MECHANISM AND CATALYST STABILITY OF METAL-ASSISTED CHEMICAL ETCHING OF SILICON

PRAYUDI LIANTO

(*S.Si., Universitas Pelita Harapan*)

A THESIS SUBMITTED

FOR THE DEGREE OF DOCTOR OF PHILOSOPHY

IN ADVANCED MATERIALS FOR MICRO- AND NANO-SYSTEMS (AMM&NS)

SINGAPORE-MIT ALLIANCE

NATIONAL UNIVERSITY OF SINGAPORE

2013

DECLARATION

I hereby declare that this thesis is my original work and it has been written by me in its entirety. I have duly acknowledged all the sources of information which have been used in the thesis.

This thesis has also not been submitted for any degree in any university previously.

Prayudi Lianto

8 July 2013

Acknowledgements

This thesis would not have been possible without the blessings of my Lord Jesus Christ and the support of the following people.

First, I would like to express my utmost gratitude to my thesis supervisors, Professor Choi Wee Kiong and Professor Carl V. Thompson. Professor Choi has helped tremendously in shaping me to be an inquisitive and independent researcher. His patience in monitoring my research progress through our weekly meetings and in helping me formulate and "sift through" my results into a meaningful and coherent thesis, even when he had to go through medical treatments, is invaluable, to say the least. I am also greatly indebted to Professor Thompson, who has provided many important and critical suggestions to my research works. His advice and encouragement greatly aided me in my journey as a PhD student. I am also very grateful for the useful discussions I had with my thesis committee members, Professor Chim Wai Kin and Professor Caroline Ross.

I must also give credit to Walter Lim, Xiao Yun, and Ah Lian Kiat as the technologists of Microelectronics lab, where I carried out all my experiments. Walter's technical expertise in the lab equipments have made him nothing short of a "superman" of the lab. I am also thankful to the CICFAR staffs: Koo Chee Keong, Ho Chiow Mooi, and Linn Linn, for being very kind and accommodating, especially towards my "non-office-hour" SEM bookings. I also would like to thank Koh Hwee Lin (ECE-DSI Laser Microprocessing lab), Woo Ying Chee (Electrical Machines & Drives lab), Tan Chee Siong and Tan Kok Kiong (Mechatronics & Automation lab), for their help with the electrical equipments.

Furthermore, I am grateful to my SMA fellow “PhD soldiers”: Sang, Thanh, Zongbin, Agung, Ria, and Chiew Yong. All of you have made my graduate studies more alive and meaningful. I am also thankful for the companionship of the other students whom I have shared the office space with: Raja, Tze Haw, Khalid, Gabriel, Yun Jia, Zhoujia, Haitao, Zheng Han, Thi, Zhu Mei, Bihan, Cheng He, Changquan, Jiaxin, Maruf, Lin Thu, and Wang Kai.

Special thanks go to my dearest Ria for being very supportive in my four-year journey with SMA. I also thank my dear brother, Alvin, for his constant encouragement. Finally, I would like to dedicate this thesis to my parents, Jio Su Ngo and Suryadi Lianto. Mom and Dad, I would not have made this far without your continual love, support, trust, and prayers.

Table of Contents

Summary

The objective of this study was to conduct a mechanistic study of MACE. Specifically, the objectives were to investigate the role of electronic holes, study the influence of etchant chemistries and catalyst geometry on the etching stability, study the porosity of etched nanostructures using IL-patterned catalyst, and investigate the role of voltage bias in the etching mechanism.

First, we report results of a systematic study on the mechanism and catalyst stability of metal-assisted chemical etching (MACE) of Si in HF and H_2O_2 using isolated Au catalyst. The role of electronic holes on etching of Si underneath Au catalyst is presented. The role of excess holes is characterized through the observation of pit formation as a function of catalyst proximity and the ratio of the H_2O_2 and HF concentrations in the etch solution. We show that suppression of excess hole generation, and therefore pitting, can be achieved by either adding NaCl to the etch solution or by increasing the HF concentration relative to the H_2O_2 concentration. We also demonstrate that an external electric field can be used to direct most of the excess holes to the back of the Si wafer, and thus reduce pit formation at the surface of the Si between the Au catalysts. We also explore the role of an Au back contact on the etching characteristics for three different cases: (i) back contact is exposed to the etchant, (ii) back contact is not exposed to the etchant, and (iii) etching with an additional current injection from an applied bias. Next, we propose that there are two possible causes for catalyst instability during MACE, namely the overlap of excess holes between neighboring catalysts and the generation of hydrogen (H_2) bubbles. From these two modes of instability, we define a

regime of etch chemistry and catalyst spacing for which catalyst stability and vertical etching can be achieved.

Next, we investigate the etching characteristics with interconnected catalyst configurations patterned using interference lithography (IL). We propose that the role of excess holes is more significant in these catalyst configurations such that the etched nanostructures possess a relatively high degree of porosity. We demonstrate that the porosity of the nanostructures can be exploited to obtain an ordered array of Si nanocones, which may find applications in biomedical research, scanning probe nanolithography, or field-emitting-tip devices. The influence of doping type and concentration on the porosity of nanowires is examined. We further demonstrate that the porosity of the nanostructures can be tuned from the etchant concentration.

Finally, we use an electric field to develop a new etching method called bias- and metal-assisted chemical etching (BiMACE) of Si. Essential features of BiMACE are presented and comparisons are made between MACE and BiMACE. Quantitative analysis of the hole contribution to BiMACE without and with H_2O_2 is presented. The etching mechanism of BiMACE is discussed. Application of BiMACE to fabricate Si nanowires is also demonstrated and its possible extension to other semiconductor materials is suggested.

List of Tables

List of Figures

List of Symbols

2D	Two-dimensional
3D	Three-dimensional
AAO	Anodic aluminum oxide
Ag	Silver
$AgNO_3$	Silver nitrate
ARC	Anti-reflection-coating
Au	Gold
BCP	Block copolymer
BiMACE	Bias- and metal-assisted chemical etching
C(x,y,t)	Hole concentration inside Si as a function of position and time (etch duration)
C_0	Hole concentration at Au-Si interface
CHF_3	Trifluoromethane
Cl	Chlorine
Cu	Copper
$Cu(NO_3)_2$	Copper (II) nitrate
D	Hole diffusivity
DI	Deionized
DOF	Degree of freedom
E_0	Energy of primary electron
EBL	Electron-beam lithography
E_C	Conduction band edge of Si
$E_{C,0}$	Conduction band edge of Si under zero bias
E_F	Fermi level
E_G	Band gap of Si
erfc	Complementary error function
EtOH	Ethanol
E_V	Valence band edge of Si

$E_{V,0}$	Valence band edge of Si under zero bias
Fe	Iron
$Fe(NO_3)_3$	Iron (III) nitrate
G	Conductance
GaAs	Gallium arsenide
GaN	Gallium nitride
h^+	Electronic holes
H^+	Proton
H_2	Hydrogen
H_2O	Water
H_2O_2	Hydrogen peroxide
H_2SiF_6	Hexafluorosilicic acid
HCl	Hydrochloric acid
HeCd	Helium cadmium
HF	Hydrofluoric acid
I	Current
IL	Interference lithography
J_n	Electron current
J_p	Hole current
J_{PS}	Critical current density
J_{walls}	Spread current
$K_2Cr_2O_7$	Potassium dichromate
K_2PtCl_6	Potassium hexachloroplatinate (IV)
$KAuCl_4$	Potassium gold (III) chloride
$KMnO_4$	Potassium permanganate
KOH	Potassium hydroxide
L_p	Hole diffusion distance
M	Molar
MACE	Metal-assisted chemical etching

n	Donor-doped Si
Na	Sodium
$Na_2S_2O_8$	Sodium persulfate
NaCl	Sodium chloride
NH_4OH	Ammonium hydroxide
NHE	Normal hydrogen electrode
Ni	Nickel
NP	Nanoparticle
O_2	Oxygen
p	Acceptor-doped Si
p	Spatial period in IL setup
Pd	Palladium
pH	Acidity
PL	Photoluminescence
PR	Photoresist
Pt	Platinum
R	Resistance
RCA	Radio Corporation of America
RF	Radio frequency
RIE	Reactive Ion Etching
SC	Standard cleaning
SE	Secondary electron
SEM	Scanning electron microscope
SF_6	Sulfur hexafluoride
Si	Silicon
SiGe	Silicon germanium
SiO_2	Silicon dioxide
TEM	Transmission electron microscope
U	Voltage bias

UV	Ultraviolet
V	Voltage
VB	Valence band
V_H	Helmholtz potential
VLS	Vapor-liquid-solid
V_{sc}	Space-charge potential
Z	Atomic number
ϕ	Angle between primary electron and sample surface
Φ	Work function
Φ_B	Schottky barrier height
χ	Electron affinity of Si
λ	Laser wavelength in IL setup; escape depth in SEM
ρ	Molar ratio, defined as [HF]/([HF]+[H_2O_2])
θ	Half-angle in IL setup
Ω	Unit of resistance

Chapter 1. Introduction

1.1 Background

Nanostructures are assembly of materials in microscopic scale. In 1960, Feynman[1] predicted that materials which are manipulated on such a small scale could exhibit interesting properties which are absent in macroscopic scale. In particular, many potential applications have been demonstrated for silicon (Si) nanostructures, such as Si nanowire-based field effect transistors,[2,3] nanowire anodes for batteries,[4,5] thermoelectric devices,[6] biomedical sensors,[7,8] photovoltaic cells,[9,10,11] and templates for magnetic data storage.[12] These Si nanostructures are fabricated using either bottom-up (growth) or top-down (etching) approaches.

The most well-known growth method is the vapor-liquid-solid (VLS) mechanism,[13] in which chemical vapor deposition is used with a metal catalyst particle (e.g. Au) under conditions for which growth occurs only at the particle-silicon interface. However, the use of the VLS process for applications has a number of drawbacks. First, the VLS technique only allows formation of cylindrical wires. In many applications, one-dimensional nanostructures with other cross-sectional shapes would be useful. For example, fin shapes are of great interest for use in metal-oxide-semiconductor field effect transistors in which the channel current can be more readily controlled than in planar or cylindrical structures.[14,15] Second, there are concerns with the use of catalysts such as Au at the temperatures required for VLS processes, because the catalyst metal is likely to be incorporated into the wires. Third, crystallographic orientation of the grown nanowire depends on

its diameter.[16] Also, it has been found that no wires can be grown on highly doped Si wafers.[17]

Among various etching methods, the metal-assisted chemical etching (MACE)[18] has recently emerged as a promising method to fabricate Si nanostructures for several reasons. First, cross-sectional shapes of the etched nanowires can be readily varied.[19] Second, it is a low-temperature process and thus, Au incorporation into Si can be eliminated. Third, crystallographic orientation of the nanowires can be controlled.[20] Fourth, MACE is known to work on Si wafers independent of doping type and level.[21] Finally, it is able to produce very high-aspect-ratio structures,[22] which are hardly achievable by any other fabrication methods.

However, due to difficulties in direct in-situ observation, the exact mechanism of MACE is still under scrutiny. For example, there are different proposed chemical reactions governing MACE process as reported in the literature.[23] It is also intriguing as to why isolated catalyst tend to change its etch directions in a non-uniform manner,[24,25] in contrast to etching with interconnected catalyst.[19,20] It is therefore important to conduct a more systematic study on the mechanism of and catalyst stability in MACE in order to gain better leverage of this process to sculpture Si. The subsequent sections will describe general etching methods of Si, followed by a brief overview of MACE.

1.2 Etching of Silicon

There are two types of etching of Si, wet and dry. Wet etching involves the use of liquid chemicals to remove the Si atoms. KOH is one of the most widely employed etchant for Si due to its high degree of anisotropy, i.e. {111} planes are etched much slower than {100} and {110} planes. By exploiting this etch anisotropy, several distinct structures can be fabricated on Si. Using interference lithography to define square openings which are aligned to <110> directions, Choi *et al.*[26] demonstrated the fabrication of inverted pyramid arrays on Si <100> substrate, as shown in **Figure 1.1a**. Ahn *et al.*[27] patterned long rectangular openings with the lengths aligned to <111> directions to fabricate high-aspect-ratio Si gratings on Si <110> substrate, as shown in **Figure 1.1b**. The high-aspect-ratio gratings were prevented from collapsing by using critical point drying method. It should be clear from the above examples that alignment is critical to achieve the desired structure. Another limitation is that it is not possible, for example, to obtain vertical grating structures with the sidewalls being non-{111} planes.

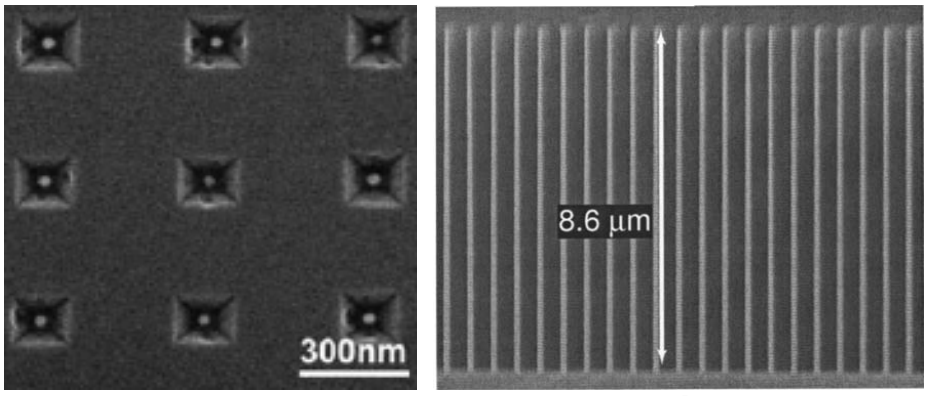

(a) (b)

Figure 1.1: (a) Inverted pyramid arrays fabricated on Si <100> substrate.[26] (b) High-aspect-ratio Si gratings fabricated on Si <110> substrate.[27]

Dry etching is also widely employed to fabricate Si nanostructures. In this process, a gas plasma is generated inside a vacuum chamber, forming reactive ions to react with the materials to be etched and form volatile byproducts. Nassiopoulos *et al.*[28] fabricated Si nanowalls and nanopillars (**Figure 1.2**) by first defining an etch mask pattern using optical lithography and subsequently transferring the pattern to the underlying Si substrate using SF_6 and CHF_3 reactive ion etching. Dry etching process, however, has several limitations. First, anisotropy can be increased – by using more energetic ions – but in the expense of reduced etch selectivity between the etched materials and the etch mask, which could limit the ultimate aspect-ratio achievable with this process. Second, the high energy ions can produce surface damage, which can be undesirable for device applications. In addition, it requires specialized equipment which can be quite costly.

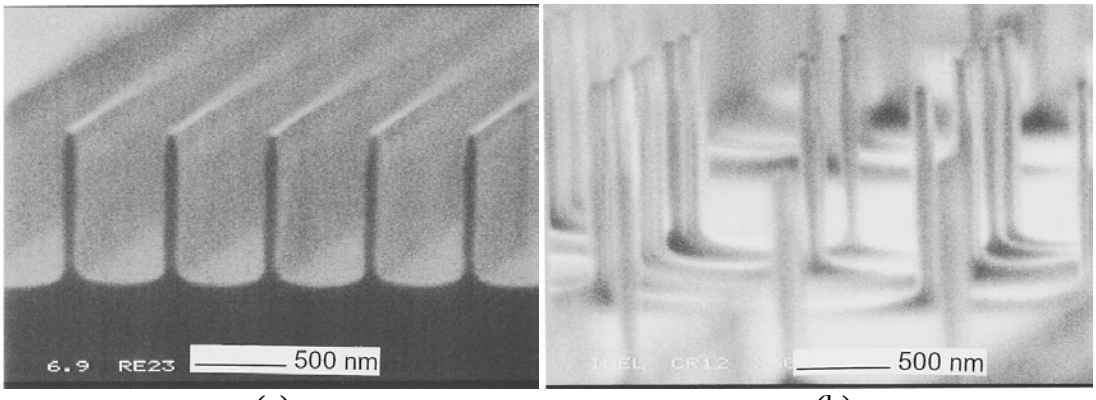

(a) (b)

Figure 1.2: Silicon nanowalls (a) and nanopillars (b) fabricated using SF_6 and CHF_3 reactive ion etching.[28]

1.3 Metal-Assisted Chemical Etching of Silicon

MACE is a wet etch process in which the etch rate of Si in a mixture of HF and an oxidizing agent is greatly increased in the presence of noble metal catalyst. First investigated by Li and Bohn[18], it was found that Au, Pt, and

Au/Pd can act as catalysts for MACE in a mixture of HF and H_2O_2. There were also reports of using Ag as the catalyst for MACE.[24,29] It should be noted that there are other possible oxidizing agents besides H_2O_2, such as $Fe(NO_3)_3$,[30] $Na_2S_2O_8$, $K_2Cr_2O_7$, and $KMnO_4$.[31]

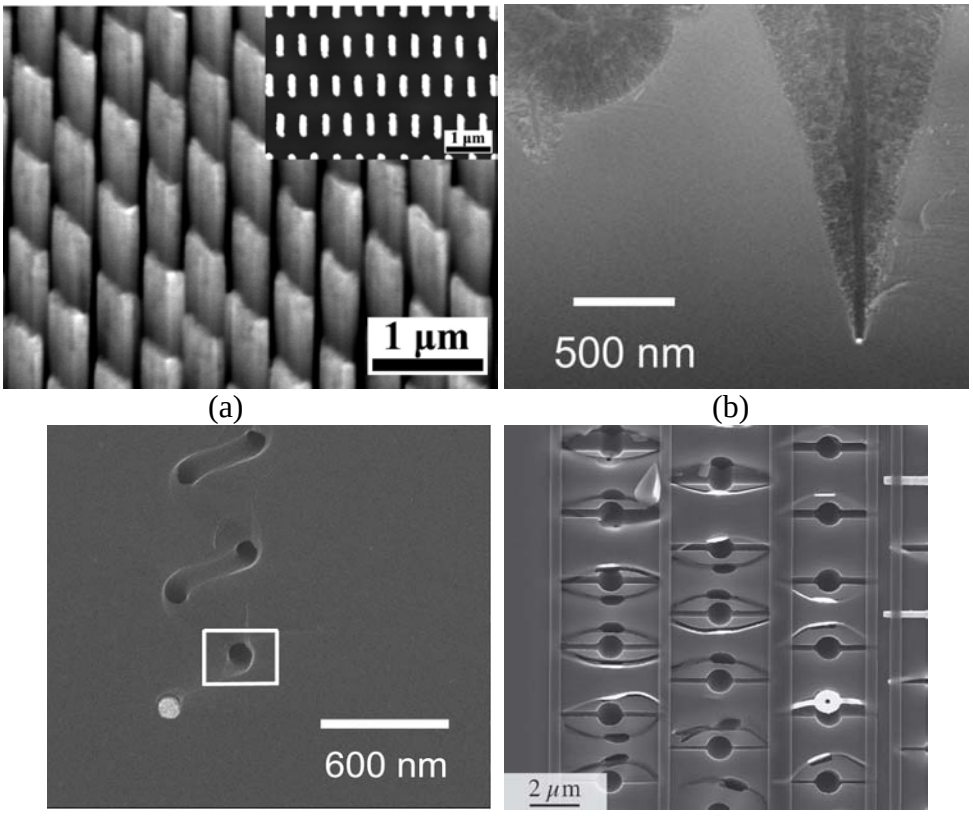

Figure 1.3: (a) Si nanofins obtained using Au perforated film etched in a mixed solution of 4.6 M HF and 0.44 M H_2O_2.[19] (b-c) Cylindrical and helical Si nanoholes obtained using Pt nanoparticles etched for 5 minutes in a mixed solution of: (b) 50% HF, 30% H_2O_2, and H_2O at a volume ratio of 2:1:8; (c) 50% HF and 30% H_2O_2 at a volume ratio of 10:1.[32] (d) Swinging catalyst etching etched in a mixed solution of 48% HF, 35% H_2O_2, and H_2O at a volume ratio of 4:1.3:2.8.[33]

The localized etching of Si in the vicinity of the noble metal allows one to fabricate various structures using MACE depending on the catalyst patterning techniques. Choi *et al.*[19] used Au perforated film patterned by interference lithography (IL) to fabricate Si nanofin arrays, as shown in

Figure 1.3a. Tsujino and Matsumura[32] demonstrated the fabrication of cylindrical and helical Si nanoholes using Pt nanoparticles, as shown in **Figures 1.3b** and **c**. Hildreth *et al.*[33] demonstrated that by pinning the catalyst with an insulating layer, the catalyst can be forced to create 3D rotational etching, as can be seen in **Figure 1.3d**.

Figure 1.3b shows that the cylindrical nanoholes were surrounded by a porous layer as opposed to the helical nanoholes, suggesting that porosity in MACE is dependent on etchant concentration. It is obvious that etchant concentration also plays a role in determining the etch morphology of isolated catalyst (e.g. nanoparticles), that is low HF concentration resulted in straight cylindrical nanoholes (**Figure 1.3b**) and high HF concentration resulted in helical nanoholes (**Figure 1.3c**). Also, catalyst configuration seems to have an influence on the etch stability because the nanofins in **Figure 1.3a** are straight despite being etched in a high relative HF concentration. Finally, it is possible to stabilize etching with isolated catalyst by using a pinning structure (**Figure 1.3d**). However, this is limited to a simple swinging pattern and the etching is restricted to only a certain depth because the pinning arms may finally detach from the catalyst, after which the control exerted by the pinning structure is lost.

1.4 Research Objectives

In view of the above review, research gaps for the current study are summarized below:

- The formation of porous layer around the cylindrical pores in **Figure 1.3b** indicates that etched structures using MACE is associated with a certain

degree of porosity. Study on porosity of etched structures using MACE has been reported, but limited to the case of nanoparticles.[29]

- Etchant concentration affects the etching characteristics of isolated catalyst.[29,32] However, these studies were limited to the case of etching with nanoparticles.
- It has been shown that isolated catalyst can be stabilized by using a pinning structure.[33] However, this is limited to certain etching patterns and the control is lost once the pinning structure delaminates from the catalyst.

The main aims of this study were to conduct a mechanistic study of MACE. The specific objectives were to:

- investigate the role of electronic holes in MACE process and develop ways to control them.
- study the influence of etchant chemistries and catalyst geometry on the etching stability of isolated patterned catalyst.
- study the porosity of etched nanostructures using IL-patterned interconnected catalyst.
- investigate the role of voltage bias in the etching mechanism.

The role of electronic holes, etchant chemistries, catalyst geometry, and voltage bias may be crucial to gain a better understanding of the mechanism of MACE. This may give the leverage to fully exploit the potential of MACE to fabricate various structures on Si.

The focus of this study was on a MACE system with Au catalyst and H_2O_2 as the oxidant. Even though catalytic etching is known to work with

different metal catalysts and oxidants, the chemical reaction obeys similar oxidation-dissolution principle.[30]

1.5 Organization of Thesis

This thesis will be divided into seven chapters. Chapter 2 will describe the theory of MACE of Si as reported in the literature. Types of catalyst and their etching mechanisms will be elaborated. Subsequently, porosity of the etched structures using MACE will be discussed from its dependence on dopant and etchant composition. Next, etching direction in MACE will be examined in two distinct catalyst configurations, namely interconnected and isolated catalyst. Finally, electrochemical etching of Si in HF will be discussed.

Chapter 3 will describe the experimental procedures employed in this study.

Chapter 4 will investigate the mechanism and catalyst stability of MACE using isolated catalyst. The role of electronic holes to the etching and pit formation is presented. The influence of catalyst spacing and [H_2O_2] on the pit formation is investigated. Control of hole injection is demonstrated by adding NaCl, increasing [HF], or applying a voltage bias. The role of Au back contact on the etching characteristics is explored. Two modes of etching instability are proposed, namely the overlap of excess holes between neighboring catalysts and the generation of hydrogen (H_2) bubbles. From these two modes of instability, we define a regime of etch chemistry and catalyst spacing for which catalyst stability and vertical etching can be achieved.

Chapter 5 will investigate the etching characteristics with interconnected

catalyst configuration patterned by IL. The role of excess holes is linked to the formation of Si nanocones from porous Si nanowires. Influence of Si doping type and concentration on the porosity is investigated. Control of excess holes is demonstrated by tuning the etchant composition.

Chapter 6 will investigate a new etching method called Bias- and Metal-Assisted Chemical Etching (BiMACE) of Si. Essential features of BiMACE are presented and comparisons are made between MACE and BiMACE. Quantitative analysis of the hole contribution to BiMACE without and with H_2O_2 is presented. The etching mechanism of BiMACE is discussed. Application of BiMACE to fabricate Si nanowires is also demonstrated and its possible extension to other semiconductor materials is suggested.

Chapter 7 will summarize the thesis and propose several recommendations for future work.

Chapter 2. Literature Review:

Metal-Assisted Chemical Etching of Silicon

2.1 Introduction

MACE has recently emerged as an attractive method to fabricate Si nanostructures, especially because it is simple, low-cost, and able to control various parameters of the etched nanostructures, such as cross-sectional shape, diameter, length, and crystallographic orientation.[23] In fact, MACE has been demonstrated not only on Si substrate but also on other semiconductors, such as silicon germanium (SiGe)[34] ,gallium arsenide (GaAs),[35,36], and gallium nitride (GaN).[37] This chapter will discuss the theory behind MACE of Si. Two distinct phases of catalyst and their etching mechanisms will be elaborated. The first form is where the catalyst is in the liquid phase (metal salt) and the etching occurs concurrently with the metal deposition on the Si surface. The second one is where the catalyst is in the solid phase and separately deposited on the Si surface prior to etching. Subsequently, porosity of the etched structures using MACE will be discussed from its dependence on dopant and etchant composition. Next, etching direction in MACE will be examined in two possible catalyst configurations, namely interconnected and isolated catalyst. Finally, electrochemical etching of Si in HF solution will also be discussed.

2.2 Types of Catalyst and Redox Reactions

In this section, mechanisms of MACE will be presented based on the phases of the catalyst, liquid and solid. Proposed redox reactions responsible for the etching of Si will be presented.

2.2.1 Liquid-Phase Catalyst

In this process, Si is immersed in a mixture of HF and metal salt. The catalyst is thus in ionic form resulting from dissociation of the metal salt. For example, let us consider the most commonly known system of $AgNO_3$/HF. Peng *et al.*[30] explained the Ag deposition process by first comparing the Si energy levels with the metal reduction potentials, as shown in **Figure 2.1a**. As can be seen, the energy level of Ag^+/Ag system is below the Si valence band (VB) edge. Therefore, it is expected that the Ag^+ ions will be reduced (cathodic reaction) to solid Ag on the Si surface by attracting the electrons from the valence band of Si. The Si atom on the surface, losing its valence band electrons, will be oxidized (anodic reaction) and dissolved in HF. The proposed reactions are,[30]

Cathode: $Ag^+ + e_{VB}^- \rightarrow Ag^0(s)$ **Equation 2.1**

Anode: $Si(s) + 2H_2O \rightarrow SiO_2 + 4H^+ + 4e_{VB}^-$ **Equation 2.2**

$SiO_2(s) + 6HF \rightarrow H_2SiF_6 + 2H_2O$ **Equation 2.3**

Figure 2.1b depicts the electroless Ag deposition mechanism of Si in $AgNO_3$/HF system. First, Ag nuclei are formed on the Si surface accompanied by the oxidation and dissolution of Si in contact with the nuclei to form pits. Since the Ag nuclei are more electronegative than Si, they attract electrons from the Si and become negatively charged. These negatively charged Ag nuclei serve as preferred sites for subsequent Ag^+ reduction events. As a result, the etching of Si will be localized beneath the Ag particles while the Ag particles continue to grow in size. It is important to notice that the etching of Si requires HF to access the metal-Si interface. Therefore, if the Ag particles continue to grow and finally cover the whole Si surface, etching will halt.

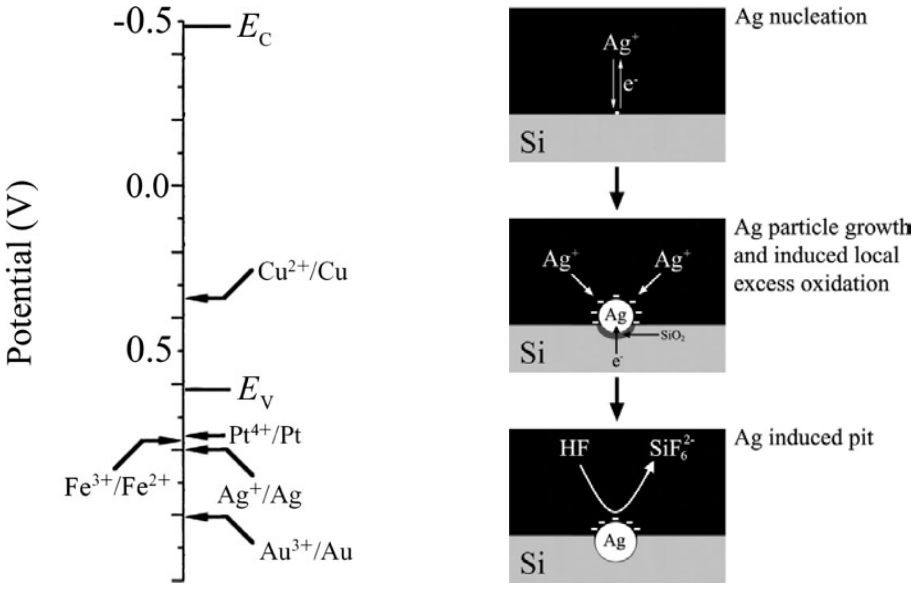

(a) (b)

Figure 2.1: (a) Qualitative diagram comparing the energy levels of Si with five metal reduction systems (E_c and E_v are the conduction and valence bands of Si). (b) Schematic of electroless Ag deposition process on a Si substrate immersed in HF/$AgNO_3$ solution.[30]

To avoid this from happening, the etching process is resumed using another oxidant instead of $AgNO_3$, such as $Fe(NO_3)_3$. From **Figure 2.1a**, Fe^{3+} will be reduced to Fe^{2+} because the reduction potential is lower than the Si valence band edge. The reduction of Fe^{3+} occurs preferentially on the Ag particles and at the same time, the Si underneath the particles continues to oxidize and dissolve in HF, as shown in **Figure 2.2a**. The proposed reactions are,[30]

Cathode: $Fe^{3+} + e_{VB}^- \rightarrow Fe^{2+}(s)$ **Equation 2.4**

Anode: $Si(s) + 2H_2O \rightarrow SiO_2 + 4H^+ + 4e_{VB}^-$ **Equation 2.5**

$SiO_2(s) + 6HF \rightarrow H_2SiF_6 + 2H_2O$ **Equation 2.6**

Upon prolonged immersion in the etchant, nanowire array will form, as shown in **Figure 2.2b**. It was suggested that the absence of lateral etching in this process is due to the formation of a charge-depletion layer around the metal

particles. The catalytic redox reaction therefore would occur at the metal/Si interface because it has the shortest charge-transport distance.

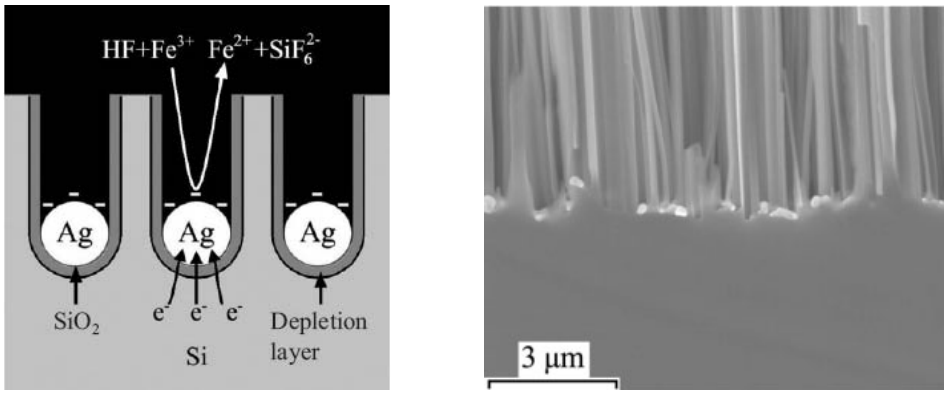

(a) (b)

Figure 2.2: (a) Mechanism of nanowire formation using electrolessly deposited Ag particles in HF/$Fe(NO_3)_3$ system. (b) Si nanowire arrays prepared in 5.0 M HF containing 0.02 M $Fe(NO_3)_3$.[30]

Figure 2.1a also shows that there are other metals that can be electrolessly deposited on the Si surface. Peng *et al.*[30] demonstrated that by mixing HF with $KAuCl_4$, K_2PtCl_6, or $Cu(NO_3)_2$, the Si surface became loaded with Au, Pt, or Cu particles. These metal particles also catalyzed the etching of Si in HF/$Fe(NO_3)_3$ system with the etch morphology depending on the metal coating morphology. Au formed dense particles and resulted in nanowire array, similar to the case of Ag. Pt formed sparse particles and resulted in a combination of straight and winding pores on Si. The non-uniform etching direction of these Pt particles suggests that proximity of catalyst may have an influence on the etching direction. Finally, Cu only formed shallow pits after immersion in HF/$Fe(NO_3)_3$ system because the reduction potential of Fe^{3+}/Fe^{2+} is more positive than that of Cu^{2+}/Cu so that the Cu particles will be converted back to its ionic state and dissolved in the solution. It is obvious that even though the catalyst preparation using electroless deposition is simple, the

etched morphology is limited to simple pore and nanowire structures and only associated with certain types of metal catalyst. Diameter of the resulting Si nanowires could only be roughly tuned by varying the concentration of $AgNO_3$ and HF.[38]

2.2.2 Solid-Phase Catalyst

There are many ways to deposit solid catalyst on Si surface. First demonstration of MACE by Li and Bohn[18] utilized a thin discontinuous sputtered layer of metal (3-8 nm) as the catalyst. Three different metals were investigated, namely Au, Pt, and Au/Pd. The metal-loaded Si surface was then etched in 49% HF and 30% H_2O_2 (balanced with EtOH with equal proportions) to create porous Si structures, as shown in **Figure 2.3**. It was found that Pt and Pd yielded much higher etch rate than Au, suggesting stronger catalytic role of Pt and Pd.

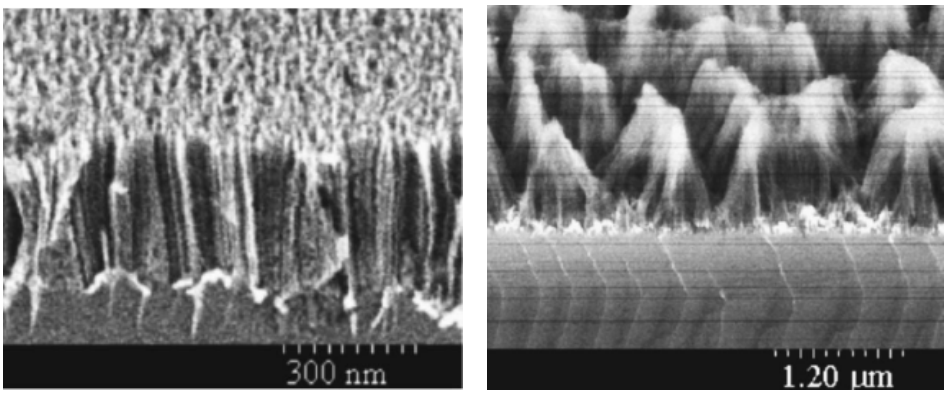

(a) (b)

Figure 2.3: (a) Au-coated Si(100) after etching in HF/H_2O_2 for 30 seconds. (b) Pt-coated Si (100) after etching in HF/H_2O_2 for 30 seconds.[18]

The proposed reactions are,[18]

Cathode: $H_2O_2 + 2H^+ \rightarrow 2H_2O + 2h^+$ **Equation 2.7**

$2H^+ \rightarrow H_2\uparrow + 2h^+$ **Equation 2.8**

Anode: $Si + 4h^+ + 4HF \rightarrow SiF_4 + 4H^+$ **Equation 2.9**

$SiF_4 + 2HF \rightarrow H_2SiF_6$ **Equation 2.10**

Balanced: $Si + H_2O_2 + 6HF \rightarrow 2H_2O + H_2SiF_6 + H_2$ **Equation 2.11**

Since the electronic holes (h^+) are generated from the reduction of H_2O_2 and H^+, MACE can work irrespective of doping type and level of the Si substrate.

It has been mentioned earlier that the etching of Si can only proceed if HF can access the metal-Si interface, which explains why Li and Bohn used a discontinuous film in their experiments. However, solid-phase catalyst has a clear advantage over the liquid-phase catalyst in that the catalyst can now be patterned with various lithographic approaches, as will be discussed in the later sections, to etch various nano- or microstructures on Si and not limited to simple pores and nanowires.

2.2.3 Chartier/Bastide/Lévy-Clément Model

Chartier *et al.*[29] proposed the following anodic and cathodic reactions of MACE,

Cathode: $H_2O_2 + 2H^+ \rightarrow 2H_2O + 2h^+$ **Equation 2.12**

Anode: $Si + 6HF + nh^+ \rightarrow H_2SiF_6 + nH^+ + \left(\frac{4-n}{2}\right)H_2$ **Equation 2.13**

Balanced: $Si + 6HF + \frac{n}{2}H_2O_2 \rightarrow H_2SiF_6 + nH_2O + \left(\frac{4-n}{2}\right)H_2$ **Equation 2.14**

It can be seen that the balanced reaction is a generalized form of that proposed by Li and Bohn (**Equation 2.11**) by putting n = 2. However, Chartier *et al.* attributed the H_2 bubble generation to anodic instead of cathodic reaction (**Equation 2.8**) because the standard redox potential of H_2O_2/H_2O (1.76 V/NHE) is more positive than that of H^+/H_2 (0 V/NHE), where NHE[39] is

normal hydrogen electrode. In other words, H_2O_2 should be the principal reactant for the generation of h^+ at the cathodic sites. Since h^+ is necessary to change a Si atom to its oxidized state in MACE process, the absence of H_2O_2 should result in minimal etching. Indeed, they did not observe any etching for Ag nanoparticles immersed in HF solution free of H_2O_2.

2.3 Porosity

In this section, porosity of the etched structures using MACE will be discussed from its dependence on dopant (type and concentration) as well as on etchant composition.

2.3.1 Dopant Dependence

In their pioneering work on MACE, Li and Bohn[18] deduced the porosity of the etched structures from both scanning electron microscope (SEM) and photoluminescence (PL) analyses. From SEM characterization, they found that the Pt-coated areas always form larger pores with columnar structure regardless of doping types and concentrations (p^+, p^-, and n^+), while the off-metal areas have smaller pores (3-5 nm) and randomly oriented structures. From the PL spectra as shown in **Figure 2.4**, it can be seen that Pt-coated areas exhibit higher PL signal as compared to the uncoated area, with the exception for p^- sample which was attributed to the formation of isolated peaked structures after etching.[18] The higher PL signal on the coated area is understandable because larger pores or thinner Si skeletons will give rise to more prominent quantum confinement effect, as described by Canham.[40] The PL signal obtained from the uncoated area, however, is intriguing because in a

control experiment, Li and Bohn[18] did not observe any detectable etching when there is no metal coating on the Si. This strongly suggests that the electronic holes can travel across macroscopic distances to form porous structures away from the metal. Chattopadhyay *et al.*[41] suggested that carrier drift could be responsible for this observation. It is therefore very interesting to see the effect of electric field in controlling the hole travel path and thus, tuning the porosity on the no-catalyst area, as we will demonstrate in Chapters 4 to 6.

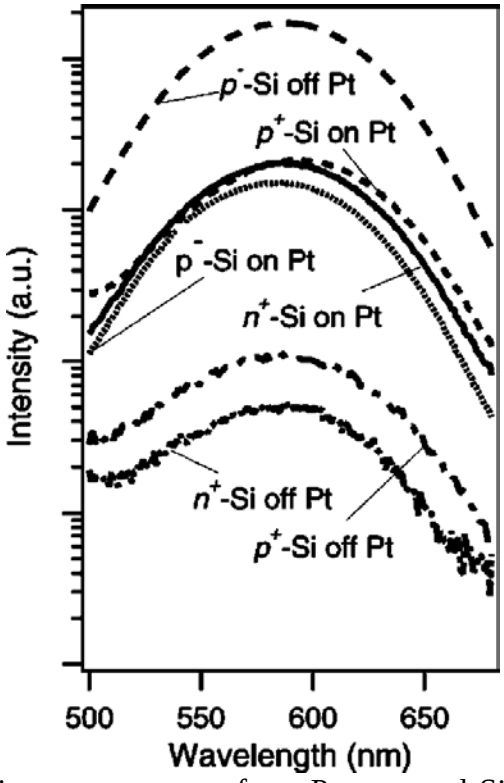

Figure 2.4: Photoluminescence spectra from Pt-patterned Si after 30-second etching in HF and H_2O_2.[18]

Hochbaum *et al.*[42] conducted systematic TEM studies on the surface morphology of the etched nanowires using 0.01-0.04 M $AgNO_3$ and 5 M HF for p-type Si wafers of different doping concentrations (corresponding to resistivity of 10, 0.01, and <0.005 Ω.cm), as shown in **Figure 2.5**. They found

that the surface roughness of the nanowires increases with decreasing resistivity (or increasing doping concentration) and mesoporous[43] nanowires (average diameter ~ 9.7 nm) were formed for p-type Si with a resistivity less than 5 mΩ.cm. They proposed two possible reasons for the observation. First, higher doping concentration in the lower resistivity wafers provides more crystal defects which may create a larger thermodynamic driving force for pore formation. Second, lower resistivity wafers (i.e. more positive Fermi level) have smaller energy barrier for charge injection across Ag-Si interface because the redox potential of Ag^+/Ag^0 is more positive than the valence band of Si. As a result, the current flow increases and thus, increasing the surface roughness or porosity.

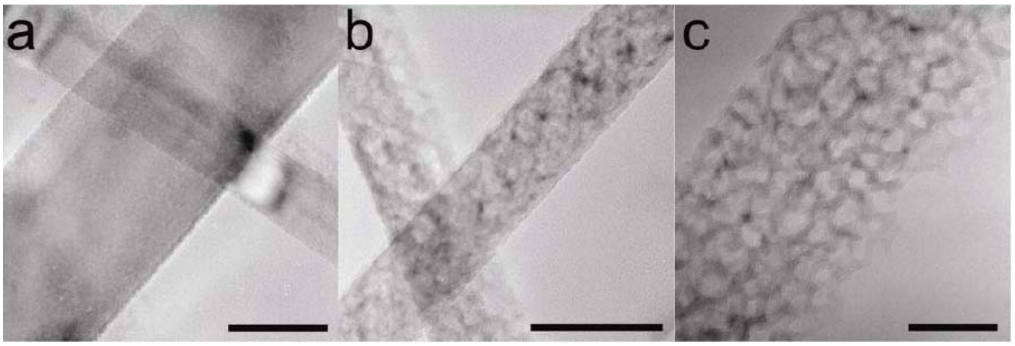

Figure 2.5: (a)-(c) TEM micrographs of Si nanowires etched from 10, 0.01 and <0.005 Ω.cm p-Si wafers, respectively. Scale bars are 100 nm for (a) and (b), and 50 nm for (c).[42]

2.3.2 Etchant Composition Dependence

The influence of etchant composition on the porosity of etched Si structures has been studied.[29,32] Chartier *et al.*[29] used molar ratio ρ, which is defined as [HF] / ([HF] + [H_2O_2]), to characterize various etched Si surface morphologies. The surface morphologies for different values of ρ are shown in **Figures 2.6a** to **g**. By allowing *n* to vary in their proposed etching reaction

(**Equation 2.14**), Chartier *et al.* proposed the concept of critical current density (J_{PS}), as shown in **Figure 2.6h**, to explain three distinct etch morphologies for different range of ρ.

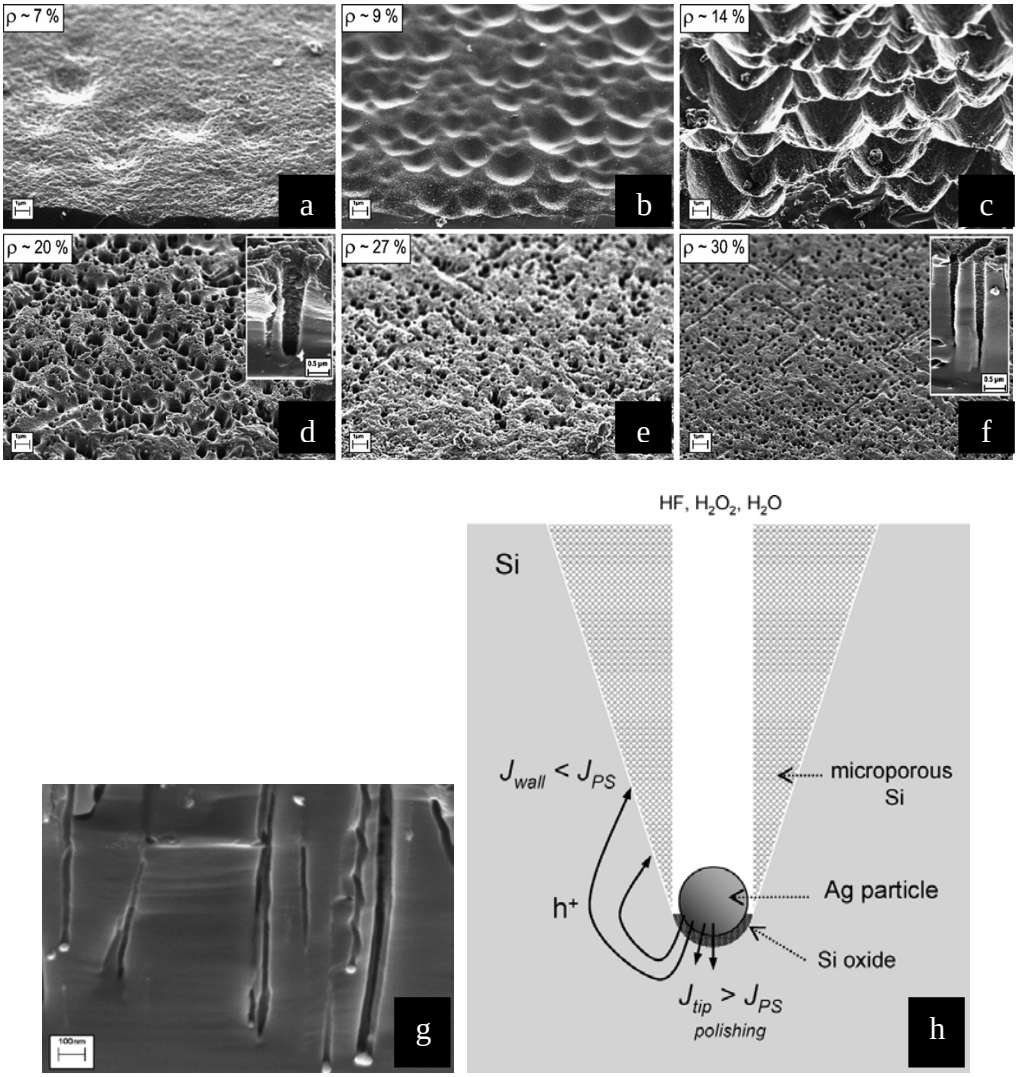

Figure 2.6: (a)-(g) SEM images of p-Si (100) samples after HF-H_2O_2 etching for ρ values of 7, 9, 14, 20, 27, 30, and 88%, respectively. (h) Diagram illustrating the mechanism of the formation of cone-shaped pores in HF-H_2O_2 solutions with 70% > ρ > 20%.[29]

1. Pore formation (100% > ρ > 20%).

At this range of ρ, apart from the holes consumed for etching directly beneath the Ag nanoparticle, some holes diffuse to the pore walls as spread current (J_{walls}) which is lower than J_{PS}. Hence, polishing (complete removal of Si) occurs beneath the particle and microporous Si forms on the walls, which

is also etched in HF-H_2O_2. The extent of this microporous region increases with decreasing ρ because more holes are available for the dissolution of Si, i.e. *n* in **Equation 2.13** increases. Therefore, for 100% > ρ > 70%, pores with diameter matching the size of the particles are formed, as shown in **Figure 2.6g**. For 70% > ρ > 20%, diameter of the pores is enlarged leading to the formation of cone-shaped pores, as shown in the insets of **Figures 2.6d** and **f**.

2. Craters (20% > ρ > 9%).

At this range of ρ, significant spread current results in a mixed process of polishing and porous Si formation, which leads to the formation of craters, as shown in **Figure 2.6b** and **c**. This morphology, however, was difficult to reproduce experimentally.[29]

3. Polishing (9% > ρ > 0).

At this range of ρ, the etching current is everywhere larger than J_{PS}. The dissolution becomes independent of the metal nanoparticle location and result in a polished Si surface, as shown in **Figure 2.6a**.

2.4 Etching Direction

In this section, etching direction of MACE will be discussed by comparing two different configurations, namely interconnected catalyst and isolated catalyst.

2.4.1 Interconnected Catalyst

Interconnected catalyst or perforated film configuration can be obtained using various patterning techniques, such as interference lithography (IL),[19,20,44] block copolymer (BCP) lithography,[20,45] nanosphere lithography,[46]

and anodic aluminum oxide (AAO).[47] With this catalyst configuration, fabrication of Si nanowire array has been demonstrated. By varying the exposure angles or the orientation between exposures in the IL setup, it is even possible to obtain nanowires with oval cross sections or nanofins.[19] In all these reports, the etching direction of the catalyst is always uniform with respect to the Si substrate. While the nanowires formed on Si (100) substrates are always vertical, there has been an inconsistency regarding the orientation of the nanowires on non-(100) Si substrates. For example, Peng *et al.*[46] observed that slanted nanowires are formed on Si (110) substrate, while Huang *et al.*[47] obtained vertical nanowires on Si substrate of the same orientation.

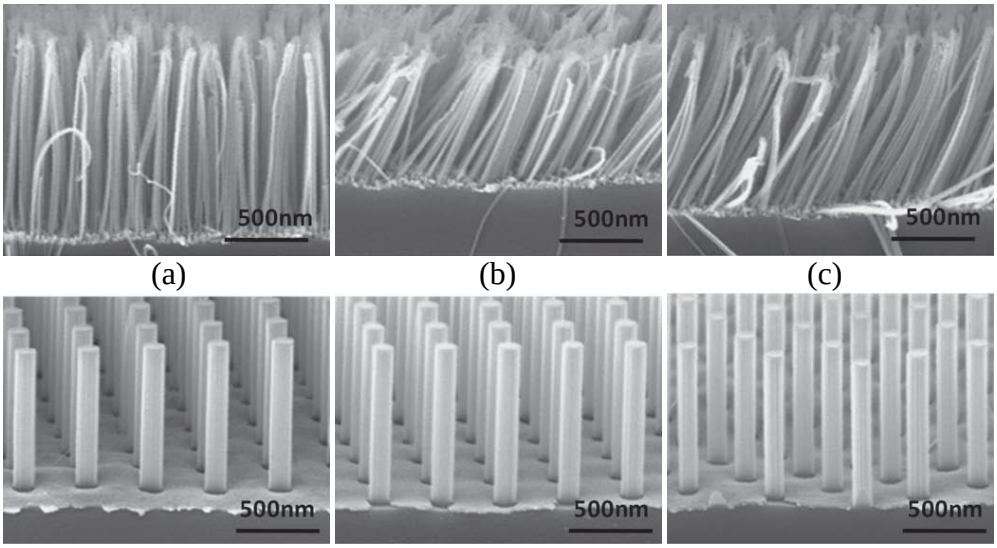

Figure 2.7: (a)-(c) Nanowire arrays etched using a Au mesh with small hole spacings patterned using BCP lithography on n(100), n(110), and n(111) Si substrates, respectively. (d)-(f) Nanowire arrays etched using a Au mesh with large hole spacings patterned using IL on n(100), n(110), and n(111) Si substrates, respectively.[20]

Chang *et al.*[20] have resolved this discrepancy by showing that the etching direction of a perforated film structure depends on the hole spacing. If the hole spacing is small, etching proceeds along the preferred <100> direction, as

shown in **Figures 2.7a** to **c**. If the hole spacing is large, however, the etching direction is vertical independent of the crystallographic orientation of the Si substrate, as shown in **Figures 2.7d** to **f**. It was suggested that when the hole spacing is small or comparable to the metal film thickness (13 nm vs. 12 nm for this study), lateral movement of the catalyst is not restricted so as to result in the inclined nanowire array. On the other hand, when the hole spacing is large, lateral movement is severely restricted so that the nanowire array is always vertical.

The preferential etching of Si along <100> directions in HF solution has been understood to be a result of different surface bond orientations, as proposed by Smith and Collins.[48] **Figure 2.8** shows the surface bond orientation for (100), (110), and (111) planes in HF solution. Since the formation of divalent Si surface state is necessary for etching, only the (100) plane presents the most favorable geometry because two bonds are symmetrically directed into the solution.

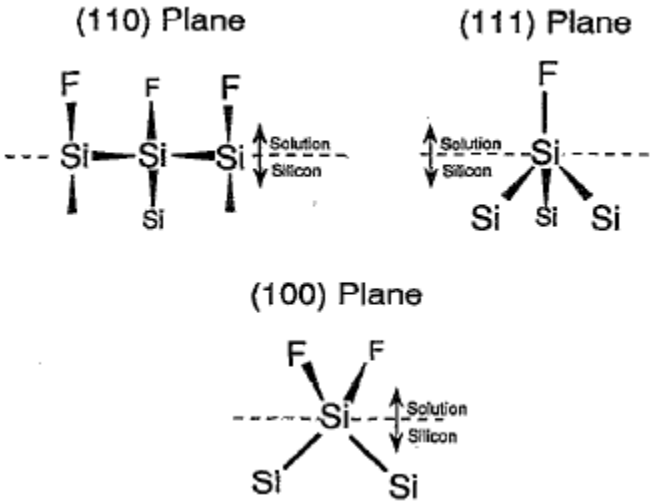

Figure 2.8: Surface bond orientation for three crystal planes: (100), (110), and (111) in HF solution.[48]

2.4.2 Isolated Catalyst

The first type of isolated catalyst commonly used in MACE is nanoparticles (NPs).[24,49,50] Tsujino and Matsumura[24] discovered that the etching direction of Ag NPs depends on the concentration of H_2O_2. For high H_2O_2 concentration ($\geq$ 0.18 M), the NPs etch along the <100> directions, as shown in **Figure 2.9a**. The preferential etching along the <100> directions has been discussed in the previous section. For low H_2O_2 concentration ($\leq$ 0.0018 M), the NPs etch along random directions, as shown in **Figure 2.9b**. For the case of high H_2O_2 concentrations, the switch of etching direction to other <100> equivalents was attributed to the shape of the NPs. They found that the Ag NPs making deep straight holes were more spherical than those making the horizontal holes. As for the formation of winding pores for low H_2O_2 concentrations, it was suggested that the spatial fluctuation in the concentration of HF or the oxidant in the pores may play a role.

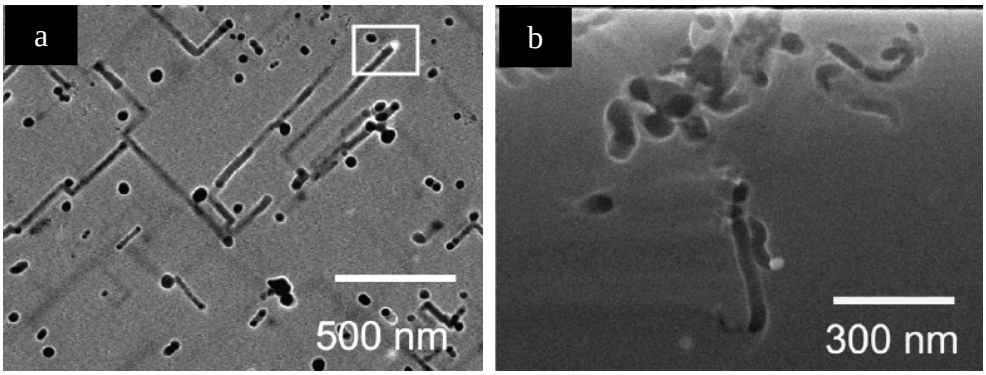

Figure 2.9: (a) Top-view SEM image of Ag NPs etched in 5.3 M HF and 0.18 M H_2O_2 for 1 minute. (b) Cross-sectional SEM image of Ag NPs etched in 5.3 M HF and 0.0018 M H_2O_2 for 30 minutes.[24]

In a separate study, Tsujino and Matsumura[32] also demonstrated that the etching direction depends on HF concentration. At low HF concentration, Pt NPs etch cylindrical holes along the <100> direction (**Figure 2.10a**) while at

high HF concentration, the NPs etch helical holes in various directions (**Figure 2.10b**). Again, the formation of helical holes was attributed to a shape effect, i.e. some irregularities on the NPs induce a local etch rate variation. Indeed, Lee *et al.*[22] demonstrated that non-spherical Au particles etched pores with spiral sidewalls while the spherical ones etched straight pores.

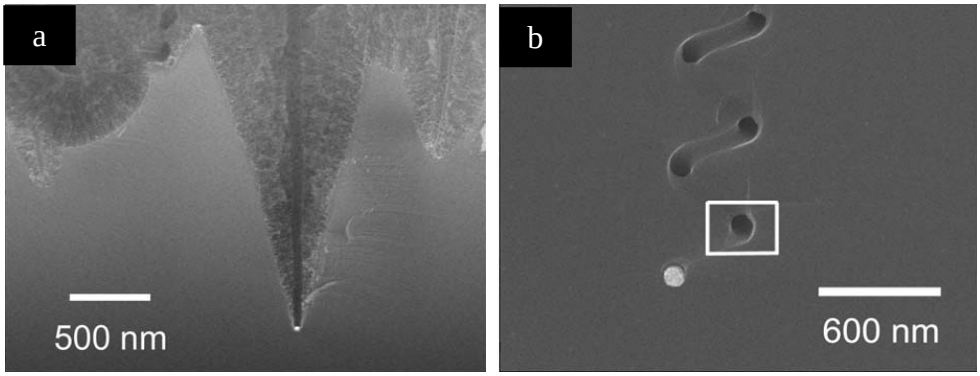

Figure 2.10: (a) Cross-sectional SEM image of Pt NPs etched in 50% HF, 30% H_2O_2, and H_2O (2:1:8 volume ratio) for 5 minutes. (b) Cross-sectional SEM image of Pt NPs etched in 50% HF and 30% H_2O_2 (10:1 volume ratio) for 5 minutes.[32]

Huang *et al.*[51] discovered that the etching direction of Ag NPs on non-(100) Si substrates is controlled by the oxidation rate. At high [H_2O_2] of 0.1 M, etching occurred along the substrate normal, as shown in **Figure 2.11a**. When the [H_2O_2] is lowered to 0.02 M, etching began to occur at an angle of ~ 23° relative to the substrate normal (**Figure 2.11b**). When the [H_2O_2] is further lowered to 0.002 M, etching occurred at a larger tilt angle of ~ 50°, i.e. along the [100] direction, as shown in **Figure 2.11c**. It was proposed that there are two competing processes for the etching of Si in MACE. First process involves direct dissolution of Si in its divalent state, which is satisfied when the etching is limited by the transfer of electrons, i.e. low [H_2O_2]. In this case, etching preferentially occurs on the most favorable surface bond orientation,

which is the {100} planes. As a result, etching occurs along the [100] direction. The second process involves the formation of intermediate oxide phase and its subsequent dissolution in HF. This condition is met when $[H_2O_2]$ is high. Since oxide dissolution in HF is isotropic, the etching direction follows the surface normal of the Si substrate. Huang *et al*. exploited this concentration-dependent etching direction to fabricate zigzag pores by periodically changing the etching concentration, as shown in **Figure 2.11d**.

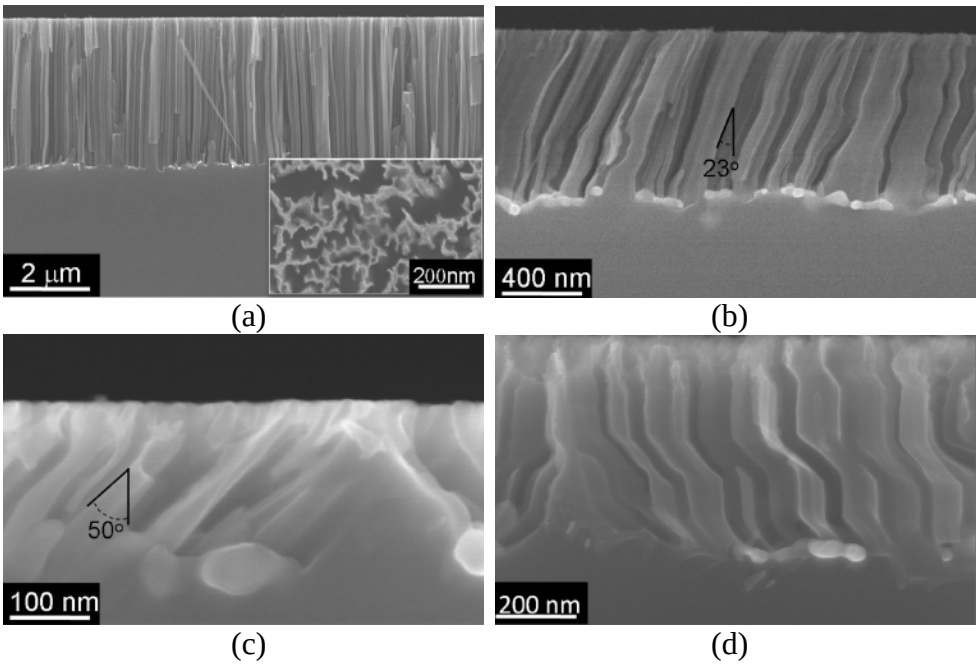

Figure 2.11: (a)-(c) Cross-sectional SEM images of p-Si (111) loaded with Ag NPs and etched in $[H_2O_2]$ = 0.1, 0.02, and 0.002 M, respectively. (d) Cross-sectional SEM image of p-Si (111) loaded with Ag NPs and etched for three periods of the sequence: 1 minute in $[H_2O_2]$ = 0.1 M and 10 minutes in $[H_2O_2]$ = 0.002 M. [HF] = 4.6 M for all samples.[51]

The second type of isolated catalyst is nanopatterns[25,33,52] made by e-beam lithography (EBL). Hildreth *et al.*[25] investigated the effect of catalyst shape and etchant composition on the etching direction of catalyst nanopatterns. First, they found that the complexity of the catalyst shape determines the possible etching path taken by the catalyst. For example, Au

nanolines have translational and rotational degree of freedoms (DOF) such that cycloid-like etching path can be seen, as shown in **Figures 2.12c** and **e**. By capping the lines on both ends to form dog-bone shape, the cycloid-like etching is eliminated allowing the catalyst to etch only along its translational DOFs (slide-etching), as shown in **Figures 2.12d** and **f**. Second, linewidth-to-thickness ratio of the catalyst was also found to affect the etching stability. For linewidth-to-thickness ratio smaller than unity, etching is generally vertical or near vertical, as shown in the last two columns of **Figures 2.12c** and **d**. On the other hand, for linewidth-to-thickness ratio larger than unity, the etching direction is more unstable, as can be seen in the first two columns of **Figures 2.12c** and **d**. Third, etchant composition or ρ (as defined in **Section 2.3.2**) was found to determine the degree of etch instability. Higher ρ generally gives rise to more erratic etchings, as can be seen by comparing **Figure 2.12e** to **Figure 2.12c**. It was suggested that as ρ increases, both etching rate of Si and electric field strength across the catalyst also increase, where the latter is responsible for the self-electrophoresis movement of catalyst in MACE process.

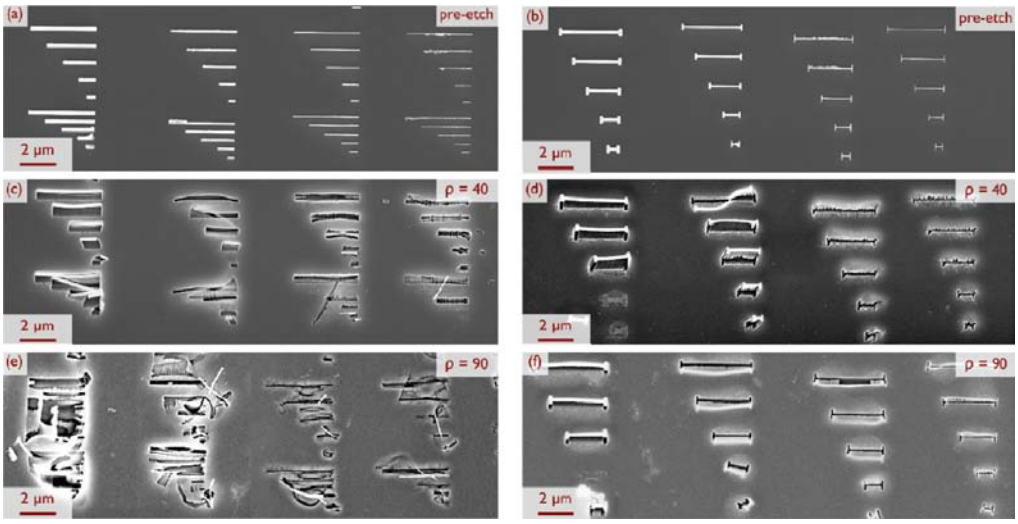

Figure 2.12: SEM images of Si etched with EBL-patterned Au nanolines (left column) and Au dog-bone shapes (right column) for 40 minutes. Line widths are 200, 100, 50, and 25 nm from left to right. Au thickness is 60 nm.[25]

Recently, Hildreth *et al.*[33] have demonstrated that by pinning the catalyst with an insulating material, the catalyst can be forced to etch complex 3D structures. **Figure 2.13a** shows the erratic etching of isolated catalysts when they are not subject to any pinning structure. **Figure 2.13b** shows that when circular catalyst pads are pinned on its arms, the pads can etch back and forth around the pivot point to create scooped-out channels in Si. It was proposed that the catalyst motion is driven by fast-electrophoresis process, in which H^+ ion flux from the anode (metal-Si interface) to the cathode (metal-liquid interface) sets up an electric field to propel the catalyst into Si. This self-electrophoretic model was introduced by Paxton *et al.*[53] to explain the spontaneous motion of Pt-Au nanorods in H_2O_2, and has also been adopted by Peng *et al.*[54] to explain the movement of Ag catalyst into Si during MACE. Hildreth *et al.*[33] calculated that the force experienced by the catalyst in their structures is in the range of 0.5 – 3.5 μN. As a result, the catalyst geometry (arm width and arm length) was found to significantly affect the etching behavior. If the arm is too short, the force experienced by the catalyst is not sufficient to move the catalyst, i.e. no etching occurs. On the other hand, if the arm is too long, the catalyst can delaminate from the pinning structure.

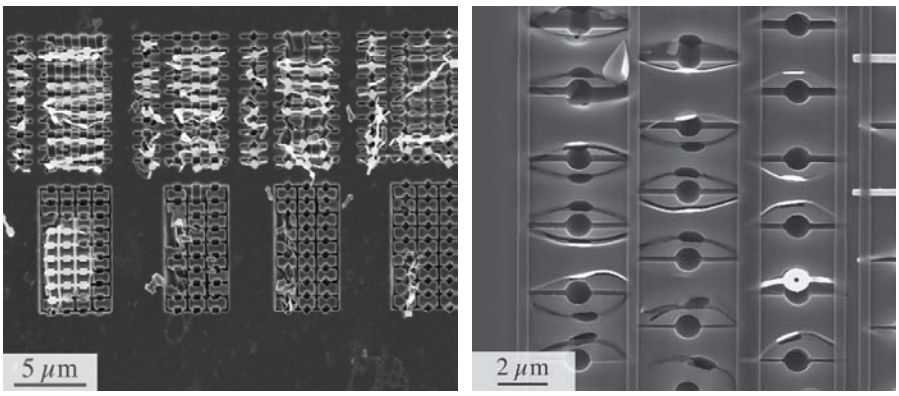

(a) (b)

Figure 2.13: (a) SEM images of erratic etching for non-pinned catalysts. (b) SEM images of "swinging" catalyst etching.[33]

It can be seen that as opposed to the case of interconnected catalyst, isolated catalyst usually does not etch in a uniform direction. The catalyst can either etch in a random manner or along the multiple <100> directions. Even though pinning the catalyst allows one to fabricate 3D nanostructures on Si, this is limited to simple swinging patterns and the etching is restricted to only a certain depth because the pinning arms may finally detach from the catalyst, after which the control exerted by the pinning structure is lost. However, this provides a valuable insight in that if we can control the movement of the isolated catalyst by other means which do not severely restrict the catalyst, 3D sculpturing of Si should be there for the taking.

2.5 Electrochemical Etching of Silicon

Another class of etching of Si in HF is the electrochemical etching method. This method had actually been invented by Uhlir[55] many years ago in 1956, but it only regained interest when Canham demonstrated its capability to produce light-emitting porous Si.[40,56] Unlike MACE where the electronic holes required for the etching of Si are provided from the reduction of H_2O_2, electrochemical etching uses holes in the Si itself, which are driven to flow to the Si-electrolyte interface by the application of a voltage bias. For this reason, electrochemical etching of n-type Si requires UV illumination to generate electron-hole pairs.[48]

The underlying mechanism of the electrochemical etching process can be understood by first examining the potential distribution of the etching system as shown in **Figure 2.14a**. It is typically assumed that the applied potential is dropped mostly on the space-charge (V_{sc}) and Helmholtz region (V_H). The

possible dominance of space-charge control gives rise to the rectifying-like I-V characteristics, as shown in **Figure 2.14b** (only the anodic dissolution portion is shown here). At small overpotential (region A), etching of Si is initiated on randomly distributed crystalline defect sites to form porous morphology. At high overpotential (region C), etching of Si occurs uniformly across the surface, i.e. electropolishing regime. At intermediate overpotential (region B), transitional morphology is formed due to a competition of pore formation and electropolishing.

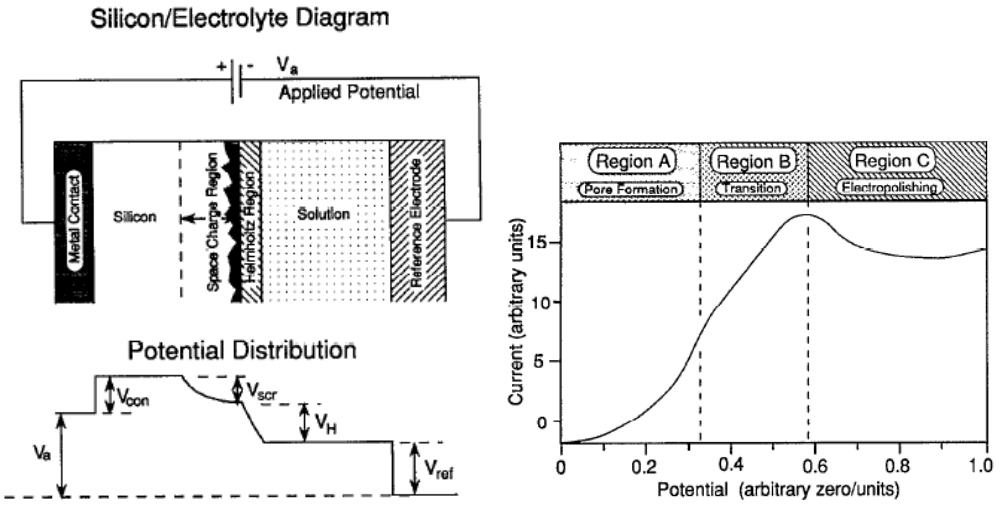

(a) (b)

Figure 2.14: (a) Schematic diagram for electrochemical etching of Si, showing potential distribution at the various interfaces. V_a is the applied voltage, V_{ref} is the solution potential, V_H is the Helmholtz potential, and V_{scr} is the space-charge potential. (b) Typical I-V relationship for Si in HF showing different regimes of dissolution.[48]

Barillaro et al.[57] demonstrated that by pre-patterning defect sites on the Si prior to etching, various arrays of regular Si microstructures can be fabricated. **Figure 2.15a** outlines the process to obtain patterned Si microstructures using electrochemical etching. First, a thermal oxide was grown on the sample and then, a standard photolithographic procedure was

carried out to define the pattern on the oxide. The pattern was then transferred to the Si by KOH etching to expose the pyramidal pits on Si. These pyramidal pits served as the preferred nucleation sites for pore formation in the subsequent electrochemical etching step. **Figure 2.15b** shows a Si microwall array fabricated by electrochemical etching using pre-patterned line defects. By controlling the pattern, it is possible to fabricate more complex microstructures, such as the meander-shaped wall array shown in **Figure 2.15c**. In the same figure, however, it can be seen that random macropores are formed on the non-patterned Si area, which was suggested to be a size-effect, i.e. more holes can diffuse to the non-patterned Si and initiate pore formation as the separation between pattern increases. This highlights the limitation of this method, i.e. a maximum dimension exists above which it is not possible to obtain pore-free Si microstructures.

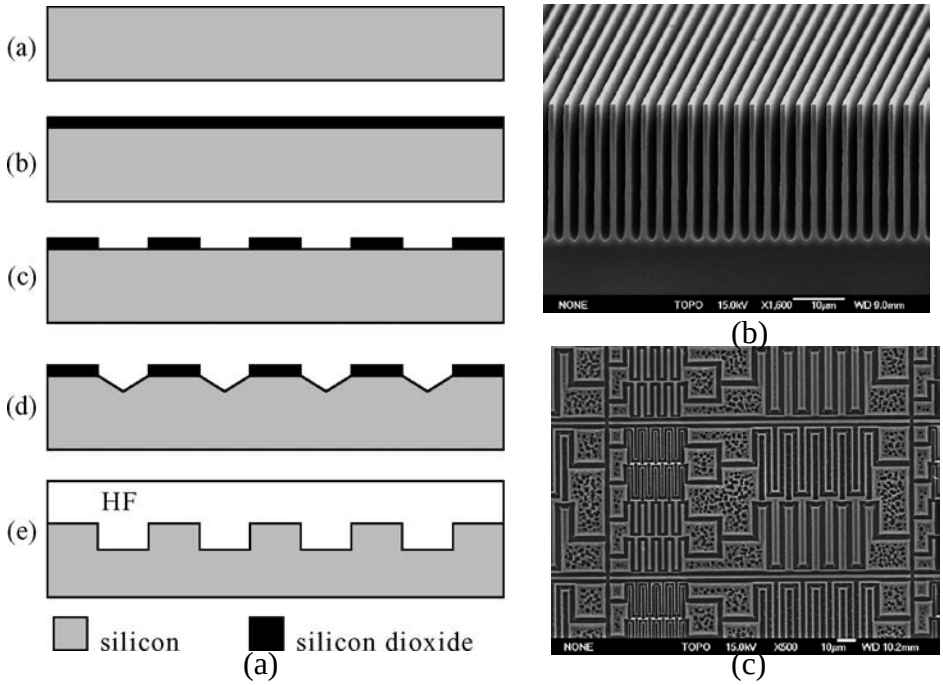

Figure 2.15: (a) Schematic diagram illustrating the fabrication of Si microstructures using electrochemical etching in HF. (b) Cross-sectional view of an electrochemically etched wall array. (c) Top view of an electrochemically etched meander-shaped wall array.[57]

Chapter 3. Experimental Methods

3.1 Introduction

This chapter will detail the experimental methods used in this study. **Section 3.2** will outline the sample preparation procedures. **Section 3.3** will discuss the patterning methods. **Sections 3.4** and **3.5** will describe the Au deposition and lift-off processes to obtain the Au patterns. **Section 3.6** will outline the setup for the MACE experiment. Finally, **Section 3.7** will discuss scanning electron microscopy (SEM) as the main characterization technique used in this study.

3.2 Sample Preparation

The Si wafer cleaning procedure consists of two RCA standard cleaning (SC) steps:[58,59]

1. SC-1.

   SC-1 serves to remove organic contaminants from the Si wafer surface. First, 250 ml deionized water (DI water) is heated to 80-90°C. Then, 50 ml hydrogen peroxide (H_2O_2, 31 wt.%) and 50 ml ammonium hydroxide (NH_4OH, 29 wt.%) are added to the solution. The Si wafers are then immersed in the solution for 10-15 minutes. Afterwards, they are rinsed in flowing DI water with bubbler for 10-15 minutes. While waiting for the rinsing step to complete, SC-2 solution can be prepared.

2. SC-2.

   SC-2 serves to remove inorganic / metallic contaminants from the Si wafer surface. First, 300 ml DI water is heated to 80-90°C. Then, 50 ml

hydrogen peroxide (H_2O_2, 31 wt.%) and 50 ml hydrochloric acid (HCl, 37 wt.%) are added to the solution. The Si wafers are then immersed in the solution for 10-15 minutes. Afterwards, they are rinsed in flowing DI water with bubbler for 10-15 minutes.

After the SC-2 step, the Si surface is passivated by a 1.5-nm-thick carbon-free oxide layer,[59] which should only be removed right before further processing steps. The oxide removal is carried out by immersing the wafer in 10 wt.% HF for 5-10 seconds.

On many occasions, not all the wafers will be used at the same time. Since the oxide layer grown on the Si surface after the SC-2 step is very thin, the Si surface can attract new contaminants when left unprocessed for a long period of time. Therefore, after the SC-2 step, the grown oxide layer can be stripped in 10 wt.% HF and immediately loaded into an oxidation furnace to grow a thick oxide layer. This oxide layer serves as a protective layer from any possible surface contaminants and can be conveniently removed in HF when the wafers are about to be used for further processing steps.

The oxidation system (Tystar Model Mini Tytan) used in this work is schematically depicted in **Figure 3.1**. There are two types of oxidation, namely dry and wet oxidation.[60] Dry oxidation uses O_2 feed gas to induce the chemical reaction of $Si + O_2 \rightarrow SiO_2$. Wet oxidation uses H_2O bubbler coupled with O_2 carrier gas to oxidize the Si according to the reaction of $Si + 2H_2O \rightarrow SiO_2 + 2H_2$. Since the new oxide forms at the Si/SiO_2 interface,[61] the oxide growth rate becomes slower (diffusion-limited) as the oxide becomes thicker. The diffusion-limited regimes for dry and wet oxidation are

approximately 4 and 100 nm, respectively.[60] For this reason, dry oxidation is typically used to grow a thin oxide layer while much thicker oxide is more practical to grow using wet oxidation. We typically grow 85-nm oxide on the Si using wet oxidation at 900°C for 24 minutes.

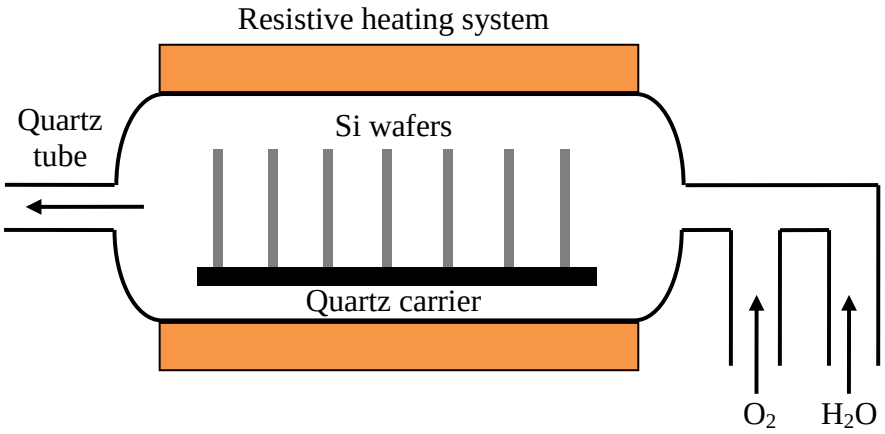

Figure 3.1: Schematic of a Si oxidation system.

3.3 Lithography

We used a thin Ultra-i 123 photoresist (PR) coating on Si for subsequent lithographic steps. First, the Si wafer is mounted on a vacuum chuck. Then, the PR is dispensed onto the Si wafer until it covers the entire wafer. Two-step spinning is employed in our experiments. The first spinning step is carried out at 500 rpm with an acceleration of 560 rpm/sec for 2 seconds, and serves to uniformly spread the PR across the whole wafer surface. The second spinning step is carried out at *x* rpm with an acceleration of 1680 rpm/sec for 58 seconds to achieve the desired resist thickness. After spincoating, the sample is softbaked at 90°C on a hotplate for 90 seconds. We have calibrated the resulting Ultra-i 123 thickness (0.35 dilution) for various values of *x*, as shown in **Figure 3.2**.

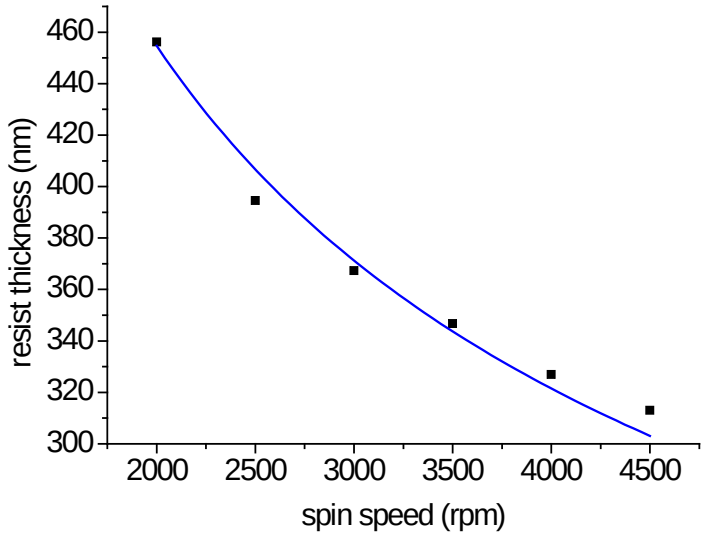

Figure 3.2: Ultra-i 123 softbaked thickness vs. spin speed.

The interference lithography (IL)[62,63] system used in this work is of the Lloyd's mirror configuration,[19] as schematically shown in **Figure 3.3**, with a HeCd laser source (λ = 325 nm). The mirror is fixed at right angle with the substrate by a rigid frame. By rotating the frame to a certain angle (θ), the incoming laser beam will interfere with the beam reflected from the mirror on the substrate so as to result in a standing wave with a spatial period (*p*) given by,

$$p = \frac{\lambda}{2 \sin \theta}$$ **Equation 3.1**

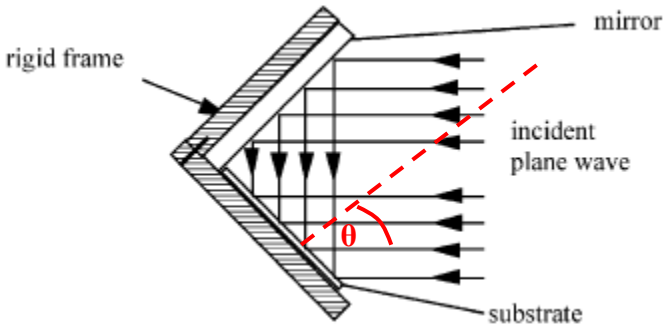

Figure 3.3: Lloyd's mirror configuration for interference lithography.[63]

After exposure, the sample is baked at 110°C for 90 seconds and developed in Microposit MF CD-26 developer for 60-90 seconds to produce the PR patterns. **Figures 3.4a** to **c** show possible geometries generated using IL. Single exposure results in lines, two exposures with angle of 90° between exposures result in dots, and two exposures with acute angle between exposures result in fins.

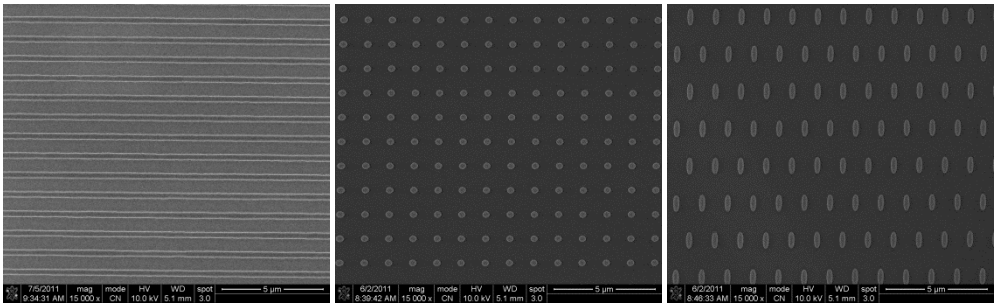

(a) (b) (c)

Figure 3.4: (a) Line, (b) dot, and (c) fin PR patterns generated using interference lithography on a Si substrate.

We have also used optical lithography to fabricate samples for our etching experiments. The optical lithograhy system (SUSS MicroTec MJB4) is schematically depicted in **Figure 3.5a**. It can operate in contact or proximity mode and uses a UV light source of 320-nm wavelength. We employed contact printing[4] for the exposure of the PR layer. After exposure, the sample is baked at 110°C for 90 seconds and then developed in Microposit MF CD-26 developer for 60-90 seconds to produce the PR patterns. Example of PR ring pattern is shown in **Figure 3.5b**.

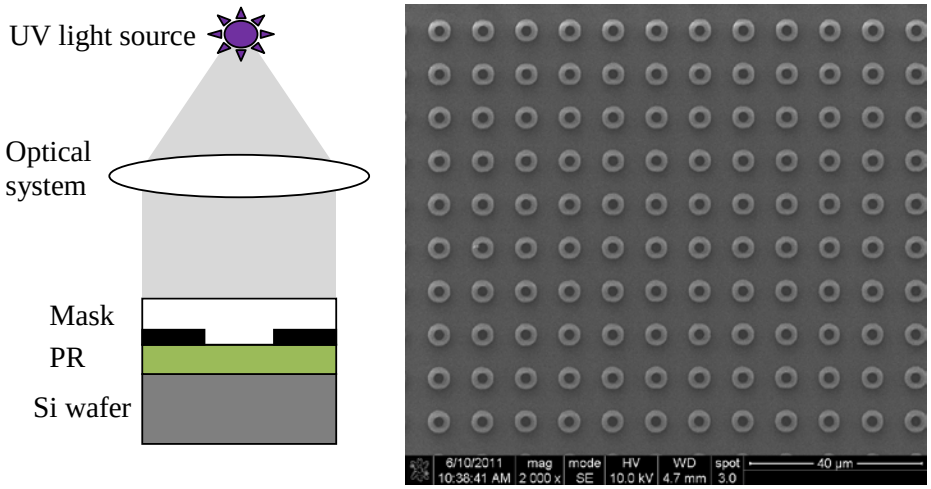

(a) (b)

Figure 3.5: (a) Optical lithography using contact printing exposure method. (b) PR ring patterns on Si.

After development, there can still be residual PR layer which can be detrimental in two aspects. First, MACE requires an intimate contact between Au and Si. Therefore, the presence of a thin residual PR layer between Au and Si will block the etching process. Second, Au patterns are obtained by first depositing Au film on the PR patterns and then selectively removing the Au-coated PR patterns. If there is a thick residual PR layer prior to Au deposition, it could result in complete removal of the Au film.

For this reason, an oxygen plasma etching step is necessary after PR development. Our plasma etching system (SAMCO Model PD-2400) is schematically depicted in **Figure 3.6**. A radio-frequency (RF) generator sets up a potential difference between electrodes and ionizes the oxygen gas, i.e. creating a gas plasma. These ionized oxygen molecules react with the PR to convert the polymer to carbon dioxide and water,[64] which are then pumped out of the system.

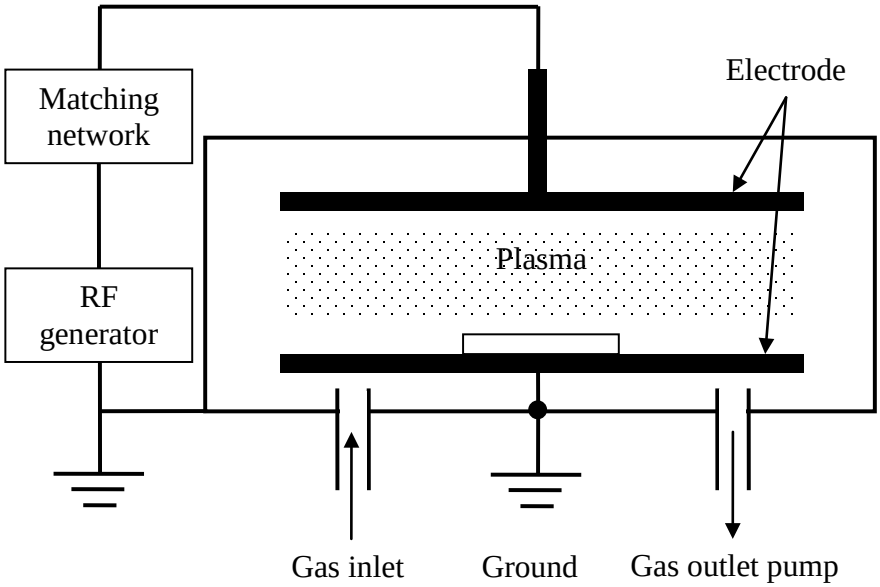

Figure 3.6: Schematic diagram of an RF-powered plasma etch system.

3.4 Thermal Evaporation

Au is deposited on the PR patterns using evaporation process because of its unidirectional deposition flux. Unidirectional flux is necessary to minimize sidewall coating on the PR patterns and hence, will facilitate the subsequent lift-off process. A schematic diagram of the thermal evaporator (Edwards Auto306 FL400) used in this work is shown in **Figure 3.7**. First, a Au wire of 7-10 mm in length is loaded into the tungsten boat and the chamber is pumped down using two-stage pumping systems. Rough pumping brings the chamber pressure to ~ 10^{-1} Torr before fine pumping takes over to lower the pressure to 10^{-6} Torr range within 1-2 hours. The tungsten boat is then resistively heated by increasing the current slowly to ~ 4 A. During the process, the Au wire can be seen to melt. After the rate monitor shows a stable value of 0.02-0.03 nm/sec, the shutter can be opened and Au will be deposited on the sample until

it reaches the desired thickness. 7-mm Au wire is sufficient to deposit ~ 20-nm Au film within a duration of ~ 20 minutes.

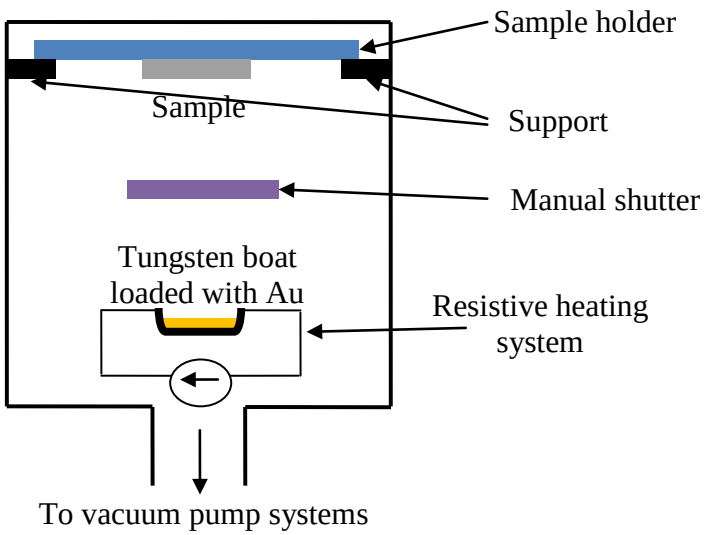

Figure 3.7: Schematic diagram of a thermal evaporator.

3.5 Lift-off

After Au deposition, the Au-coated PR patterns must be selectively removed to leave behind only the Au patterns on Si. This process is called lift-off, as schematically shown in **Figure 3.8**. First, an ultrasonic bath (Branson B2510DTH) is filled with water up to the allowed operating level. Then, the sample is put upside down on the sample holder (with perforations to allow the liquid to penetrate from below) and immersed in an acetone-filled beaker in the bath. After subjected to ultrasound agitation (40 kHz) for about 10 minutes, the PR patterns should be completely removed, leaving behind the inverse patterns on the Au film. Typical results before and after lift-off are shown in **Figures 3.8b** and **c**, respectively.

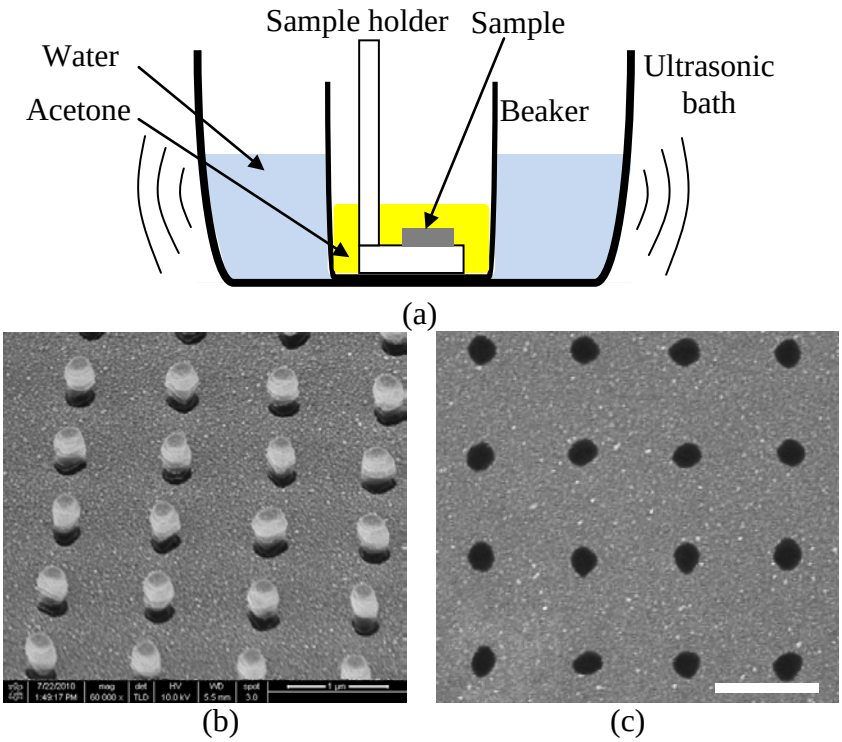

Figure 3.8: (a) Schematic diagram of an ultrasonic bath. (b) Tilted view of PR patterns coated with Au before lift-off. (c) Top view of inverse PR patterns on Au after lift-off. Scale bar is 1 μm.

3.6 Metal-Assisted Chemical Etching of Silicon

After lift-off, the samples are ready for MACE. The etchant consists of a mixture of H_2O, HF, and H_2O_2. Since HF is known to attack glass,[65] Pyrex beaker cannot be used for the etching experiment and the etchant must instead be placed in a Teflon beaker, as shown in **Figure 3.9**. The samples (with the Au patterns facing up) are put inside a Teflon sample holder which has perforations to allow the etchant to seep from beneath. The importance of exposing the back side of the sample to the etchant will become clear in the next chapter.

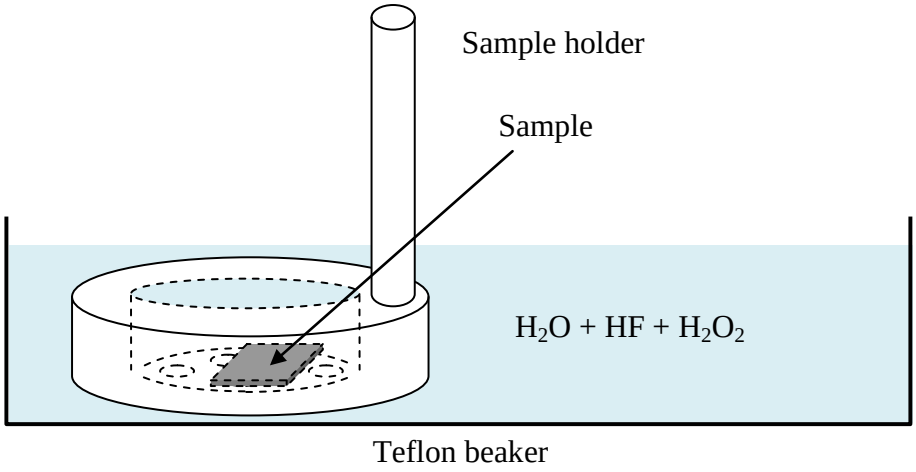

Figure 3.9: Schematic illustrating MACE experiment.

3.7 Scanning Electron Microscopy

The surface morphology of the samples was characterized using two types of scanning electron microscopes (SEM): FEI Nova NanoSEM 230 and Philips XL 30 FEG. The working principle of image collection in SEM is depicted in **Figures 3.10a** and **b**. When a primary electron beam of energy E_0 (typically with an acceleration voltage < 30 kV) is incident on a sample, the kinetic energy is lost via multiple inelastic scattering to generate many secondary electrons (SEs). These SEs are brought to rest within the interaction volume (or penetration depth), as shown in **Figure 3.10a**. Some of the SEs near the surface (within an escape depth λ), however, can escape to vacuum as a signal for the detector. The value of λ is very small (~ 2 nm) and therefore, SE image gives the surface structure (topography) of a sample.[66]

Figure 3.10b shows that the number of escaping SEs per primary electron (called SE yield) depends on the angle (ϕ) between the primary electron and the surface. This is because for an inclined surface (B), the volume from which the SEs can escape is larger than that of a flat surface as

can be seen by comparing the hatched area in B and A. This means that protrusion or recess features will appear brighter than their surroundings even though they are constituted from the same material. **Figure 3.10c** shows a Si nanowire array fabricated on Si substrate using MACE. It can clearly be seen that the nanowires appear brighter than the Si background due to the difference of SE yield explained above.

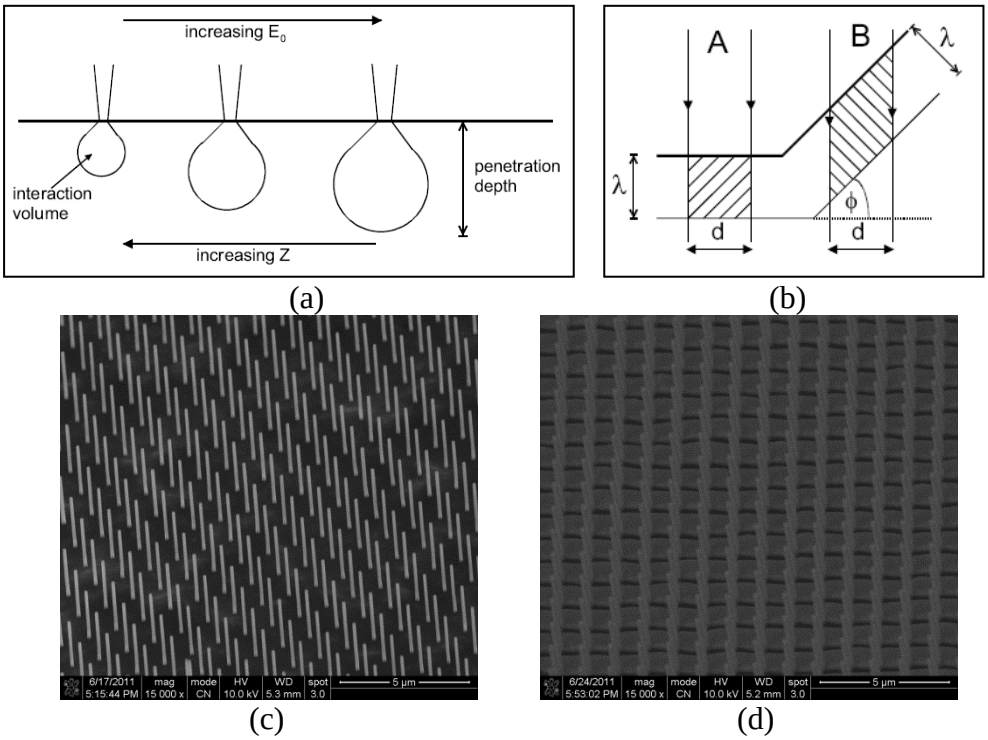

Figure 3.10: (a) Schematic dependence of the interaction volume and penetration depth as a function of incident energy E_0 and atomic number Z of the incident (primary) electrons.[66] (b) SEM incident beam that is normal to a specimen surface (at A) and inclined to the surface (at B).[66] (c) Si nanowires fabricated on Si substrate using MACE. (d) The same nanowire array which has been shadow-evaporated with nickel (Ni).

Figure 3.10a also shows that the interaction volume increases with E_0 because more scatterings can occur for higher-energy electrons, and decreases with the sample atomic number (Z) because more atoms are available per unit volume to slow down the primary electrons. The dependence on Z implies that materials with different atomic number can also create a contrast in SEM

images. **Figure 3.10d** shows the same Si nanowire array (**Figure 3.10c**) which has been coated with nickel (Ni) using shadow-evaporation method. It can be seen that the Ni-coated background appears brighter than the uncoated Si region because Z_{Ni} (= 28) is higher than Z_{Si} (= 14). It should be noted, however, that to obtain strong atomic-number-contrast image, the SEM is typically operated under backscatter mode because the cross section for high-angle elastically backscattered electron is proportional to Z^2.[66]

Chapter 4. Mechanism and Stability of Catalyst in Metal-Assisted Chemical Etching

4.1 Introduction

In recent years, metal-assisted chemical etching (MACE) of Si has emerged as a promising low-cost alternative 3D fabrication method. This method involves the etching of Si in a mixed solution of HF and H_2O_2 with noble metal catalyst,[19,23] and it has successfully produced tilted and zigzag nanowires,[54,67] nanocones,[21] helical holes,[24,32] and cycloidal[25] and spiral trenches.[25,52] Among all the reports on MACE, it is worthwhile to distinguish two distinct catalyst configurations, namely the isolated catalysts (e.g. nanoparticles[24,32] or nanopatterns[25,33,52]) and the interconnected catalysts (e.g. perforated films[19,20,44]).

For work on MACE using isolated catalysts, it was observed that[24,32] the direction of Pt or Ag nanoparticles can significantly deviate from directions normal to the original surface. When Au nanopatterns[25,33] (~0.5 μm^2) are used as catalysts, the etching direction into the Si is intimately related to the geometry of the catalysts. In fact, Wong *et al.* demonstrated that controlled 3D motion of catalyst patterns during MACE can only be achieved by locally pinning them with an electrically insulating material prior to etching.[33,68,69]

The second type of MACE of Si makes use of a layer of perforated Au film on Si surface (i.e. the anti-dot configuration).[19,20,44] With the anti-dot configuration, the Au film causes etching in uniform direction relative to the substrate leaving behind nanowires and nanofins. Note that a controlled etching direction of nanopatterns has also been achieved by Wong *et al*. *but*

with the nanopatterns pinned. These results therefore point to an intriguing fact that the configuration of catalyst, i.e. isolated or interconnected, is intimately related to whether the etching direction is uniform.

In this chapter, we report results of a systematic study on the mechanism and catalyst stability of metal-assisted chemical etching (MACE) of Si in HF and H_2O_2 using isolated Au catalyst. The role of electronic holes on etching of Si underneath a Au catalyst is presented. The role of excess holes is characterized through the observation of pit formation as a function of catalyst proximity and the ratio of the H_2O_2 and HF concentrations in the etch solution. We show that suppression of excess hole generation, and therefore pitting, can be achieved by either adding NaCl to the etch solution or by increasing the HF concentration relative to the H_2O_2 concentration.

We also demonstrate that an external electric field can be used to direct most of the excess holes to the back of the Si wafer, and thus reduce pit formation at the surface of the Si between the Au catalysts. We also explore the role of Au back contact on the etching characteristics for three different cases: (i) back contact is exposed to the etchant, (ii) back contact is not exposed to the etchant, and (iii) etching with an additional current injection from an applied bias. Next, we propose that there are two possible causes for catalyst instability during MACE, namely the overlap of excess holes between neighboring catalysts and the generation of hydrogen (H_2) bubbles. From these two modes of instability, we define a regime of etch chemistry and catalyst spacing for which catalyst stability and vertical etching can be achieved.

4.2 Experimental Details

p-type Si (100) wafers with resistivity 4–8 Ω.cm were used for the MACE experiments. The wafers were cleaned in SC-1 and SC-2 solutions and dipped briefly in 10 wt.% HF before lithographic steps. The basic process flow for the preparation of samples for subsequent MACE experiments is shown in **Figure 4.1a**. First, an Ultra-i 123 photoresist layer of ~ 400-nm thickness was spin coated on the Si wafer and baked at 110°C for 1.5 minutes. The photoresist was then exposed using a UV mask aligner (SUSS MicroTec MJB4), baked at 110°C for 1.5 minutes, and developed in Microposit MF CD-26 developer for ~ 1 minute to generate patterns in the photoresist. The patterns consist of sets of rectangles (2 μm × 100 μm) of different spacings (2, 5, 9, 13, 17, and 20 μm) as shown schematically in **Figure 4.1b**.

The samples were then subjected to an oxygen plasma etch at a pressure of 0.2 Torr and power of 200 W for an etching time of 30 seconds to remove any residual resist layer after development. An Au layer (~18 nm) was then deposited on the resist patterns using a thermal evaporator (Edwards Auto306 FL400) at a base pressure of ~ 10^{-6} Torr. The samples were subsequently put in an ultrasonic bath for 10 minutes to lift off the photoresist patterns, leaving behind Au strips on the Si. Typical SEM images of the Au strips with strip spacings of 2, 13 and 20 μm are shown in **Figures 4.1c** to **e**, respectively. The samples were then etched in a mixed solution of H_2O, H_2O_2 and HF of different proportions at room temperature. The surface morphologies of the Au catalysts and the Si between the Au strips were examined using scanning electron microscopes (FEI Nova NanoSEM 230 and Philips XL 30 FEG).

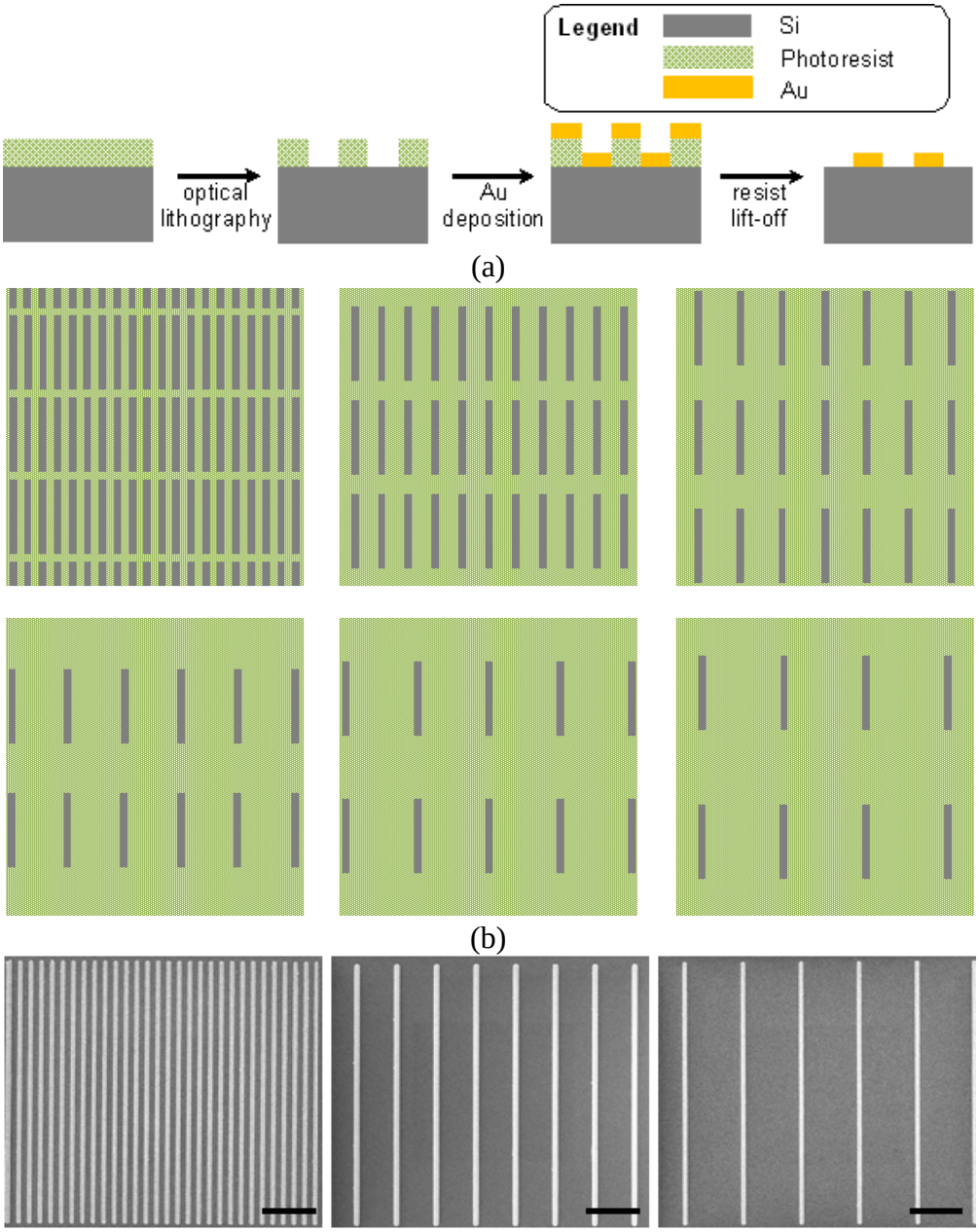

Figure 4.1: (a) Process steps for fabrication of Au strips using optical lithography. (b) Schematic of photoresist patterns with different spacings. (c)-(e) SEM images of Au strips with spacings of 2, 13 and 20 µm. The scale bar for the SEM images is 20 µm.

4.3 Role of Electronic Holes on Etching Underneath Au

The MACE process involves a pair of redox reactions at the cathode (Au–liquid interface) and anode (Au-Si) interfaces,[29]

Cathode: $\frac{n}{2}H_2O_2 + nH^+ \rightarrow nH_2O + nh^+$

Equation 4.1

and

Anode: $Si + 6HF + nh^+ \rightarrow H_2SiF_6 + nH^+ + \left(\frac{4-n}{2}\right)H_2$

Equation 4.2

so that

Balanced reaction: $Si + 6HF + \frac{n}{2}H_2O_2 \rightarrow H_2SiF_6 + nH_2O + \left(\frac{4-n}{2}\right)H_2$

Equation 4.3

H_2O_2 is reduced at the Au surface as Au is negatively charged[70] for pH > 3 in all possible HF concentrations,[71] and this attracts H^+ ions to the vicinity of Au catalyst. This reaction produces water and at the same time injects holes (h^+) through the Au catalyst into Si. At the anode (Au-Si interface), the Si atoms underneath the Au catalyst are oxidized by the holes and dissolve in the HF solution as H_2SiF_6. H^+ ions and H_2 gas are also produced at the anode.

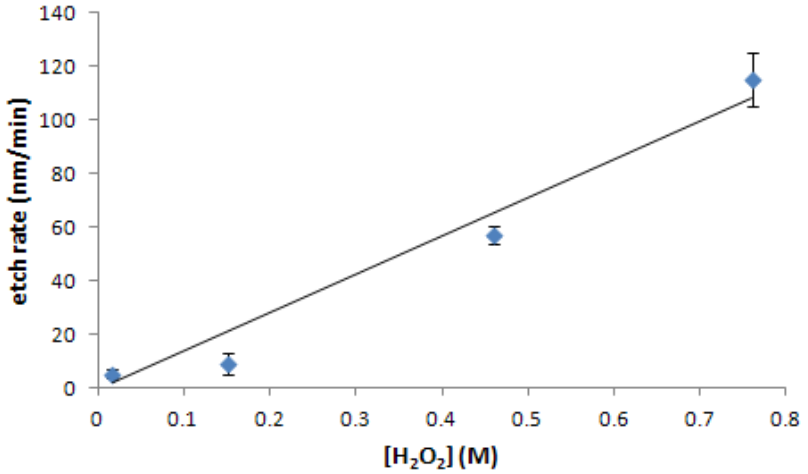

Figure 4.2: Si etch rate versus the H_2O_2 concentration for Au strips with 2-µm spacing with fixed [HF] = 1.73M.

Figure 4.2 shows etch rate results for samples with an Au strip spacing of 2 µm as a function of the H_2O_2 concentration for [HF] = 1.73 M. It can be seen that the etch rate increases linearly as the H_2O_2 concentration is

increased. This is expected as an increase in [H_2O_2], in the range in which the HF supply is abundant, will provide an increasing number of holes to oxidize the Si and cause the etch rate to increase.

4.4 Role of Excess Holes on Pit Formation

As HF can only access the Si from the edge of the catalyst, this allows a certain number of holes (especially in the middle region underneath the catalyst) to diffuse away from the catalyst, as shown in **Figure 4.3a**. These excess holes will diffuse to locations away from the Au strip and then oxidize Si atoms at the Si surface between strips. These oxidized portions will then be etched by HF resulting in the formation of pits. To study pit formation in our samples, we have identified two different regions at the Si surface between adjacent Au strips: Region A (of 1 μm width half way between the two adjacent Au strips) and Region B (of 1 μm width along the edges of the Au strips), as illustrated in **Figure 4.3b**.

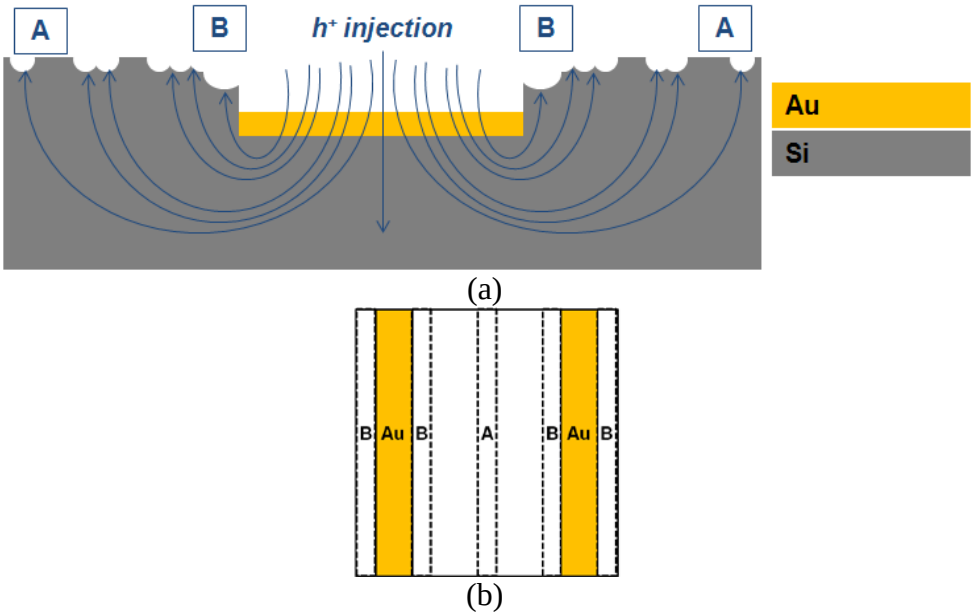

Figure 4.3: (a) Schematic of hole injection into Si during MACE. (b) Definitions of regions A and B.

4.4.1 Influence of Catalyst Spacing

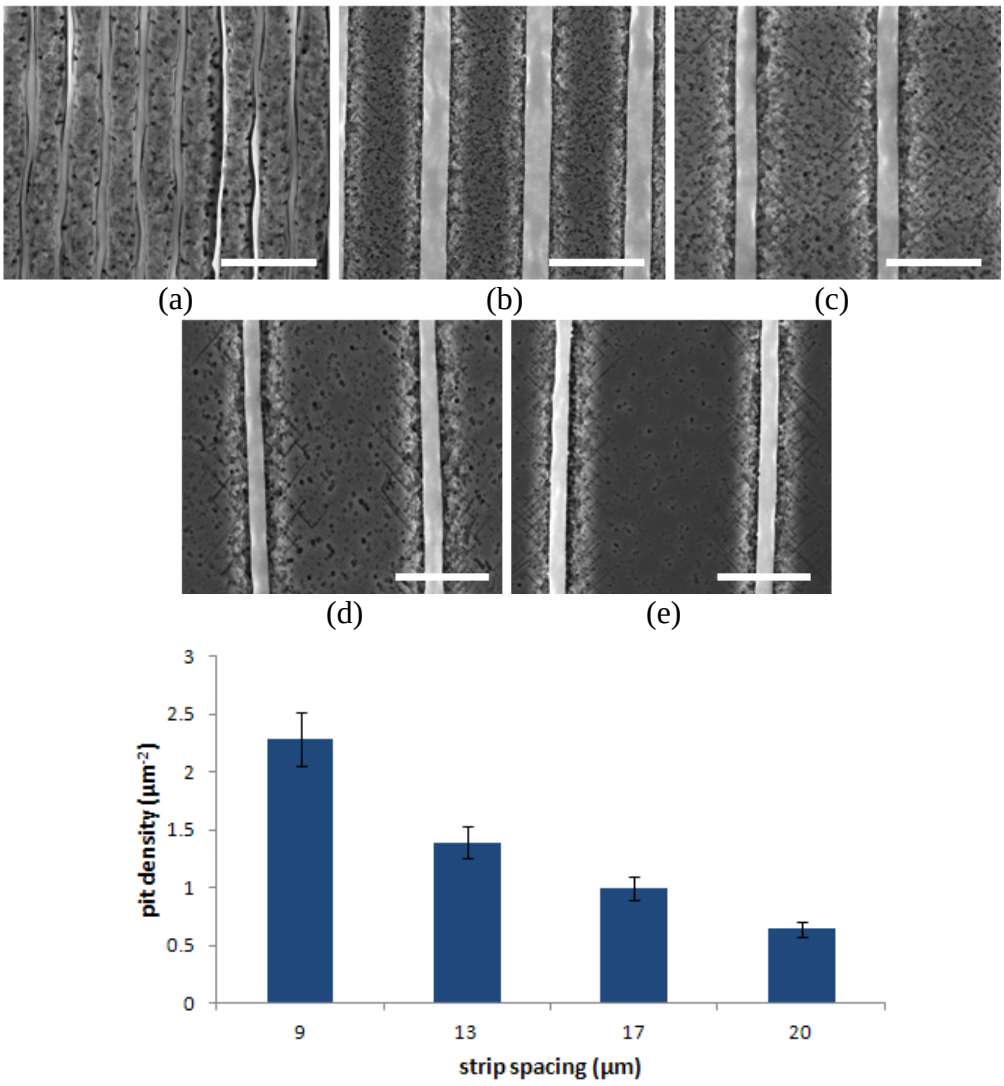

Figure 4.4: (a)-(e) Top-view SEM images of etched samples with strip spacings 2, 9, 13, 17, and 20 μm, respectively. The [HF] and [H_2O_2] were fixed at 1.73 and 1.21 M, respectively, and the etch duration was 15 minutes for (a) and 20 minutes for (b) through (e). The scale bar for the SEM images is 10 μm. (f) Comparison of pit density in Region A for samples shown in (b) through (e).

Figures 4.4a to **e** show the SEM images of the Si surface between Au strips with strip spacings of 2, 9, 13, 17, and 20 μm. It is reasonable to assume that the concentration of excess holes in the Si decreases with distance from the Au edges. This means that a much higher concentration of holes will be found in Region B compared to Region A. As a result, there should always be

more etching of Si in Region B than Region A. This is in agreement with all the SEM images shown in **Figures 4.4a** to **e**. However, it should be noted that for the sample with strip spacing of 2 μm, Regions A and B become indistinguishable, probably caused by a significant overlap of regions with high excess hole concentrations. For samples with larger strip spacing, Region A becomes smoother (i.e. has fewer pits). This is confirmed by the pit density shown in **Figure 4.4f**.

4.4.2 Influence of [H_2O_2]

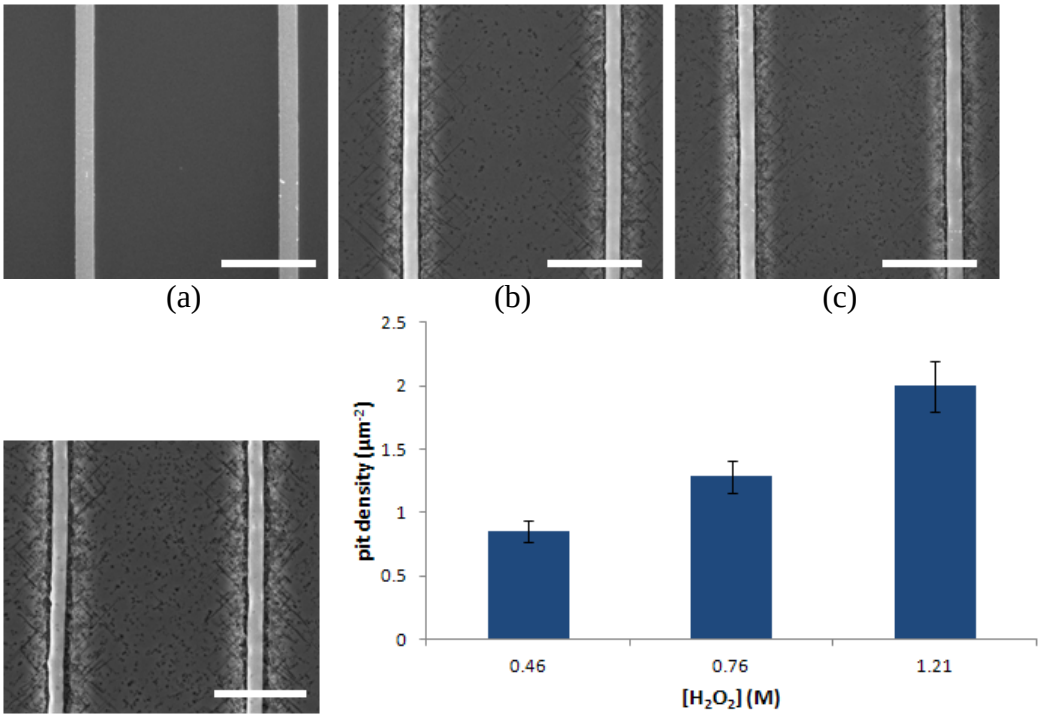

Figure 4.5: (a)-(d) Top-view SEM images of etched samples with a strip spacing of 20 μm, etched with H_2O_2 concentrations of 0.15, 0.46, 0.76, and 1.21 M. [HF] was fixed at 1.73 M and the etch duration was 15 minutes. The scale bar for the SEM images is 10 μm. (e) Comparison of pit density in Region A for samples shown in (b) to (d).

We have also varied the flux of holes by changing the H_2O_2 concentrations in our etching experiments. **Figures 4.5a** to **d** show the pit distributions for samples with a strip spacing of 20 μm and etched for 15

minutes with $[H_2O_2]$ = 0.15, 0.46, 0.76, and 1.21 M. First, we observe that the Si surface between the Au strips is very smooth for the etching experiment with $[H_2O_2]$ = 0.15 M. For low H_2O_2 concentrations (e.g. 0.15 M), there are very few extra holes available for the formation of pits, and thus the Si surface between the strips is very smooth. As the concentration of H_2O_2 is increased from 0.46 to 1.21 M, more extra holes are available and pits form in Region A, as shown in **Figures 4.5b** to **d**. This is in agreement with the results of **Figure 4.5e,** which shows that the pit density increases with increasing H_2O_2 concentration.

4.5 Control of Excess Holes

We have shown that excess holes are responsible for the formation of pits at locations away from the catalyst. We will now explore three possible ways to control these excess holes, namely addition of NaCl, increase in [HF], and application of electric field.

4.5.1 Addition of NaCl

One way to vary the injection rate of holes is to vary the supply of H^+ ions at the Au-liquid surface. This can be achieved by adding NaCl to the etching solution.[72] **Figure 4.6a** shows a schematic of the influence of adding NaCl to the etching solution. NaCl can readily dissociate into Na^+ and Cl^- ions and the Na^+ ions are attracted to the negatively charged Au surface. As H^+ ions are required for the generation of holes at the cathode, the presence of Na^+ ions reduces the number of H^+ ions at the Au surface and hence the number of holes injected into Si. This will result in (i) a reduction of the etch rate of the

Si underneath the Au strips and (ii) a concomitant reduction in the injection rate of excess holes, thereby suppressing pit formation at the Si surface between the Au strips. **Figures 4.6b** and **c** compare the Si surfaces for etching without and with the addition of 10mM NaCl to the etching solution, respectively. **Figure 4.6c** clearly shows that there is a significant reduction in pit formation when NaCl is added. The etch rate was also found to decrease from 95 nm/min (from **Figure 4.6b**) to 22 nm/min (from **Figure 4.6c**). To make sure that the smooth Si surface shown in **Figure 4.6c** was not due to reduction in the etch rate, another sample was etched to a comparable depth (a depth of 0.9 µm achieved in 21 minutes, as shown in **Figure 4.6d**) and the Si surface was still found to be smoother than in the case when NaCl was not added (as shown in **Figure 4.6b**).

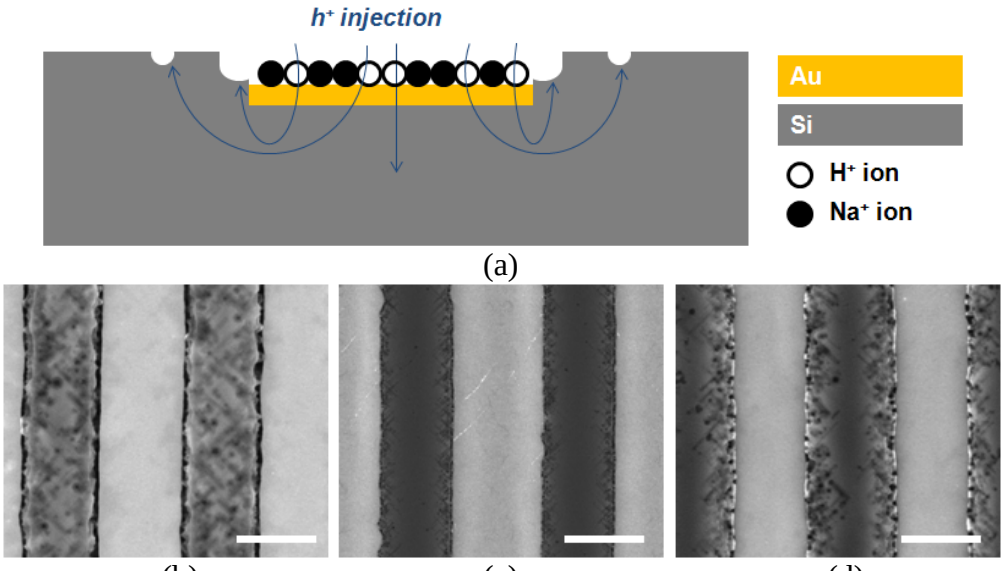

Figure 4.6: (a) Schematic diagram illustrating the effect of adding NaCl to etching solution. Na^+ adsorption at the Au-liquid interface suppresses H^+ adsorption and the injection of holes into the Au and Si. (b)–(d) Top-view SEM images of samples with a 2-µm Au strip spacing; (b) without NaCl in the etching solution and etched for 10 minutes, (c) with 10mM NaCl in the etching solution and etched for 10 minutes, (d) with 10 mM NaCl in the etching solution and etched to reach a depth of 0.9 µm. [HF] and [H_2O_2] were fixed at 1.73 and 0.46 M, respectively. The scale bar for the SEM images is 2 µm.

4.5.2 Increase in [HF]

We also consider the effect of HF concentration on pit formation in the MACE process. When HF supply is increased, more holes are consumed beneath the catalyst and fewer holes can diffuse away and form pits. It is therefore expected that the etch rate of Si should increase and the formation of pits at the Si surface between the Au strips should be reduced with an increase in [HF]. **Figures 4.7a** and **b** show the Si surface condition between Au strips with a spacing of 2 μm for [HF] = 1.73 and 27.5 M, respectively. As can be seen, there is a drastic change in the Si surface condition from pitted to smooth. The etch rate was also found to increase from 130 nm/min to 280 nm/min when [HF] was increased from 1.73 to 27.5 M.

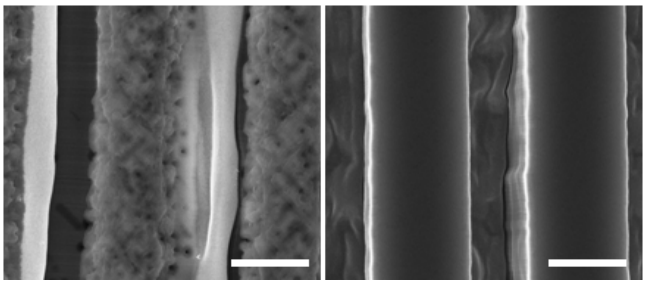

(a) (b)

Figure 4.7: Top-view SEM images of samples with Au strips of 2-μm spacing and etched with HF concentrations of (a) 1.73 M and (b) 27.5 M. The H_2O_2 concentration was fixed at 0.46 M and the samples were etched for 15 minutes. The scale bar for the SEM images is 2 μm.

4.5.3 Effect of Electric Field

Figure 4.8a shows a schematic of the experimental set-up used to manipulate the excess holes in an electric field. The H_2O_2 and HF solution was placed inside a flexible plastic container (a plastic pipette bulb) and the Si sample with Au strips was immersed inside the solution. The plastic container was pressed between two copper plates to obtain a gap between the plates of

2–3 mm, as shown in **Figure 4.8a**. The electric field across the etching solution could then be varied by changing the potential applied (*U*) across the two metal plates.

Figures 4.8b, **c** and **d** show SEM images of three samples etched with [HF] = 1.73 M and [H_2O_2] = 1.21 M with *U* = 0, 10 and 100 V. For the sample with *U* = 0 V, excess holes diffused into Regions A and B (see **Figure 4.8b**) to form pits as described in **Section 4.4**. With *U* = 10 V, the excess holes are drawn toward the bulk of Si resulting in less pitting in Regions A and B. As shown in **Figure 4.8d**, the effect of the electric field in drawing the holes to the bulk of Si is even more significant for *U* = 100 V.

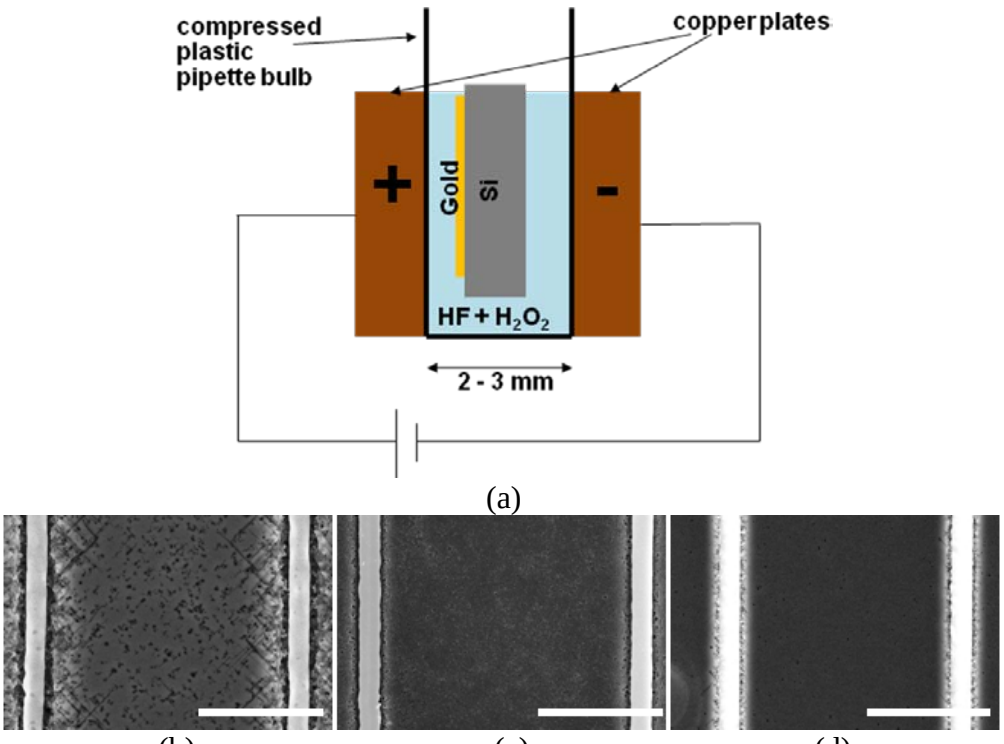

Figure 4.8: (a) Schematic illustration of the experimental set-up used for studies of etching in the presence of an external electric field. (b)–(d) Top-view SEM images of samples with an Au strip spacing of 20 μm etched for 15 minutes in [HF] = 1.73 M and [H_2O_2] = 1.21 M with *U* = 0, 10, and 100 V, respectively. The scale bar for the SEM images is 10 μm.

It was also found that the etch rate decreased with increasing electric field. For samples etched with U = 0, 10 and 100 V, the etch rates were 0.12, 0.03, and 0.023 μm/min, respectively. Similar results were obtained from the same etching experiments but with $[H_2O_2]$ = 0.46 M (see Appendix A). These results suggest that in the presence of the electric field, either fewer holes are generated at the Au/Si interface, or fewer of the holes generated at the interface cause a reaction there.

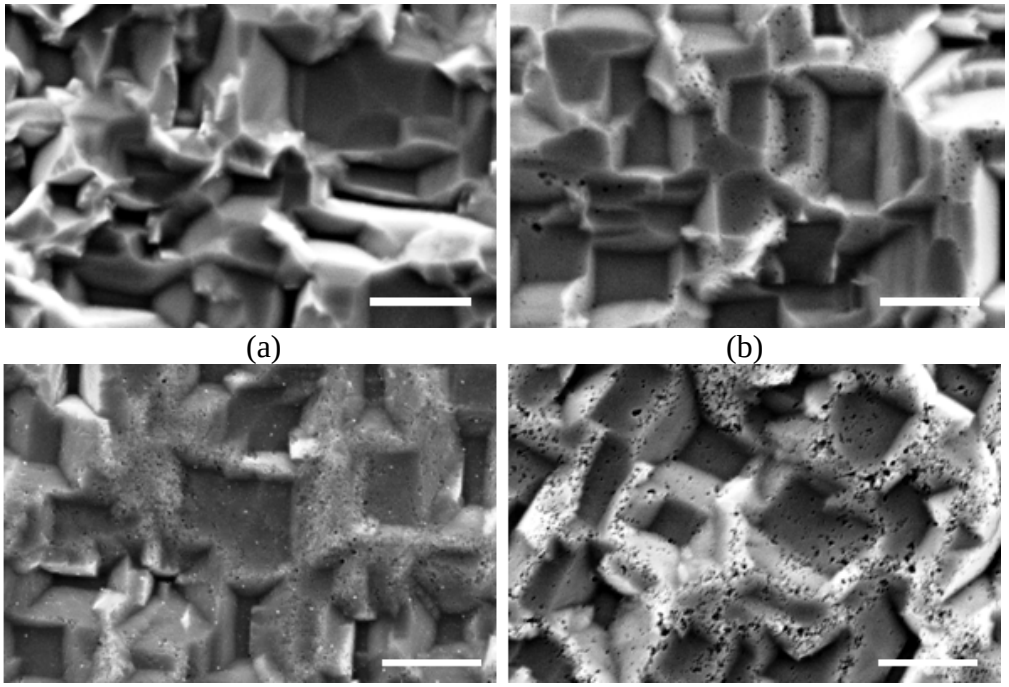

Figure 4.9: (a) SEM images of the backside surface of a virgin Si sample. (b)–(d) Backside surface of samples with an Au strip spacing of 20 μm etched for 15 minutes in [HF] = 1.73 M and $[H_2O_2]$ = 1.21 M, with U = 0, 10, and 100 V, respectively. The scale bar for the SEM images is 5 μm.

One would expect some of the holes being drawn by the electric field to the bulk of the Si to reach the back side of the Si wafer and hence result in pit formation. **Figure 4.9a** shows a SEM image of the back side of a virgin sample. The rough back side surface is expected as the Si wafer was only polished on the opposite side. It is interesting to compare the SEM images (see

Figures 4.9b, **c** and **d**) of the back side of three samples etched with [HF] = 1.73 M and [H_2O_2] = 1.21 M with U = 0, 10 and 100 V. With U = 0, most of the holes were consumed at the front side of the wafer, giving rise to pits in Regions A and B, and few pits are observed on the back side of sample. The pit density clearly increases when U is increased to 10 or 100 V. This is expected as higher electric field will cause more holes to reach the back side of sample.

4.6 Role of Au Back Contact

Since the reduction of H_2O_2 or the generation of holes (**Equation 4.1**) is greatly facilitated in the presence of Au, as explained in **Section 4.3**, we have also explored the role of Au back contact on the etching characteristics at the front side of the sample where the Au patterns are located. For this purpose, we use a different catalyst configuration obtained through the process flow described in **Figure 4.10**. First, lithographic exposure was carried out to expose the Si strips of 20-μm spacing beneath the PR layer. Then, another exposure was carried out, with the upper half of the sample covered with a piece of Si wafer, to generate the Si finger pattern. Subsequently, 18-nm Au was deposited on the sample, followed by a lift-off process to obtain Au fingers on Si. The function of the large pad at the base of each Au strip is to enable the application of an electrical bias. Finally, Au film of 18-nm thickness was also deposited on the back side of the sample to form a back contact. Care was taken to ensure that the edges were not coated with Au to avoid any current shorting with the Au patterns on the front side of the sample.

We have examined three different cases for this catalyst configuration: (i) back contact is exposed to the etchant, (ii) back contact is not exposed to the etchant, and (iii) etching with an additional current injection from an applied bias.

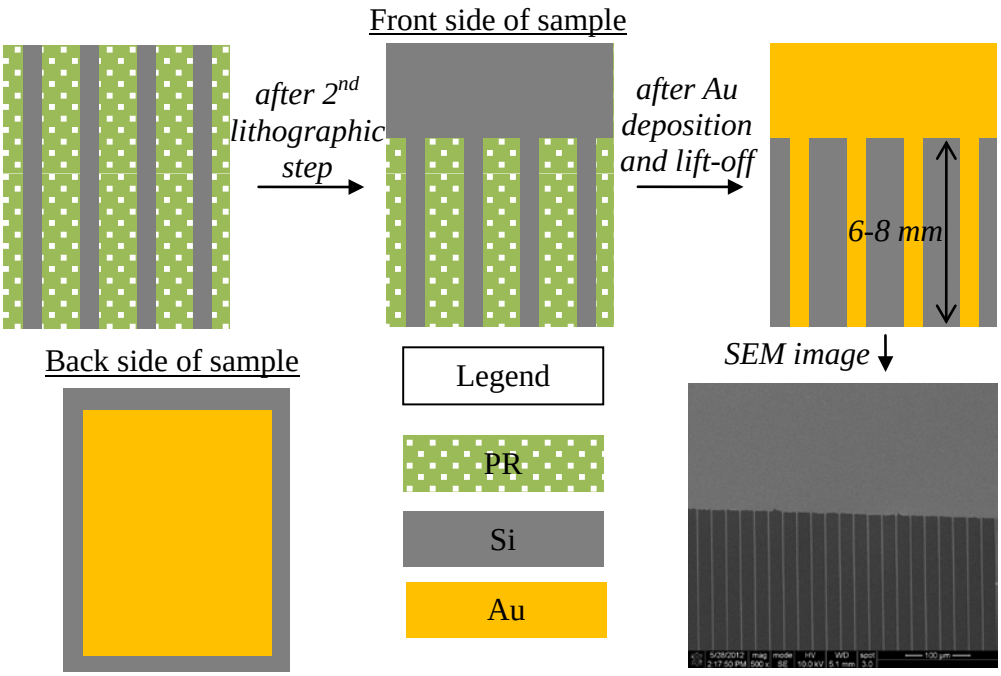

Figure 4.10: Process steps to fabricate Au fingers with Au back contact.

4.6.1 Double-Sided Hole Injection

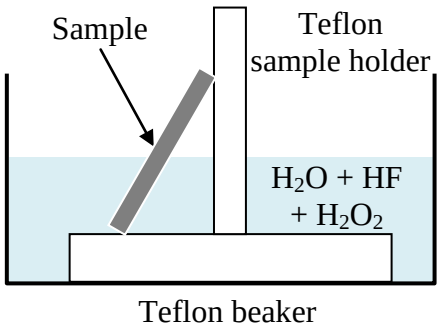

Figure 4.11: Schematic illustrating MACE experiment for Au fingers with Au back contact. The large Au pad is not immersed in the etchant solution.

To examine the role of Au back contact, the samples were etched in a configuration shown in **Figure 4.11**. The large Au pad was not immersed in

the etchant solution to isolate any possible influence of the pad on the etching characteristics.

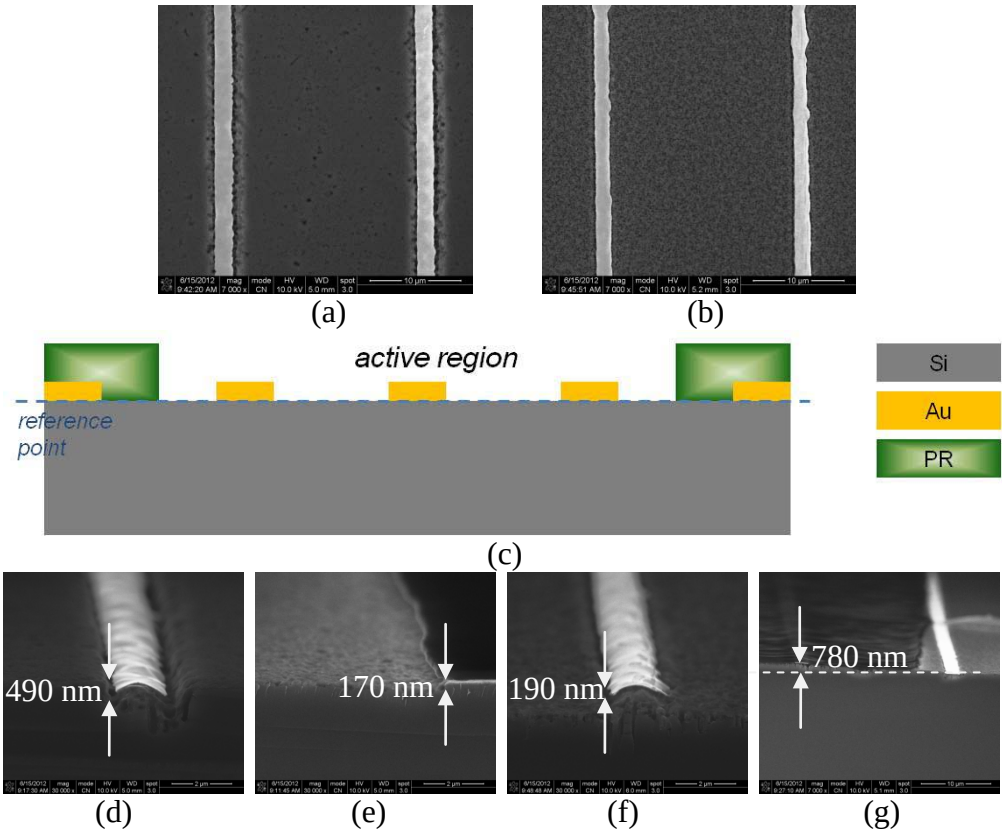

Figure 4.12: (a) and (b) are top-view SEM images of samples etched for 15 minutes with and without Au back contact, respectively. [H_2O_2] and [HF] were fixed at 1.21 and 1.73 M, respectively. (c) Schematic illustrating the creation of a PR step to obtain an absolute etch depth measurement. (d) and (e) are cross-sectional SEM images of sample etched without Au back contact at the active region and the reference point, respectively. (f) and (g) are cross-sectional SEM images of sample etched with Au back contact at the active region and the reference point, respectively.

Figures 4.12a and **b** show the top-view SEM images of the samples etched with and without Au back contact, respectively. Without back contact, regions A and B are clearly distinguishable for the reason explained in **Section 4.4**. With back contact, however, numerous pits are formed uniformly between the Au strips, i.e. no regions A and B. This is because the back contact provides an additional source of hole injection to the front side of the sample.

Since the back side of sample is thoroughly coated with Au, it is expected that the pit formation is intensified uniformly between the Au strips at the front side of sample.

One would expect that the increased amount of holes at the front side should result in a faster etch rate beneath the Au strips. In such condition, however, the Si surface between the strips could as well be etched down. To ensure that the etch depth measurement is absolute, i.e. not relative to the etched-down Si surface, PR steps were created at both edges of the sample, as shown **Figure 4.12c**. Etching is now confined within the active region and the protected Si surface underneath the PR steps serves as a reference point for etch depth measurement. **Figures 4.12d** and **e** show the etch depth for sample without back contact at the active region and the reference point, giving a total etch depth of 660 nm. **Figures 4.12f** and **g** show the corresponding results for sample with back contact, which obviously gives a larger total etch depth of 970 nm. It is worthwhile to note that without a reference point, the etch depth measurement becomes relative to the etched-down Si surface between Au strips and could lead to misinterpretation (*cf.* **Figures 4.12d** and **f**).

4.6.2 Hole Fill-Up Effect

To eliminate the contribution of holes from the Au back contact, we have explored another etching configuration where only a few cc of the etchant were placed on the front side of sample to form a liquid droplet (diameter ~ 0.5 cm), as shown schematically in **Figure 4.13a**. The droplet was arranged to wet only the Au strip region and not the large Au pad. The etching result is shown in **Figure 4.13b**. It can be seen that the surface between the Au strips is

still uniformly populated with numerous pits. As has been explained in **Section 4.5.3**, the excess holes which are injected at the front side of sample may reach the back side and react with the etchant to form pits. This consumption pathway for the excess holes is not available when only the front side of sample is exposed to the etchant. As such, the excess holes will finally fill up the whole thickness of the sample and give rise to the formation of numerous pits between the Au strips.

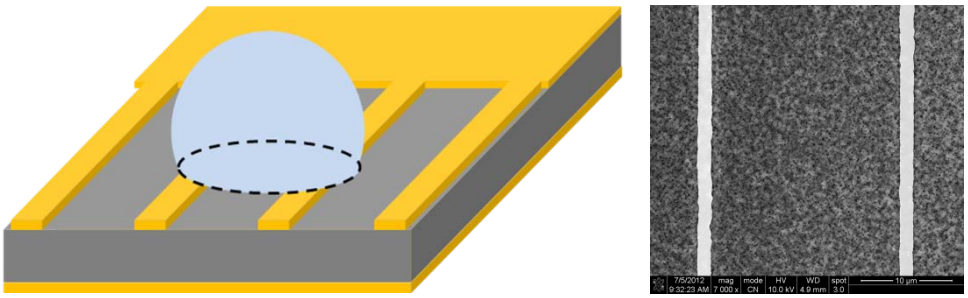

(a) (b)

Figure 4.13: (a) Schematic illustration of etching experiment with a droplet. The large Au pad was not exposed to the etchant droplet. (b) Top-view SEM image of sample etched with a droplet for 15 minutes. [H_2O_2] and [HF] were fixed at 1.21 and 1.73 M, respectively.

4.6.3 Electrochemistry Current vs. Semiconductor Current

We have tried to eliminate the hole fill-up effect by applying an electrical bias to the samples. The summary of our etching results for different biasing conditions is shown in **Table 4.1**. First, we observed that the etch rate is controlled by the current. Higher current gives higher etch rate, as can be seen by comparing samples 2 and 3 or samples 4, 5, and 6. It can be seen, however, that there is also an effect of bias polarity. Negative biasing (sample 2) results in higher etch rate than the opposite polarity (samples 4 and 5) despite smaller current. Second, under the condition employed in sample 3, we observed that the pits are localized near the edge of the strips, as shown in

Figure 4.14. It suggests that to obtain smooth surface morphology, the current should be small and at the same time, the voltage drop (and thus the electric field) across the sample should be sufficiently large. However, this requirement is generally difficult to be met. **Table 4.1** shows that for sample without any external bias (sample 1), the current as measured by the ammeter is only 0.4 mA, which is several orders of magnitude lower than the current generated even by a small bias. This means that the external current generated by the semiconductor far outweighs the electrochemistry current generated by MACE process alone. Under such condition, the hole injection becomes so abundant that it is difficult to achieve pit-free surface. Unfortunately, for this catalyst configuration, increasing the voltage (to obtain higher electric field to direct the holes) will concurrently increase the external current because both sides of sample are coated with an ohmic material (Au).

Table 4.1: Summary of etching results on Au finger samples with Au back contact for different biasing conditions. The voltage is relative to the front side of the sample. [H_2O_2] and [HF] were fixed at 1.21 and 1.73 M, respectively, and the etch duration was 15 minutes.

Sample No.	*I* (A)	*V* (V)	Etch depth (μm)	Surface morphology between Au strips
1	4×10^{-4}	0	0.39	Pits everywhere
2	0.15	-1	2.21	Pits everywhere
3	**0.09**	**-1**	**0.35**	**Pits localized near the edge**
4	0.25	+1	0.64	Pits everywhere
5	0.18	+1	0.5	Pits everywhere
6	0.03	+0.1	0.1	Pits everywhere

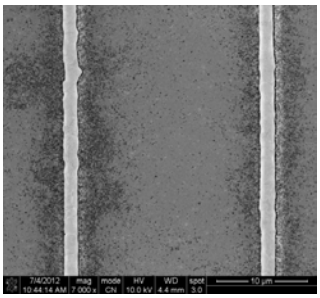

Figure 4.14: Surface morphology between Au strips for sample etched with I = 0.09 A and V = – 1 V (sample 3 in Table 4.1). [H_2O_2] and [HF] were fixed at 1.21 and 1.73 M, respectively, and the etch duration was 15 minutes.

4.7 Modes of Catalyst Instability

In this section, we propose two possible causes for catalyst instability during MACE, namely the overlap of excess holes between neighboring catalysts and the generation of H_2 bubbles. From these two modes of instability, we define a regime of etch chemistry and catalyst spacing for which catalyst stability and vertical etching can be achieved.

4.7.1 Mode 1: Overlap of Excess Holes

During etching, holes are constantly generated at the Au-Si interface from H_2O_2 reduction. Assuming the holes inside the Si diffuse isotropically and taking a two-dimensional (2D) slice normal to the axis and far from the end of the strip, the hole concentration, *C(x,y,t)*, inside the Si can be modeled as a 2-D constant-source diffusion process so that

$$\frac{C(x,y,t)}{C_0} = erfc\left(\frac{x}{2\sqrt{Dt}}\right) erfc\left(\frac{y}{2\sqrt{Dt}}\right)$$

Equation 4.4

where C_0 is the excess hole concentration at the Au-Si interface ($y = 0$), x and y represent the Cartesian coordinates defined by the schematic in **Figure 4.15a**, *erfc* is the complementary error function, D is the hole diffusivity estimated from experimental data, 2.94 x 10^{-15} m^2/sec (for details, see Appendix B) and t is the etch duration.

Since etching occurs only at the Au-Si interface, we are only interested in the hole concentration at $y = 0$. The time evolution of the hole concentration for samples with Au strip spacings of 20 and 2 μm are plotted using MATLAB[73] software in **Figures 4.15b** and **c**. For a strip spacing of 20 μm, the hole concentration at the Au-Si interface remains uniform over the whole

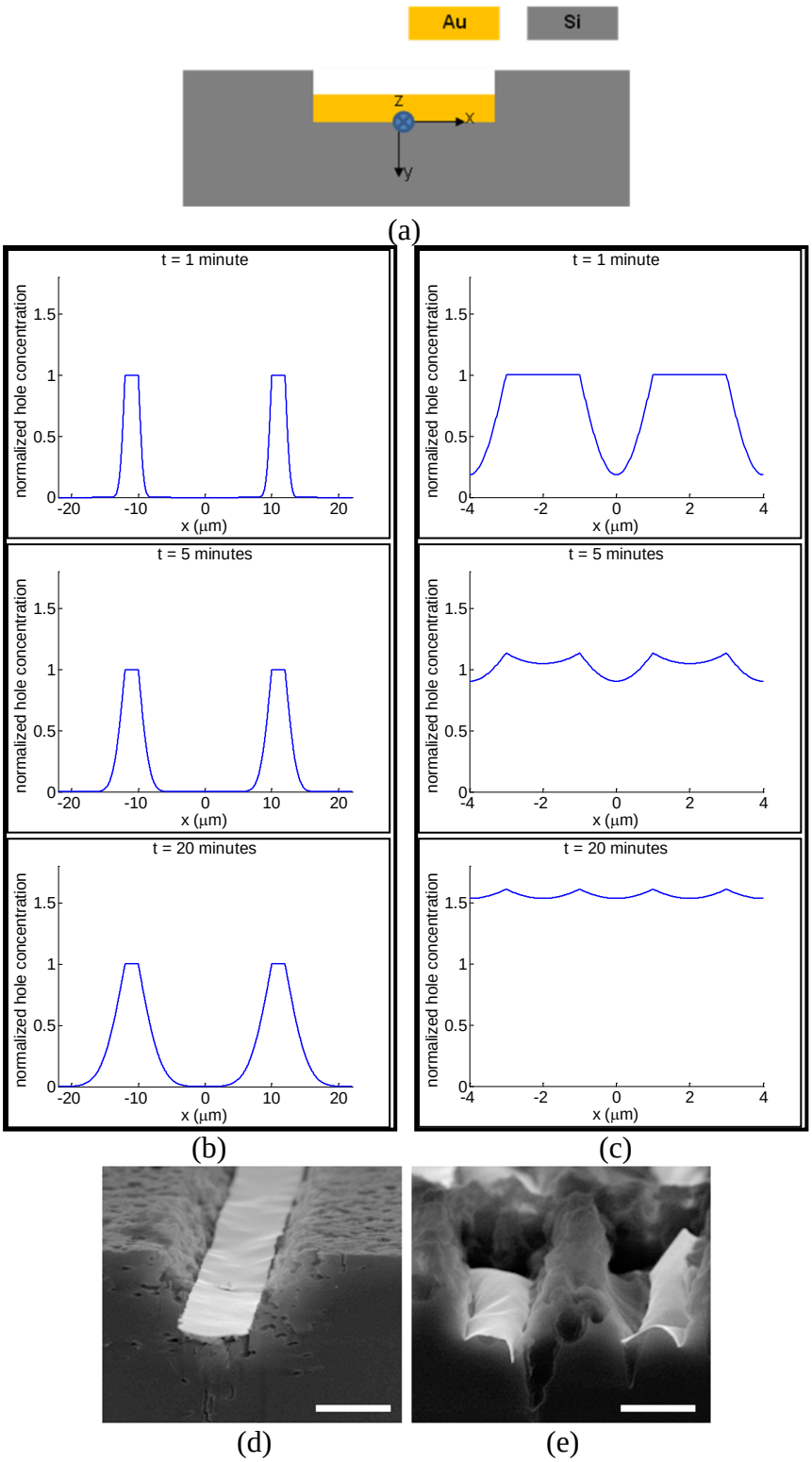

Figure 4.15: (a) Schematic diagram defining the coordinates for the calculated hole concentration. (b)-(c) Time evolution profiles of the hole concentration at Au-Si interface during etching for Au strips with spacings of 20 μm and 2 μm, respectively. (d)-(e) Cross-sectional SEM images of samples with Au strip spacings of 20 μm and 2 μm, respectively. [H_2O_2] and [HF] were fixed at 1.21 and 1.73 M, respectively, and the samples were etched for 20 minutes. The scale bar for the SEM images is 2 μm.

etching duration such that the Au strip should remain flat. For samples with a strip spacing of 2 μm, however, the hole concentration at the Au-Si interface becomes higher at the edges due to additive accumulation of excess holes from the neighboring Au strip. A higher etch rate at the edges should result in a concave Au strip morphology after etching. **Figures 4.15d** and **e** show SEM images for etched samples with strip spacings of 20 and 2 μm, and show consistency with the simulation results in that the Au strips with 20-μm spacing remain flat, and the sample with 2-μm spacing shows a concave pattern.

4.7.2 Mode 2: Generation of H_2 Bubbles

Another source of instability is the generation of H_2 bubbles during MACE, as illustrated schematically in **Figure 4.16a**. As the bubbles form beneath the Au, those near the edges can escape into the solution more easily than those near the center of the catalyst strip. As a consequence, the catalyst is in better contact with the Si near the strip's edges and the etch rate is higher there, so the shape of the Au-Si interface curves as shown in **Figure 4.16a**. According to **Equation 4.3**, it can be seen that H_2 bubbles will form when $n <$ 4. This corresponds to

$$[H_2O_2] < \frac{1}{3}[HF]$$

Equation 4.5

For [HF] = 1.73 M, this corresponds to $[H_2O_2] < 0.58$ M.

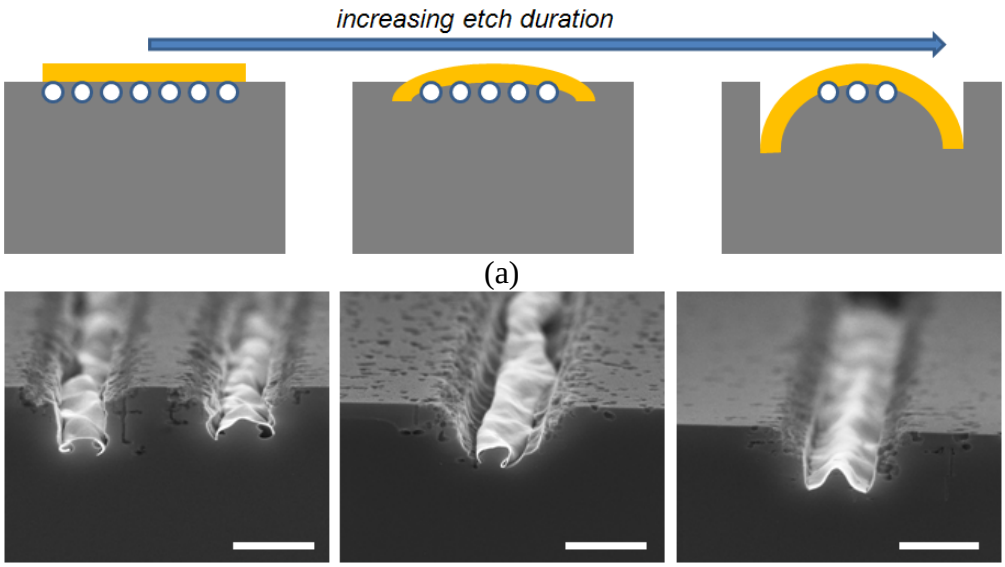

Figure 4.16: (a) Schematic illustrating the effect of trapped H_2 bubbles on the etching profile. (b)-(d) SEM cross-sectional views of the etching profile with $[H_2O_2]$ = 0.017 M, [HF] = 1.73M, for samples with Au strip spacings of 2, 5, and 20 μm, respectively. The scale bar for the SEM images is 2 μm.

Figures 4.16b to **d** show the etch morphologies with $[H_2O_2]$ = 0.017 M for samples with Au strip spacings of 2, 5, and 20 μm, respectively. At this concentration, H_2 bubble generation is significant so the Au strip is unstable for all samples irrespective of Au strip spacing.

4.7.3 Etch Stability Diagram

Figure 4.17 summarizes the stability conditions for the etching of Si as a function of the Au strip spacing and $[H_2O_2]$. Two modes of instability can be distinguished. Mode-1 instability is due to the pronounced overlap of excess holes from the neighboring Au strips that gives rise to a higher hole concentration at the edge of strip and thus results in a concave strip configuration. This effect is most prominent for samples with Au strip spacing of 2 μm in that there is no stable regime for all H_2O_2 concentrations used in

this work. For samples with a strip spacing of 5 μm, it is possible to achieve etching stability for $[H_2O_2]$ = 0.3 and 0.46 M. At higher H_2O_2 concentrations, the effect of excess holes dominates and no etch stability can be obtained. Mode-2 instability in **Figure 4.17** is caused by the generation of H_2 bubbles beneath the Au strips. In theory (see **Equation 4.5**), this should happen for $[H_2O_2] < 0.58$ M. We have, however, observed experimentally that stable etching could be achieved even for H_2O_2 concentrations as low as 0.3 M for samples with strip spacing≥ 5 μm. This suggests that when $[H_2O_2]$ is not too low (e.g. 0.3 M), the rate of H_2 bubble generation is sufficiently low that bubbles still escape into the solution and therefore do not cause an instability. A complete summary of our results with all the SEM images can be found in Appendix C.

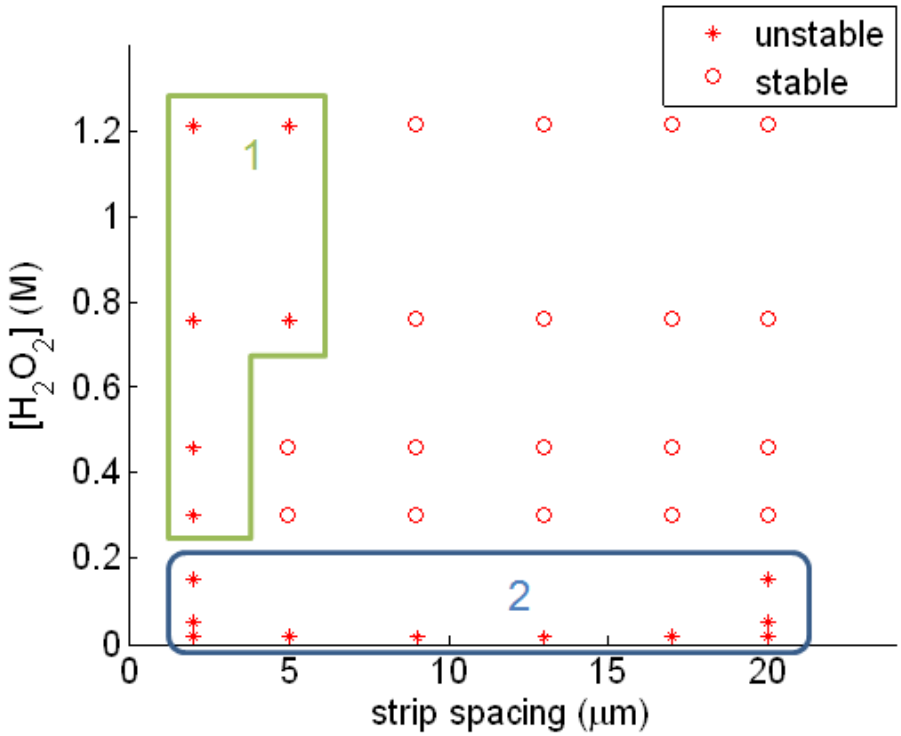

Figure 4.17: Stability diagram for MACE of Si as a function of the Au strip spacing and the concentration of H_2O_2.

Chapter 5. Fabrication of Silicon Nanostructures with Metal-Assisted Chemical Etching

5.1 Introduction

In Chapter 4, we have presented a systematic study on the mechanism and stability of isolated catalyst in MACE of Si. In this chapter, we investigate the etching characteristics with interconnected catalyst configuration patterned by interference lithography (IL). It has been established that etching of Si proceeds in uniform direction relative to the substrate orientation when the catalyst is interconnected.[20,23] This has been exploited to fabricate arrays of vertical Si nanowires,[19,20] nanofins,[19] or tilted nanowires.[20] We propose that the role of excess holes is more significant in IL-patterned catalyst configuration such that the etched nanostructures possess a relatively high degree of porosity. We demonstrate that the porosity of the nanostructures can be exploited to obtain an ordered array of Si nanocones,[21] which may find applications as a master copy for nanoimprinted polymer substrates in biomedical research, as a candidate for making sharp probes for scanning probe nanolithography, or as a building block for field-emitting-tip devices. The influence of doping type and concentration on the porosity of nanowires will be examined. We further demonstrate that the porosity of the nanostructures can be tuned from the etchant concentration. Other than the excess holes generated from the patterned Au catalyst, we also explore the role of extraneous Au nanoparticles (NPs) on the surface condition of the etched Si nanostructures, as detailed in Appendix F, and it will be shown that the effect of these NPs can be eliminated by employing an anti-reflection-coating (ARC)

layer in the interference lithography step.

5.2 Experimental Details

Figure 5.1 shows the process flow to obtain the Si nanowires or nanofins using a combination of interference lithography (IL) and MACE. The Si wafer was first coated with an Ultra-i 123 PR layer and baked at 90°C for 90 seconds. The PR was then exposed using a Lloyd's-mirror type IL setup with a HeCd laser source (λ = 325 nm), baked at 110°C for 90 seconds, and developed in Microposit MF CD-26 for ~ 1 minute to obtain periodic PR patterns on Si. Two exposures with angle of 90° between exposures result in PR dots, and two exposures with acute angle between exposures result in PR fins. After O_2 plasma step to clear any residual PR layer, the sample was coated with ~ 20-nm Au using thermal evaporation at a base pressure of ~ 10^{-6} Torr. The sample was then etched in a mixture of H_2O, HF, and H_2O_2 at room temperature with the [HF] and [H_2O_2] fixed at 4.6 and 0.46 M, respectively. Afterwards, the Au was removed using a standard iodine-based Au etchant and the PR was dissolved in acetone.

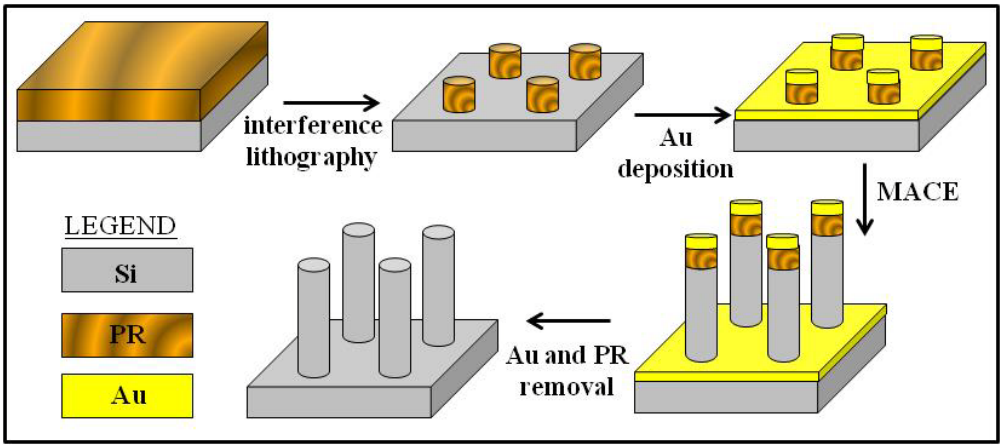

Figure 5.1: Schematic diagrams illustrating fabrication of Si nanowires or nanofins using a combination of interference lithography and MACE.

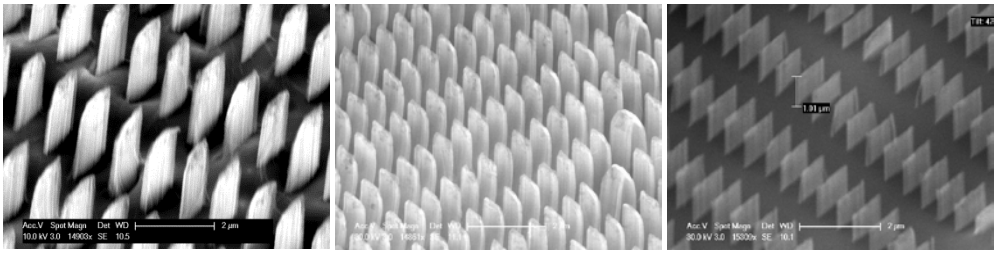

(a) (b) (c)

Figure 5.2: Si nanofins fabricated using interference lithography and MACE on (a) p-Si (100) 4-8 Ω.cm, (b) p-Si (110) 1-10 Ω.cm, and (c) p-Si (111) 1-10 Ω.cm.

Figures 5.2a, **b**, and **c** show Si nanofins fabricated on Si (100), (110), and (111) substrates, respectively. As can be seen, all the nanofins are oriented vertically irrespective of the substrate orientation. This is because in an interconnected configuration, the lateral movement of the catalyst is severely restricted such that inclined etching is not possible.

5.3 Dominant Role of Excess Holes in IL-Patterned Catalyst

In Section 4.4, we have shown that excess holes are responsible for the formation of pits at locations away from the catalyst. For large separation between catalysts, e.g. 20 μm, Regions A and B are clearly distinguishable. However, for small separation, e.g. 2 μm, Regions A and B become indistinguishable due to a significant overlap of regions with high excess hole concentrations.

IL-patterned catalyst is in perforated film configuration with sub-micron separation between perforations. Therefore, the excess holes for this catalyst configuration should contribute significantly to etching away from the catalyst and give rise to porous etched nanostructures, as illustrated in **Figure 5.3**. We found that this porous region on the etched Si nanostructures exhibit enhanced oxidation ability even at room temperature. We exploit this finding to

demonstrate the fabrication of Si nanocones from porous Si nanowires etched for a prolonged duration. We also investigate the influence of dopant on the nanocone formation. Si nanofins exhibit caterpillar-like or haystack-like clustering upon prolonged etching and the porous layer can extend through the thickness of the fins.

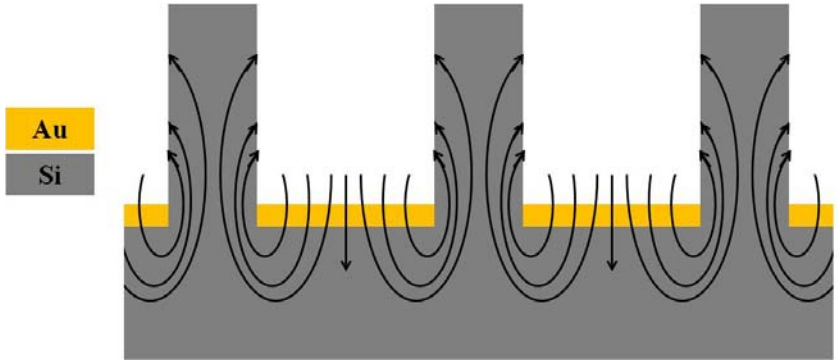

Figure 5.3: Schematic of hole injection into Si during MACE using IL-patterned catalyst.

5.3.1 Fabrication of Silicon Nanocones from Porous Silicon Nanowires

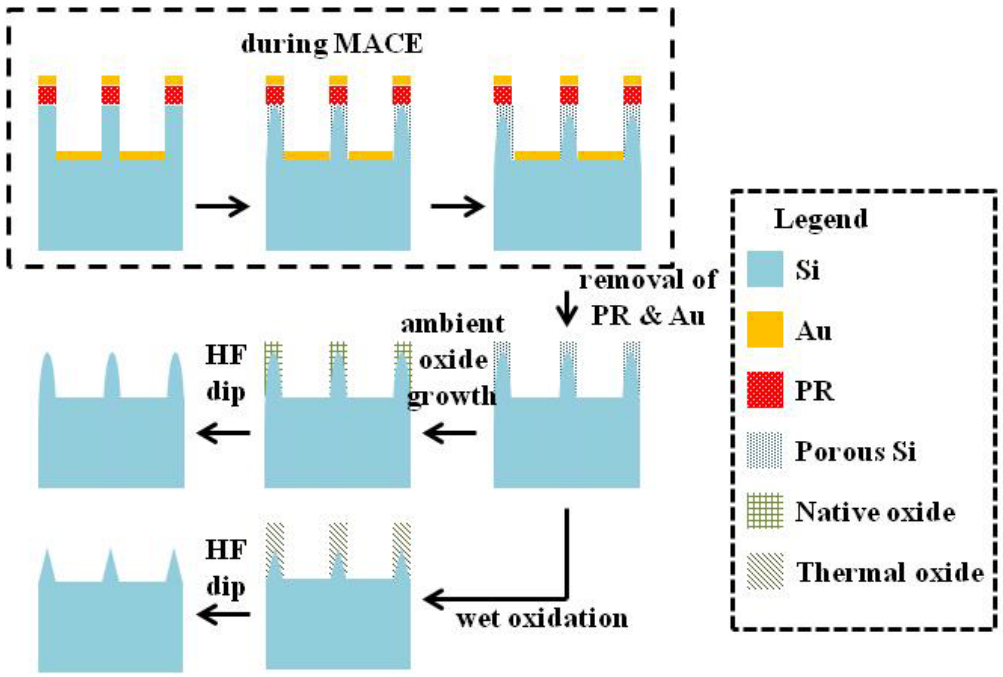

Figure 5.4: Schematic diagram illustrating the formation of porous Si nanowires during MACE and the subsequent process flow to obtain Si nanocones from nanowires. Note that the bending of nanowires is not illustrated in this schematic diagram.

Figure 5.4 illustrates that during MACE, porous Si will result at the surface of the nanowires. We suggest that during the formation of the Si nanowires, as the etching duration increases, the top part of the nanowire would be more porous compared to the lower part because the top part would have been exposed to the etchant for a longer period of time. A further oxidation in ambient or by wet oxidation of such nanowires followed by wet etching in 10% HF solution, resulted in a large area, precisely located and of well-controlled geometry and size, of nanocones on the Si surface.

Figure 5.5 shows the SEM images of Si nanowires that were etched with exactly the same etching conditions as described in **Section 5.2**, except with different etching durations that resulted in (a) straight (~1.70 μm), (c) top-bent (~1.80 μm), and (e) severely bent (~2.00 μm) nanowires. SEM images (b), (d), and (f) show the respective Si nanowires after being etched again in 10% HF for 1 minute. The results suggest that all the nanowires obtained from the IL-MACE method contained silicon oxide after exposure to atmospheric ambient. We assume here that the removal of Si oxide from the Si nanowires is complete while immersed in the mixed solution of H_2O, HF, and H_2O_2. Therefore, the oxide formed after the nanowires had been exposed to air must be due to a reaction from ambient oxygen to the porous Si at the surface of the nanowires. The porous Si will oxidize rapidly as the sponge-like structure[56] consists of a large number of pores resulting in a large surface area for rapid oxidation.[74] The non-uniform distribution of porous Si along the length of the nanowire and its subsequent oxidation in ambient conditions results in the residual nanocone.

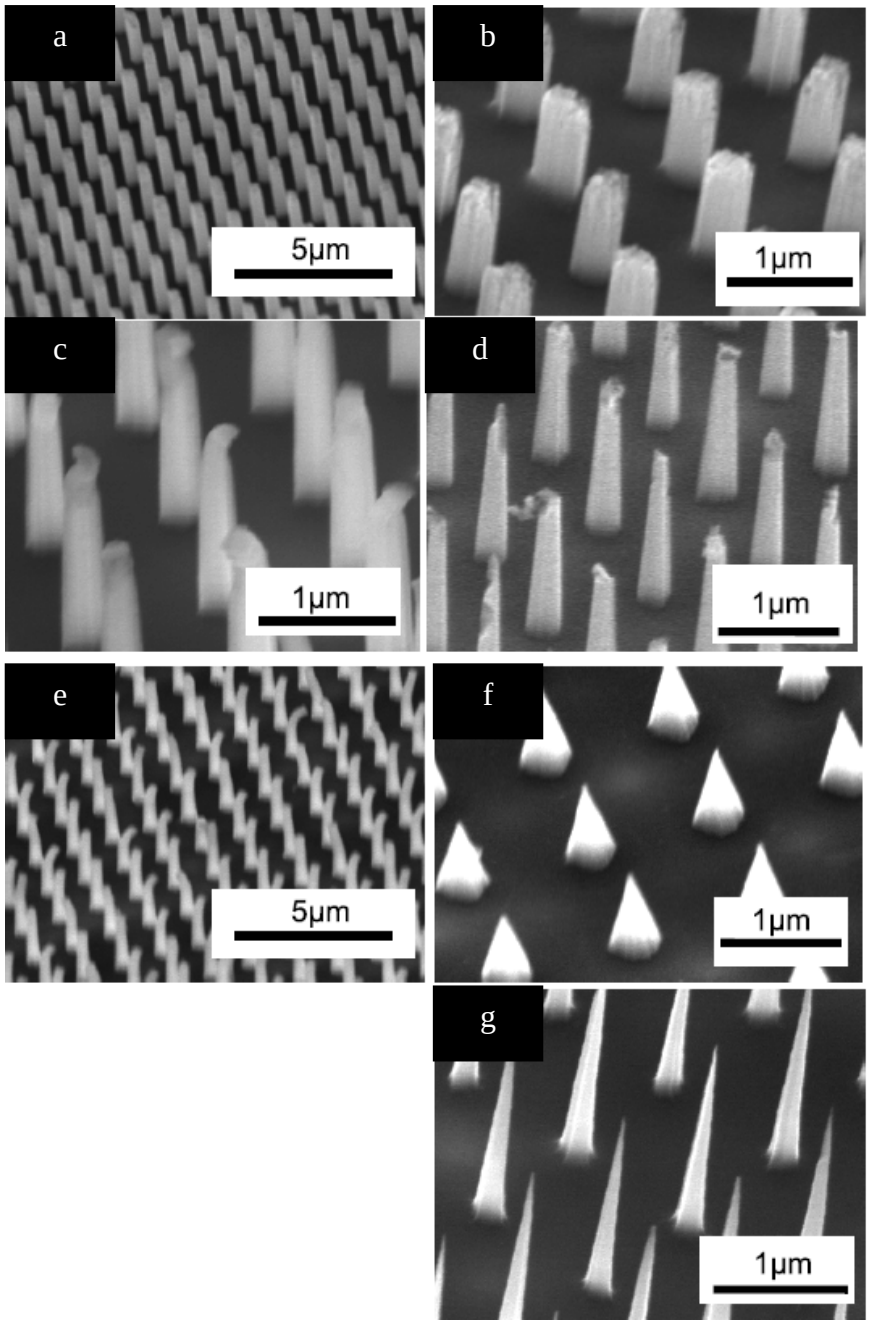

Figure 5.5: SEM images of large-area, precisely located (a) straight, (c) top-bent, and (e) severely bent Si nanowires that were etched in a mixed solution of H_2O, HF, and H_2O_2 at room temperature, respectively. SEM images (b), (d), and (f) show the different shapes of nanostructures after etching Si nanowires in 10% HF solution for 1 minute at room temperature. SEM image (g) shows Si nanocones produced by an additional wet thermal oxidation and HF etching of the top-bent nanowires in (c).[21]

The different degree of bending of nanowires may be linked to the different degree of porosity of these nanowires. **Table 5.1** summarizes the change in volume of the nanowires as a result of etching in 10% HF solution. The percentage change in volume was arrived at by dividing the change of nanowire volume (i.e. by subtracting the final volume from the initial volume) by the initial volume of the nanowires. The straight nanowires remained straight after etching in 10% HF (**Figure 5.5b**), and have a reduction of nanowire height from ~1.7 to 1.5 μm, giving rise to a 10% change in volume with the oxide removed. This implies that the straight nanowires have low degree of porosity. The top-bent and severely bent nanowires had a reduction of height from 1.80 to 1.4 μm, and 2.00 to 1.00 μm, respectively. This leads to a 74% and 86% volume reduction when the nanowires were etched in 10% HF solution. It means that these bent nanowires have much higher degree of porosity compared to the straight nanowires. The top-bent nanowires give rise to Si nanocones after the oxide at the silicon surface was removed. Note that a large number of these nanocones exhibit 'blunt' tips (**Figure 5.5d**). The removal of a significant amount of oxide from severely bent nanowires resulted in Si nanocones with sharp tips (**Figure 5.5f**). **Figure 5.5g** shows an SEM image of top-bent nanowires that have gone through a further wet thermal oxidation process at 900°C for 35 minutes and then etched in 10% HF solution. It can be seen from this figure that significantly sharper nanocones have been obtained by the extra wet thermal oxidation process. Therefore, we are able to vary the geometry of the Si nanocones by manipulating the amount of silicon oxide grown on the Si nanowire surface.

Table 5.1: The change in nanowire height and the estimated change in nanowire volume after the nanowires were etched in 10% HF solution for 1 minute at room temperature.[21]

Type of nanowires	Diameter (nm)	Initial height (μm)	Height after HF etch (μm)	Volume reduction (μm^3)	Change in volume (%)
Straight	400	1.70	1.50	2.51×10^{-2}	10
Top-bent	260	1.80	1.40	7.08×10^{-2}	74
Severely bent	490	2.00	1.00	3.1×10^{-1}	86

5.3.2 Influence of Dopant on Porosity of Silicon Nanowires

Hochbaum *et al.*[42] have recently examined the structure of single crystalline mesoporous Si nanowires obtained by etching p-type Si wafers in a solution consisting of $AgNO_3$ and HF. They have observed an increase in the surface roughness of the nanowires as the resistivity of three Si wafers changed from 10, 0.1 to 0.005 Ω.cm. As our results above were all obtained from n-type Si of resistivity 10 Ω.cm, we selected p-type Si wafers of resistivity of 10, 0.1 Ω.cm as well as n-type 0.1 Ω.cm Si to determine the influence of doping type and concentration for the creation of nanocones.

The experimental procedures were exactly the same as shown in **Figure 5.4** and the SEM images of the as-prepared nanowires and the nanocones (i.e. after oxidation and HF etch) are shown in **Figures 5.6a**, **c**, **e** and **b**, **d**, **f**, respectively. It should be noted that with a lower resistivity Si wafer, the as-prepared nanowires are of comparable height to those obtained from a Si wafer of 10 Ω.cm (by exploiting a shorter etch duration), but resulted in shorter nanocones when oxidized and etched in HF. This is in agreement with the results of Hochbaum *et al*. in that our lower resistivity wafer would have given rise to more porous Si nanowires and then resulted in shorter nanocones when oxidized and etched in HF. Our results also indicate that obtaining large-

area ordered nanocones using our method is independent of doping type. There are reports on the synthesis of Si nanocones using other methods. For example, Bae *et al.*[75] synthesized Si nanocones via the VLS method using Ga and Al catalysts. Hsu *et al.*[76] fabricated Si nanocones via self-assembly of silica nanoparticles followed by careful control of reactive ion etching (RIE). However, spatial control is difficult with VLS method and the need for dedicated RIE machine significantly increases the fabrication cost.

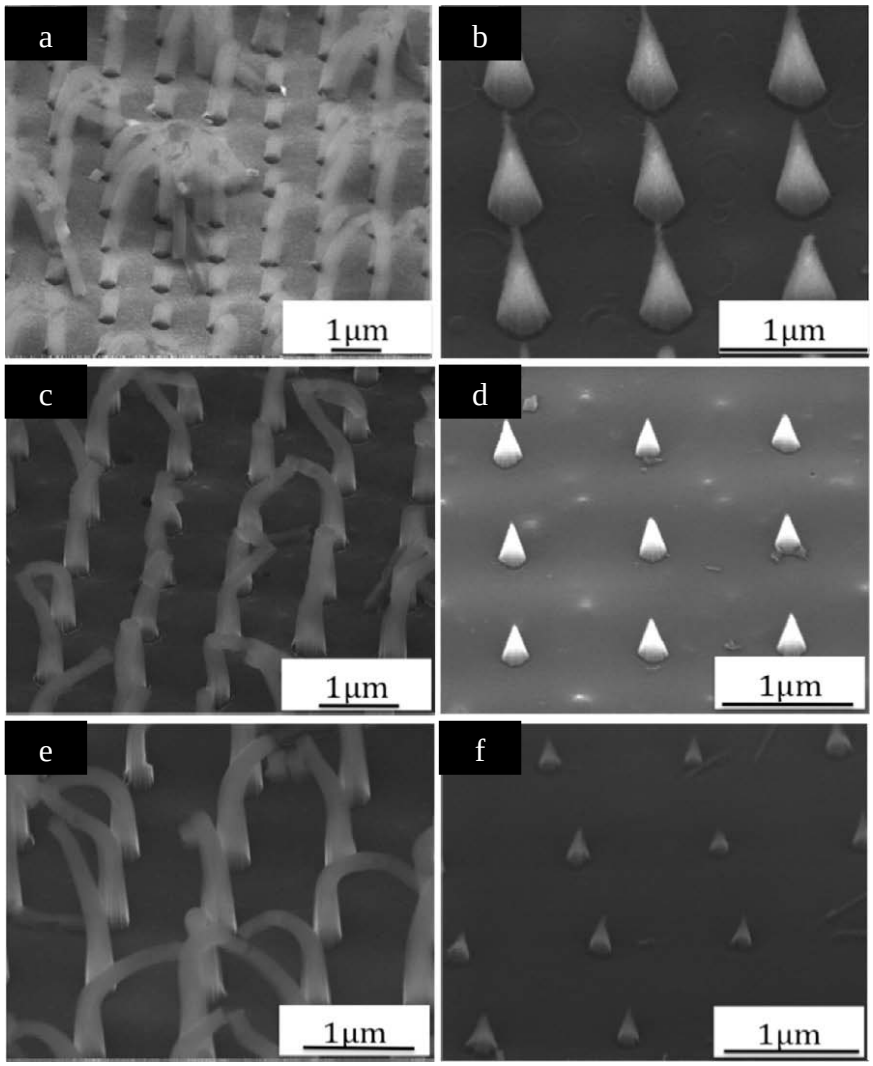

Figure 5.6: The SEM images of as-etched nanowires with (a) p-Si with resistivity 10 Ω.cm, (c) p-Si with a lower resistivity of 0.1 Ω.cm, and (e) n-Si with resistivity 0.1 Ω.cm. Etch durations were 10, 7, and 7 minutes for (a), (b), and (c), respectively. SEM images of the respective nanocones obtained by wet thermal oxidation and HF etch of the nanowires are shown in (b), (d), and (f) respectively.[21]

5.3.3 Caterpillar-like and Haystack-like Silicon Nanofins

We have also explored the porosity on Si nanofins fabricated using IL-MACE method and the results are shown in **Figure 5.7**. As can be seen, when etched for a long duration, the high-aspect-ratio nanofins cluster to the neighbors. The clustering is caused by capillary force between the fins on the liquid-air interface during drying process,[77,78] and could actually be avoided if critical point drying technique is used.[45] Interestingly, however, we found that the way the fins cluster is correlated to the crystallographic orientation of the Si substrate. When p-Si (100) sample is used, the fins cluster in a caterpillar-like fashion, as shown in **Figure 5.7a**. For p-Si (110) and (111) samples, the fins cluster in a haystack-like fashion, as shown in **Figures 5.7b** and **c**. The different clustering behavior might be related to the anisotropy in the elastic modulus of Si.[64]

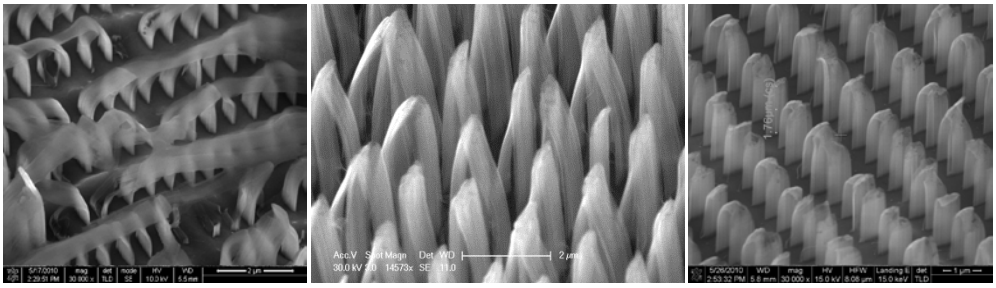

(a) (b) (c)

Figure 5.7: Clustered Si nanofins fabricated using interference lithography and MACE on (a) p-Si (100) 4-8 Ω.cm, (b) p-Si (110) 1-10 Ω.cm, and (c) p-Si (111) 1-10 Ω.cm. Etch duration was 14 minutes for all samples. (a) shows caterpillar-like nanofins while (b) and (c) show haystack-like nanofins.

We have demonstrated earlier that during the etching of Si nanowires, porous Si forms on the surface of the nanowires. This porous Si is oxidized readily when exposed to air so as to result in the formation of nanocones when etched in HF. We have tried similar experiments on the Si nanofins, as shown

in **Figure 5.8**. However, when the straight Si nanofins (**Figure 5.8a**) was immersed in 10% HF for 1 minute, only short Si stumps were left as shown in **Figure 5.8b**. This is expected because for fin geometry, the width is much smaller in one direction than the other such that the porous Si layer could extend through the whole thickness of the fin. Thus, when exposed to oxygen-containing atmosphere, the body of the fins will almost be completely oxidized and etched away when immersed in HF solution.

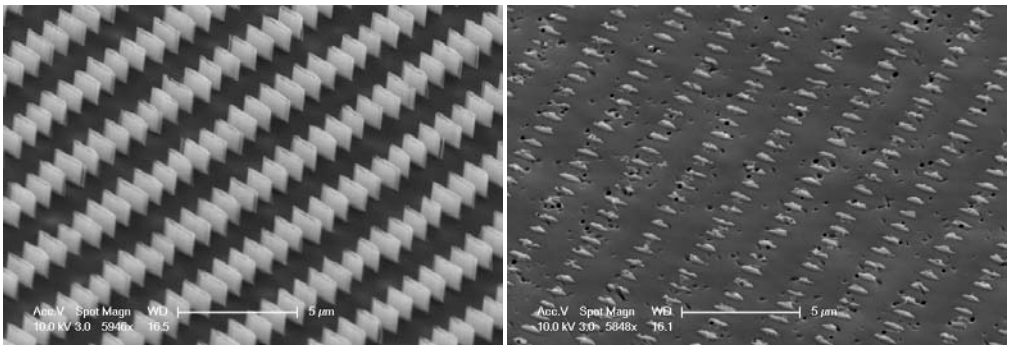

(a) (b)

Figure 5.8: (a) Straight Si nanofins fabricated using interference lithography and MACE. (b) The same Si nanofins after immersion in 10% HF for 1 minute.

5.4 Control of Excess Holes via Etchant Concentration

We have established in **Section 5.3** that substantial number of excess holes is responsible for the porous etched nanostructures. Since the flux and consumption of holes are controlled by $[H_2O_2]$ and [HF], respectively, we explore their influence on the porosity of the etched nanostructures.

5.4.1 Influence of $[H_2O_2]$

Figures 5.9a, **b**, and **c** show Si nanowires etched with H_2O_2 concentrations of 0.46, 0.2, and 0.08 M, respectively. As can be seen, the nanowires become less porous or less tapered with decreasing $[H_2O_2]$. Since

$[H_2O_2]$ controls the flux of holes injected into the Si, decreasing $[H_2O_2]$ would produce fewer excess holes which can diffuse away from the catalyst to porosify the body of the nanowires. It should be noted, however, that reducing the $[H_2O_2]$ from 0.46 to 0.08 M (~ 6:1 dilution) is still insufficient to eliminate the tapering or etching of the nanowire body. This is probably because the HF molecules proceed to react with the holes from the catalyst edges while the holes are uniformly injected across the catalyst. As a result, when [HF] is low (e.g. 1.73 M), some holes can still escape from the catalyst to etch the body. Another consequence of reducing $[H_2O_2]$ is that fewer holes are available for etching underneath the catalyst, i.e. the etch rate should decrease with decreasing $[H_2O_2]$. Indeed, the etch rate was found to decrease from 250 nm/min to 100 nm/min to 60 nm/min.

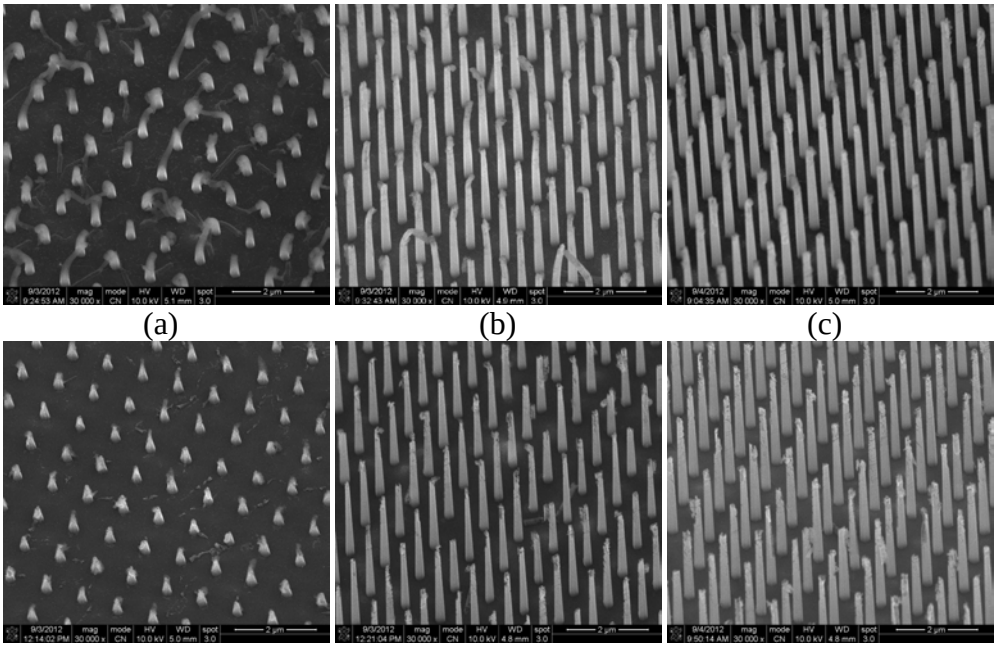

(a) (b) (c)

(d) (e) (f)

Figure 5.9: Si nanowires etched with: (a) $[H_2O_2]$ = 0.46 M for 10 minutes, (b) $[H_2O_2]$ = 0.2 M for 30 minutes, and (c) $[H_2O_2]$ = 0.08 M for 60 minutes. [HF] was fixed at 1.73 M. (d)-(f) are SEM images of the nanowires shown in (a)-(c), after aged for ~ 1 day in atmospheric condition and etched in 10% HF for 1 minute.

Figures 5.9d, **e**, and **f** show the same set of nanowires which have been left in atmospheric condition for ~ 1 day and subsequently etched in 10% HF for 1 minute. For $[H_2O_2]$ = 0.46 M, the nanowires were transformed to nanocones after etched in HF (compare **Figures 5.9a** and **d**). As explained in **Section 5.3.1**, severely bent nanowires exhibit enhanced oxidation ability such that the bent portion becomes fully oxidized after exposure to atmospheric ambient. Nanowires etched with lower $[H_2O_2]$ have a lesser degree of porosity and thus, undergo less volume subtraction after the HF etch step (compare **Figures 5.9b** and **e** or **Figures 5.9c** and **f**).

Similar conclusions were obtained from the same set of experiments carried out on Si nanofin samples and the results are summarized in Appendix D.

5.4.2 Influence of [HF]

Figures 5.10a, **b**, and **c** show Si nanowires etched with HF concentrations of 1.73, 4.6, and 8.63 M, respectively. As can be seen, the high porosity and tapering of the sidewall have been eliminated when [HF] is increased from 1.73 to 4.6 M (~ threefold increase). When HF supply is increased, more holes are consumed beneath the catalyst and fewer holes can diffuse away to etch the nanowire body. It is therefore expected that the etch rate of Si should increase and the porosity of the wires should be much reduced with an increase in [HF]. The etch rates were found to be 250, 900, and 750 nm/min for [HF] = 1.73, 4.6, and 8.63 M, respectively. When [HF] is too high, e.g. 8.63 M, etch rate may decrease due to increased evolution of H_2 bubbles.[29] **Figures 5.10d**, **e**, and **f** show the same set of nanowires which have

been left in atmospheric condition for ~ 1 day and subsequently etched in 10% HF for 1 minute. For [HF] = 1.73 M, the nanowires were transformed to nanocones after etched in HF (compare **Figures 5.10a** and **d**) for the reason explained in **Section 5.4.1**. For the wires etched with higher [HF], the wires are relatively non-porous such that there is no observable decrease in volume after the HF etch step (compare **Figures 5.10b** and **e** or **Figures 5.10c** and **f**). Similar conclusions were obtained from the same set of experiments carried out on Si nanofin samples and the results are summarized in Appendix E.

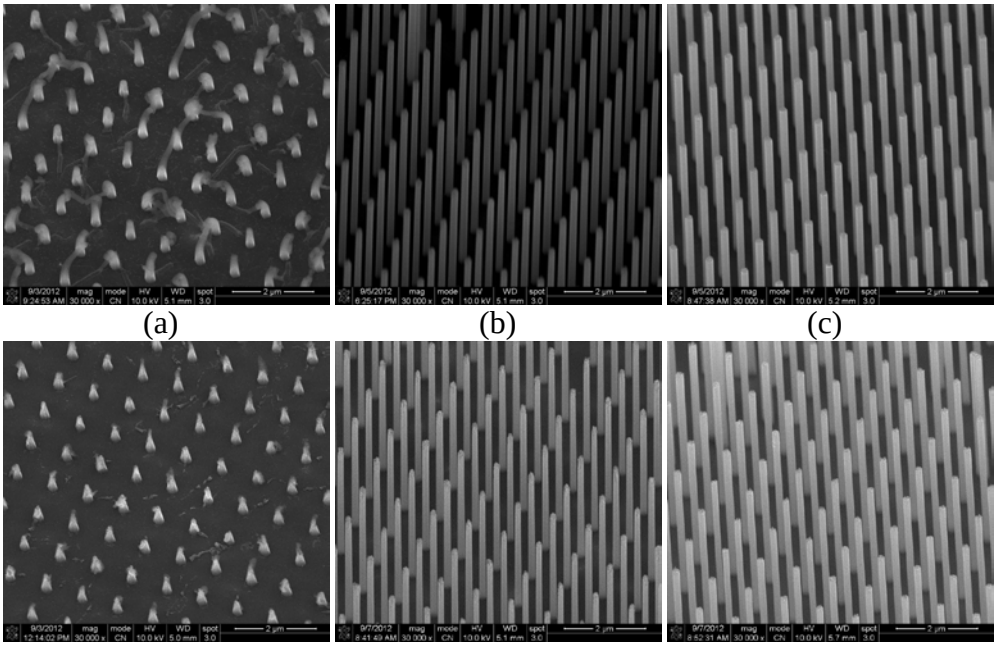

(a) (b) (c)

(d) (e) (f)

Figure 5.10: Si nanowires etched with: (a) [HF] = 1.73 M for 10 minutes, (b) [HF] = 4.6 M for 5 minutes, and (c) [HF] = 8.63 M for 7 minutes. [H_2O_2] was fixed at 0.46 M. (d)-(f) are SEM images of the nanowires shown in (a)-(c), after aged for ~ 1 day in atmospheric condition and etched in 10% HF for 1 minute.

Chapter 6. Bias-and-Metal-Assisted Chemical Etching of Silicon

6.1 Introduction

Electronic holes in Si are crucial in determining the etching characteristics of MACE. Li and Bohn[18] reported that the etch rate of Si depends on the rate of generation of holes, which is determined by the type of noble metal catalyst. It was found that Pt and Pd have stronger catalytic roles than Au. Chartier *et al.*[29] discovered that the etched Si surface morphology using Ag nanoparticles depends on the hole current density (estimated from mass loss measurement), which is determined from the etchant composition. At relatively low H_2O_2 concentration, the holes are consumed very close to the catalyst such that cylindrical pores are formed with sizes matching the diameters of the nanoparticles. At higher H_2O_2 concentrations, the hole current is spread over the entire Si surface and etching occurs everywhere, independent of the metal nanoparticle location (electropolishing). Hadjersi[31] reported that whether or not electropolishing occurs also depends on the type of oxidant. Lee *et al.*[72] suggested that hole current density, and thus the etch rate, can be regulated by adding salts into the etching solution. In Chapter 4, we have reported that pit formation between catalysts and catalyst stability during etching are governed by the excess hole concentration, which can be controlled from the etchant chemistries and catalyst spacings. In all these instances, however, the holes are controlled only in terms of their current density and not in their flow direction.

We have also shown in Chapter 4 that an electric field can be used to direct the excess holes to the back of the Si wafer and thus reduce the pit formation between catalysts. Therefore, in this chapter, we present results from an attempt to use an electric field to control the etching process. We call this etching method as bias- and metal-assisted chemical etching (BiMACE) of Si. Essential features of BiMACE are presented and comparisons are made between MACE and BiMACE. Quantitative analysis of the hole contribution to BiMACE without and with H_2O_2 is presented. The etching mechanism of BiMACE is discussed. Application of BiMACE to fabricate Si nanowires is also demonstrated and its possible extension to other semiconductor materials is suggested.

6.2 Experimental Details

Single-side polished p-type Si (100) wafers with resistivity 4-8 Ω.cm were used for the etching experiments. The wafers were cleaned in RCA-1 and RCA-2 solutions and dipped briefly in 10 wt.% HF before lithographic steps.

The process flow for the sample preparation is shown in **Figure 6.1a**. First, a WiDE-8C wet-developable anti-reflection coating (ARC) layer of ~ 80 nm thickness was spin coated on the Si wafer and baked at 100°C for 30 seconds and then at 172°C for 1 minute. Next, an Ultra-i 123 photoresist layer of ~ 400 nm was spin coated on top of the ARC layer and baked at 110°C for 1.5 minutes. The resist stack was then exposed using a UV mask aligner (SUSS MicroTec MJB4), baked at 110°C for 1.5 minutes, and developed in Microposit MF CD-26 developer for ~ 1.5 minutes to generate finger patterns

in the photoresist and simultaneously create an undercut profile in the underlying ARC layer, which is essential for successful lift-off process. Afterwards, oxygen plasma etch was carried out at a pressure of 0.2 Torr and power of 200 W for a duration of 20 seconds to remove any residual ARC layer after development. An Au layer (~ 60 nm) was then deposited on the resist patterns using a thermal evaporator (Edwards Auto306 FL400) at a base pressure of ~ 10^{-6} Torr. The samples were subsequently sonicated in a mixture of Microposit MF CD-26 developer and acetone (3:1 volume ratio) to lift off the resist patterns, leaving behind Au finger patterns on Si as shown in the scanning electron micrograph (SEM) image in **Figure 6.1b**.

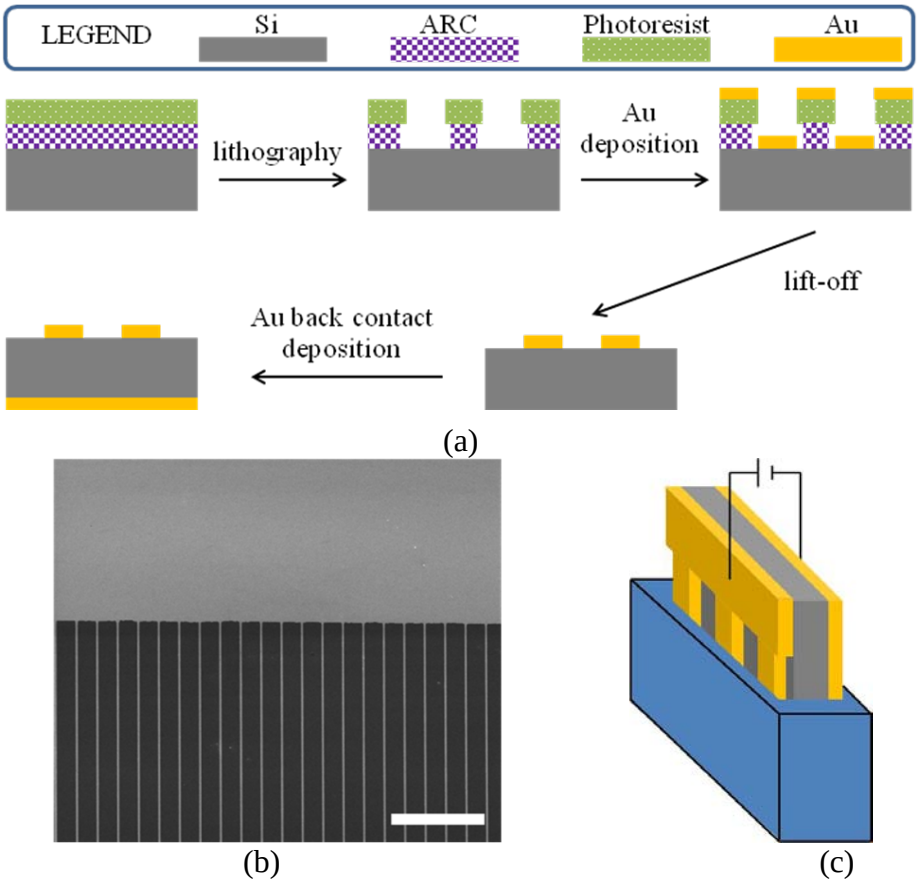

Figure 6.1: (a) Process steps for fabrication of Au fingers for BiMACE experiments. (b) SEM image of Au fingers with a spacing of 20 μm. The scale bar for the SEM image is 100 μm. (c) Schematic diagram illustrating the setup for BiMACE experiment.

A voltage bias was applied on the samples using a DC power supply (GW Instek GPR-11H30D) by connecting the positive terminal to the base of the Au fingers and the negative terminal to the back contact, as shown schematically in **Figure 6.1c**. The samples with the Au fingers portion were etched in HF solution of different concentrations *without* H_2O_2 at room temperature. The surface morphology of the samples was examined using a scanning electron microscope (FEI Nova NanoSEM 230).

6.3 Etching Results from BiMACE

It has been well accepted that the MACE process involves a pair of redox reactions at the cathode (Au-liquid interface) and anode (Au-Si) interfaces,[18,29]

Cathode: $\frac{n}{2}H_2O_2 + nH^+ \rightarrow nH_2O + nh^+$ **Equation 6.1**

Anode: $Si + 6HF + nh^+ \rightarrow H_2SiF_6 + nH^+ + \left(\frac{4-n}{2}\right)H_2$ **Equation 6.2**

Etching of Si by HF at the anode is made possible through the injection of holes (h^+) from the reduction of H_2O_2 at the cathode. The etching reaction produces soluble H_2SiF_6, H^+ ions, and hydrogen gas (H_2).

In the BiMACE process, the anodic reaction as given in **Equation 6.2** still holds, but the holes are now provided from the Si itself, which is, in principle, similar to the electrochemical etching of Si in HF.[48] However, in the electrochemical etching of Si, the hole current is spread over the entire Si surface exposed to the solution, which means that the pores are formed on random sites. Even though it is possible to pre-pattern defect sites on the Si

prior to etching to facilitate the formation of various arrays of Si microstructures, there exists a maximum dimension (interdefect spacing) above which it is not possible to avoid the formation of random pores between the defects.[57] **Figure 6.2** shows typical etching result using BiMACE. As can be seen, unlike the electrochemical etching method, etching is localized in the vicinity of the catalyst.

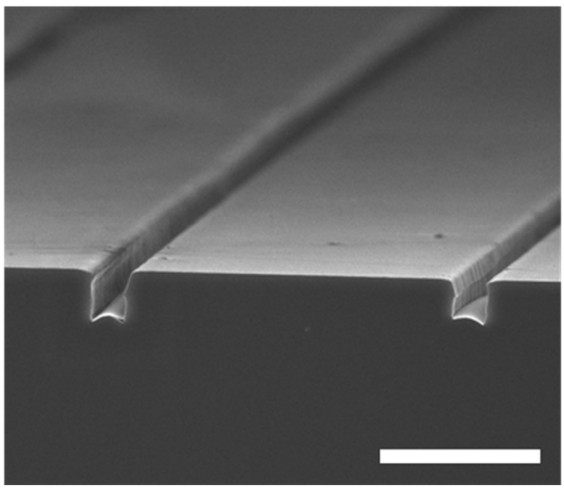

Figure 6.2: Cross-sectional SEM image of 20-μm-apart Au fingers etched with [HF] = 1.73 M and U = 2 V for 30 minutes. The scale bar for the SEM image is 10 μm.

Figure 6.3a shows the etch rate of Si as a function of voltage using BiMACE for a fixed [HF] of 1.73 M. As can be seen, the etch rate increases as the voltage is increased from 1 to 2 V. This is expected because an increase in voltage will drive a larger hole current in the Si, which is necessary for the etching of Si in HF. In MACE, the hole current is provided from the reduction of H_2O_2 and therefore, for a fixed [HF], the etch rate was found to increase with [H_2O_2], as has been shown in Chapter 4. **Figures 6.3b** to **d** show the cross-sectional view of samples etched with BiMACE for U = 1, 1.5, and 2 V, respectively, which are used to construct **Figure 6.3a**.

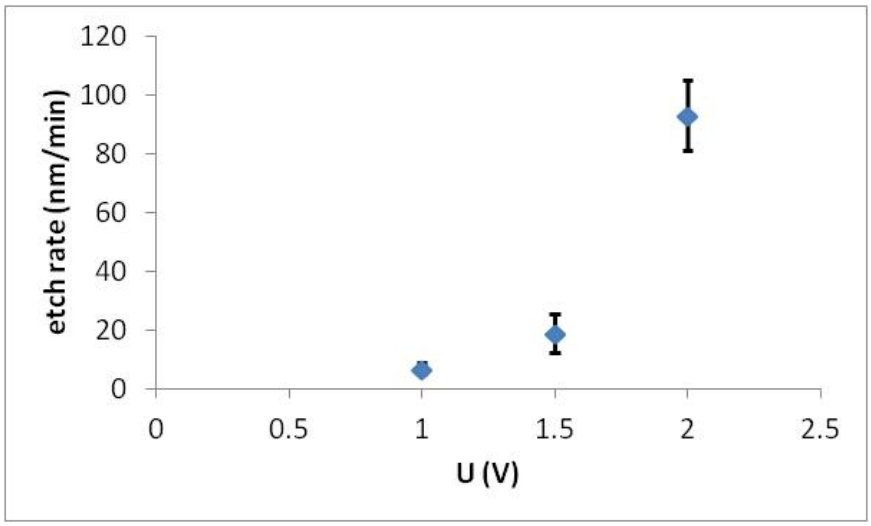

(a)

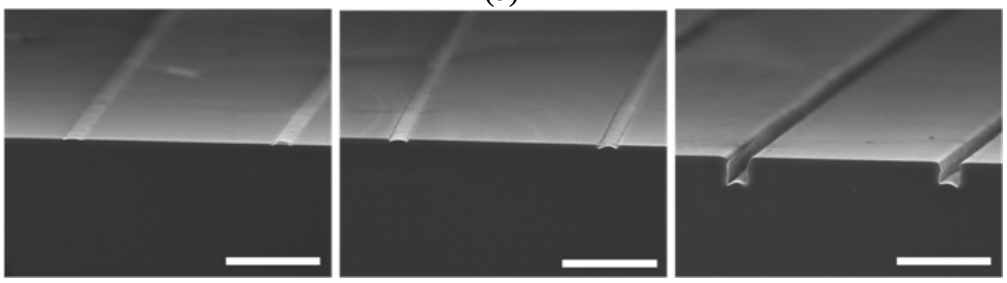

(b) (c) (d)

Figure 6.3: (a) Si etch rate versus voltage for 20-μm-apart Au fingers using BiMACE. (b)-(d) are cross-sectional SEM images of 20-μm-apart Au fingers etched with U = 1, 1.5, and 2 V, respectively. [HF] = 1.73 M and etch duration = 30 minutes. The scale bar for the SEM images is 10 μm.

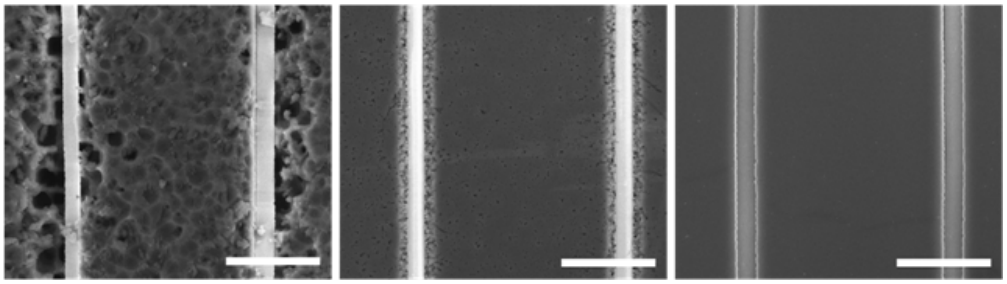

(a) (b) (c)

Figure 6.4: (a)-(b) Top-view SEM images of 20-μm-apart Au fingers etched using MACE with H_2O_2 concentrations of 1.21 M for 30 minutes (etch depth ~ 3 μm) and 0.017 M for 4 hours (etch depth ~ 1 μm), respectively. (c) Top-view SEM image of 20-μm-apart Au fingers etched using BiMACE with U = 2 V for 30 minutes (etch depth ~ 3 μm). [HF] is fixed at 1.73 M for all the samples. Scale bar for the SEM images is 10 μm.

Figures 6.4a and **b** show 20-μm-apart Au fingers etched using MACE with H_2O_2 concentrations of 1.21 M (30 minutes, etch depth ~ 3 μm) and 0.017 M (4 hours, etch depth ~ 1 μm), respectively, for a fixed HF

concentration of 1.73 M. It can be seen that for high [H_2O_2] (**Figure 6.4a**), the surface between the fingers became very pitted after etching. We have attributed in Chapter 4 that this pit formation is caused by the diffusion of excess holes away from the catalyst due to the fact that HF can only access the Si underneath the catalyst from the catalyst edges. Even as the flux of holes is significantly lowered ([H_2O_2] = 0.017 M) such that the etch depth is only ~ 1 μm for an etching duration of 4 hours, the pit formation between the Au fingers could not be entirely prevented, as shown in **Figure 6.4b**. In contrast, 20-μm-apart Au fingers etched using BiMACE with U = 2 V for 30 minutes (comparable etch depth to the sample in **Figure 6.4a**) exhibited pit-free Si surface between the fingers, as shown in **Figure 6.4c**. Therefore, BiMACE offers better control of the excess holes responsible for pit formation, as compared to MACE.

Figures 6.5a and **b** show 2-μm-apart Au fingers etched using MACE with H_2O_2 concentrations of 1.21 M (30 minutes, etch depth is indeterminate due to prominent damage on the Si surface) and 0.017 M (4 hours, etch depth ~ 1.5 μm), respectively, for a fixed HF concentration of 1.73 M. It can be seen that for high [H_2O_2] (**Figure 6.5a**), apart from the prominent damage on the Si surface between the fingers, the fingers exhibit etch instability. We have shown in Chapter 4 that etch instability for closely spaced catalysts is a consequence of additive accumulation of excess holes from the catalyst neighbors, which gives rise to non-uniform etch rate underneath each individual finger. When the flux of holes is significantly lowered by lowering [H_2O_2] to 0.017 M, etching became more stable but the surface between the fingers remained pitted (**Figure 6.5b**). In contrast, 2-μm-apart Au fingers

etched using BiMACE for 30 minutes with U = 1.5 V (etch depth ~ 1.5 μm) exhibits etch stability while maintaining pit-free surface, as shown in **Figure 6.5c**.

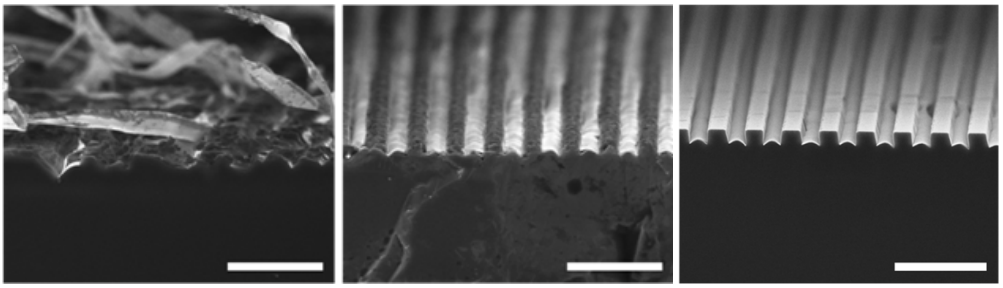

(a) (b) (c)

Figure 6.5: (a)-(b) Cross-sectional SEM images of 2-μm-apart Au fingers etched using MACE with H_2O_2 concentrations of 1.21 M for 30 minutes and 0.017 M for 4 hours, respectively. (c) Cross-sectional SEM images of 20-μm-apart Au fingers etched using BiMACE for 30 minutes with U = 1.5 V. [HF] is fixed at 1.73 M for all the samples. Scale bar for the SEM images is 10 μm.

To investigate the role of source of holes in the etching of Si, we performed experiments to isolate the contribution from "pure" BiMACE and "pure" MACE by including H_2O_2 component in the BiMACE setup. It should be noted, however, that when H_2O_2 is included, the Au back contact peels off easily during etching. Therefore, Au fingers are now patterned on both sides of the sample by using double-side polished wafer (p-type Si (100) with resistivity 1-10 Ω.cm).

Figure 6.6a shows the etch rate of Si for different voltage biases with and without H_2O_2. It can be seen that the etch rate of Si increases as long as the supply of holes is increased, either by using higher voltage or higher H_2O_2 concentration. This means that the etching of Si in HF is possible as long as there exists a flux of holes, regardless of the source. The difference in etch rate between samples without and with H_2O_2 for the same voltage allows us to calculate the contribution of holes from the Si itself and from H_2O_2,

$$\frac{dN_{holes\ from\ Si}}{dt} = v_{without\ H2O2} \times A \times N_{Si}$$

Equation 6.3

$$\frac{dN_{holes\ from\ H2O2}}{dt} = (v_{with\ H2O2} - v_{without\ H2O2}) \times A \times N_{Si}$$

Equation 6.4

where *dN/dt* is the number of reacting holes per unit time, *v* is the etch rate, *A* is the area of the Au strip (width of 2 μm and length of 0.5 cm), and N_{Si} is the atomic density of Si (5 x 10^{22} cm^{-3}). The plot of this calculation is shown in **Figure 6.6b**. As can be seen, the hole contribution from H_2O_2 is weakly dependent on the bias while the hole contribution from Si is strongly bias-dependent. The weak dependence of H_2O_2 hole contribution on the bias is expected because the holes are generated from H_2O_2 reduction events on the Au surface and thus, the biasing conditions should have little effect. On the other hand, the hole contribution from Si is determined from the total amount of current flowing through the Si and thus, the strong bias dependence is not surprising.

To check if the calculated amount of reacting holes is reasonable, the measured current during etching is also plotted in **Figure 6.6c**. By subtracting the total current without H_2O_2 from the current with H_2O_2, we can obtain the current contribution from the Si itself and from H_2O_2 separately, as shown in **Figure 6.6d**. It can be seen that the current contribution from the Si is much higher than that of the H_2O_2. However, as shown previously in **Figure 6.6b**, a significant portion of the total number of reacting holes during etching is derived from H_2O_2. This suggests that H_2O_2 is more efficient than the voltage bias in facilitating the holes to participate in the etching reaction. In other words, the hole current generated by the bias is mostly dissipated into the bulk

of Si, while the hole current generated by H_2O_2 reduction events contribute significantly to the surface reaction, i.e. etching of Si. It should be noted that the negative calculated value of flowing holes on **Figure 6.6d** could be caused by the non-uniform sample sizes, the effect of which becomes significant as the current contribution from H_2O_2 is small.

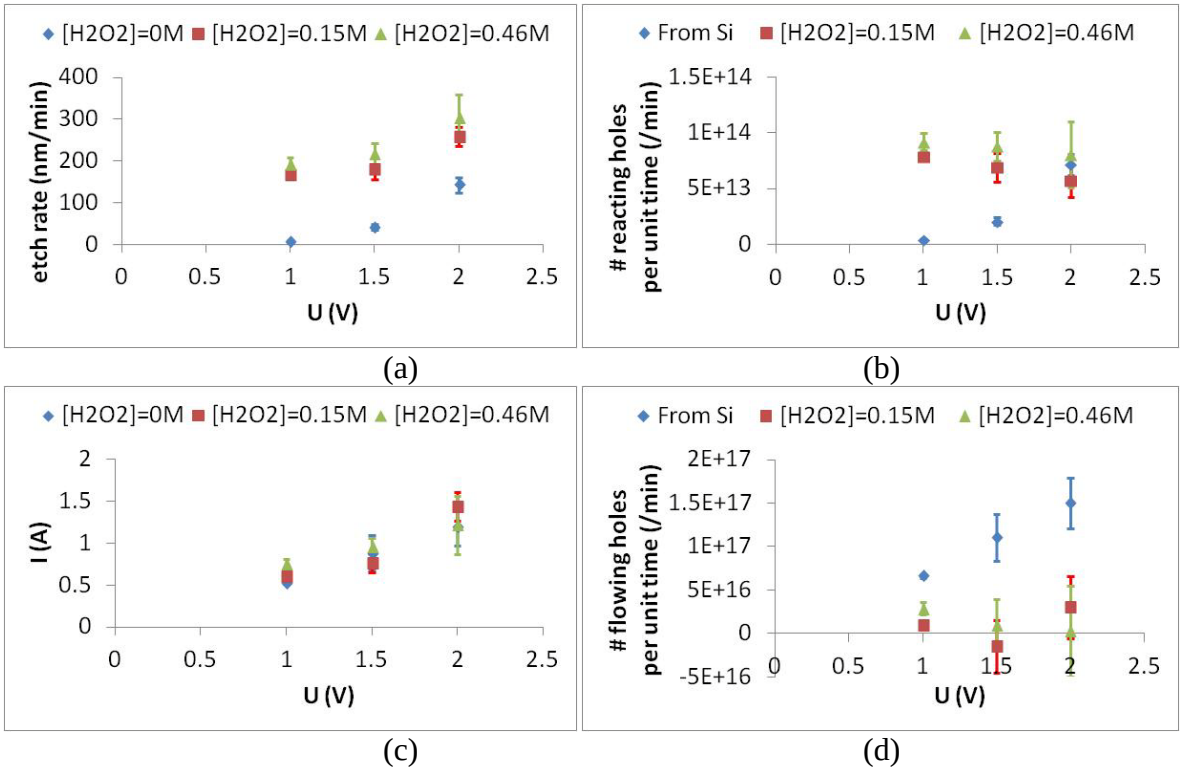

Figure 6.6: (a) Si etch rate versus voltage for 20-µm-apart Au fingers using BiMACE with and without H_2O_2. (b) Number of reacting holes per unit time versus voltage for 20-µm-apart Au fingers using BiMACE with and without H_2O_2. (c) Current versus voltage for 20-µm-apart Au fingers using BiMACE with and without H_2O_2.

6.4 Etching Mechanism

BiMACE is a polarity-dependent etching method in that etching only occurs on the positive terminal. **Figures 6.7a** to **c** show that no etching occurred on Au fingers connected to the negative terminal. This is understandable because etching of Si in HF requires a bond exchange with

negatively charged fluorine ions.[23,29] The negative Au electrode should therefore repel these ions and prevent etching from taking place.

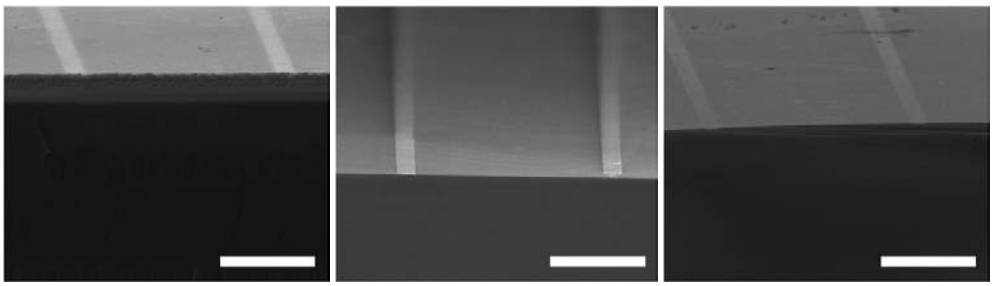

(a) (b) (c)

Figure 6.7: Cross-sectional SEM images of 20-µm-apart Au fingers connected to the negative terminal and etched using BiMACE for (a) double-side polished p-type Si (100) of resistivity 1-10 Ω.cm with U = 2 V for 20 minutes; (b) single-side polished n-type Si (100) of resistivity≤ 0.005 Ω.cm with U = 1 V for 30 minutes; (c) double-side polished n-type Si (100) of resistivity 1-10 Ω.cm with U = 2 V for 20 minutes. [HF] is fixed at 1.73 M for all the samples. The scale bar for the SEM images is 10 µm.

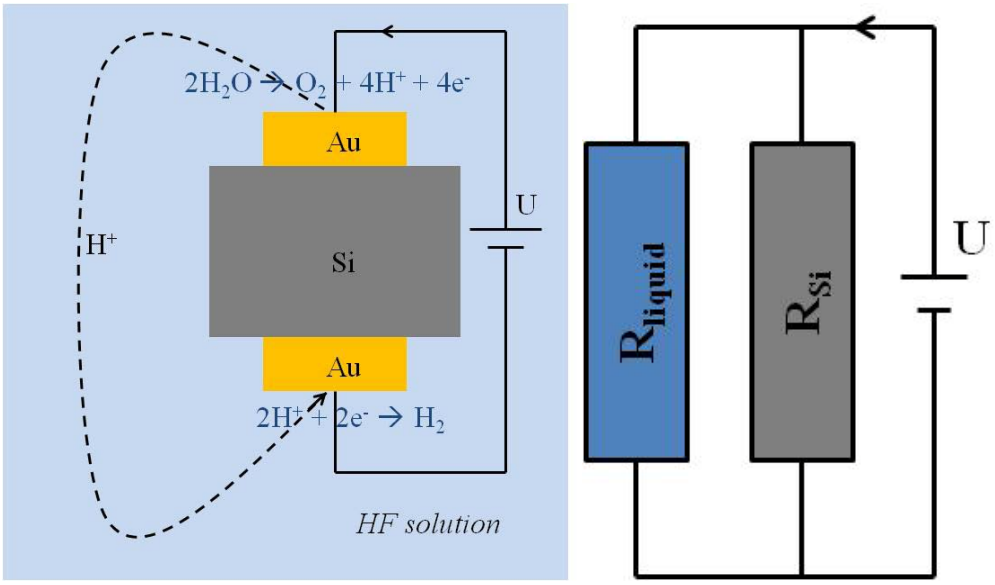

(a) (b)

Figure 6.8: (a) Schematic illustrating possible conduction paths in BiMACE. (b) Electrical circuit representation of BiMACE system.

Figure 6.8a shows two possible conduction paths in the BiMACE system, namely through the Si and through the solution (ionic current). This etching system can be represented as an electrical circuit consisting of two parallel resistances, R_{Si} and R_{liquid}, connected to a potential difference, U, as shown in **Figure 6.8b**. R_{liquid} corresponds to several possible chemical

reactions in the etching system, such as the etching of Si (**Equation 6.2**) and the electrolysis reactions of water,[79]

$$2H_2O \rightarrow O_2 + 4H^+ + 4e^-$$

Equation 6.5

$$2H^+ + 2e^- \rightarrow H_2$$

Equation 6.6

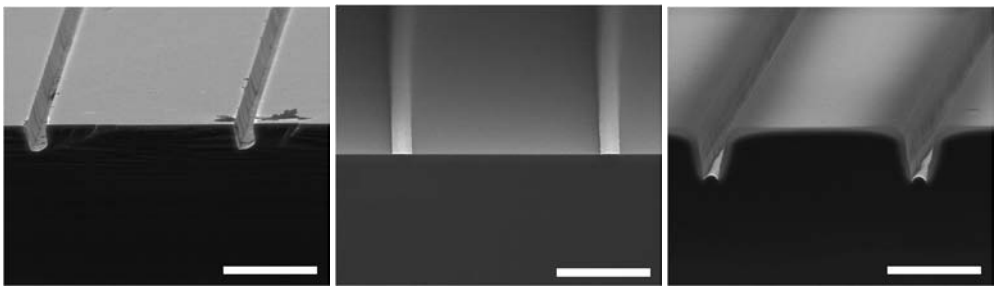

(a) (b) (c)

Figure 6.9: Cross-sectional SEM images of 20-μm-apart Au fingers etched using BiMACE for (a) double-side polished p-type Si (100) of resistivity 1-10 Ω.cm with U = 2 V for 20 minutes; (b) single-side polished n-type Si (100) of resistivity ≤ 0.005 Ω.cm with U = 1 V for 30 minutes; (c) double-side polished n-type Si (100) of resistivity 1-10 Ω.cm with U = 2 V for 20 minutes. [HF] is fixed at 1.73 M for all the samples. The scale bar for the SEM images is 10 μm.

For the case of p-type Si (double-side polished and patterned, with resistivity of 1-10 Ω.cm), I_{before} and I_{after} are ~1.17 and ~1.2 A, respectively, for U = 2 V. From the current reading before immersion, we can extract the value of R_{Si} to be ~1.72 Ω. From the current reading after immersion, we obtain the value of the parallel resistance to be ~ 1.67 Ω, from which we can extract the value of R_{liquid} to be (1.72 x 1.67) / (1.72 – 1.67) = 57.4 Ω. Since the liquid is much more resistive than the system, hole current is expected to flow anisotropically from the top to the bottom electrode. As a result, the etching is localized in the vicinity of the catalyst, as shown in **Figure 6.9a**.

For the case of n^+-type Si (single-side polished and patterned, with resistivity of ≤ 0.005 Ω.cm), I_{before} and I_{after} are ~1.17 and ~1.28 A,

respectively, for U = 1 V. From the current reading before immersion, we can extract the value of the total contact resistance R_{Si} to be ~0.85 Ω. From the current reading after immersion, we obtain the value of the parallel resistance to be ~ 0.78 Ω, from which we can extract the value of R_{liquid} to be (0.85 x 0.78) / (0.85 – 0.78) = 9.47 Ω. Since the liquid is much more resistive than the system, electron current is expected to flow anisotropically from the bottom to the top electrode. However, this electron current should not result in any etching because holes are required for etching of Si in HF. **Figure 6.9b** supports this argument in that no etching took place beneath the Au fingers even after immersion in the solution for 30 minutes.

For the case of n-type Si (double-side polished and patterned, with resistivity of 1-10 Ω.cm), I_{before} and I_{after} are <1 and ~28 mA, respectively, for U = 2 V. From the current reading before immersion, we can extract the value of the total contact resistance R_{Si} to be ~2 kΩ. From the current reading after immersion, we obtain the value of the parallel resistance to be ~ 71.4 Ω, from which we can extract the value of R_{liquid} to be (2000 x 71.4) / (2000 – 71.4) = 74 Ω. In contrast to the previous two cases, the liquid is now much more conductive than the system. Therefore, when the sample is immersed in the etchant, the Si simply acts as an open switch and the electrical circuit is now completed by electrolysis reactions via electron injection from the solution into the top Au electrode/anode (**Equation 6.5**) and electron injection from the bottom Au electrode/cathode to the solution (**Equation 6.6**). It has been reported that the etching of Si using noble metal catalyst in HF is greatly enhanced with O_2 bubbling, indicating the role of O_2 as an oxidizing agent via

its reduction reaction on the catalyst.[80] The generation of O_2 bubbles at the anode therefore serves as a source of holes required for etching of Si. **Figure 6.9c** indeed shows that etching occurred significantly on the n-type sample. The tapered sidewall of and the formation of porous region around the etched trenches indicate that there is a significant amount of holes injected to the anode via this electrolysis mechanism.

If electrolysis is the mechanism responsible for etching on n-type Si, one would expect that etching only occurs when the applied voltage (U) exceeds the standard potential for electrolysis of water, 1.229 V.[81] Therefore, we have also tried to etch the n-type sample with U = 0.5 and 1.4 V, as shown in **Figure 6.10a** and **b**, respectively. As expected, there is no etching for U = 0.5 V and etching occurs when U exceeds 1.229 V. The less prominent etching for U = 1.4 V (**Figure 6.10b**) compared to U = 2 V (**Figure 6.9c**) is expected due to its lower over-potential.

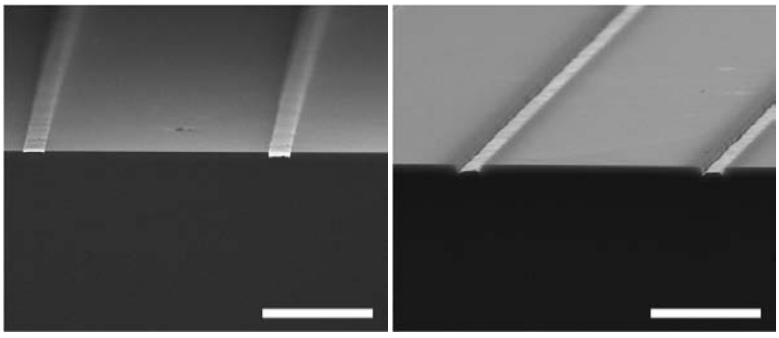

(a) (b)

Figure 6.10: Cross-sectional SEM images of 20-μm-apart Au fingers etched using BiMACE for double-side polished n-type Si (100) of resistivity 1-10 Ω.cm for (a) U = 0.5 V and (b) U = 1.4 V. [HF] is fixed at 1.73 M and etching duration is 20 minutes. The scale bar for the SEM images is 10 μm.

6.5 BiMACE to Fabricate Nanowires

Motivated by the results of the etched micron-sized features, we have also explored BiMACE to etch Si nanowires. For this purpose, we have

employed interference lithography[19] to pattern resist dot array on the Si. As in the case of Au finger structure (**Figure 6.1c**), it is necessary to have a base through which the bias will be applied to the Au catalyst later. This is accomplished by carrying out a UV flood exposure on half portion of the samples prior to the interference lithography step. After Au deposition, lifting off the resist patterns will leave behind Au film with circular perforations connected to an Au pad as shown in **Figure 6.11a**. **Figure 6.11b** shows Si nanowires etched using BiMACE (U = 1.5 V for 35 minutes) for a fixed [HF] of 4.6 M.

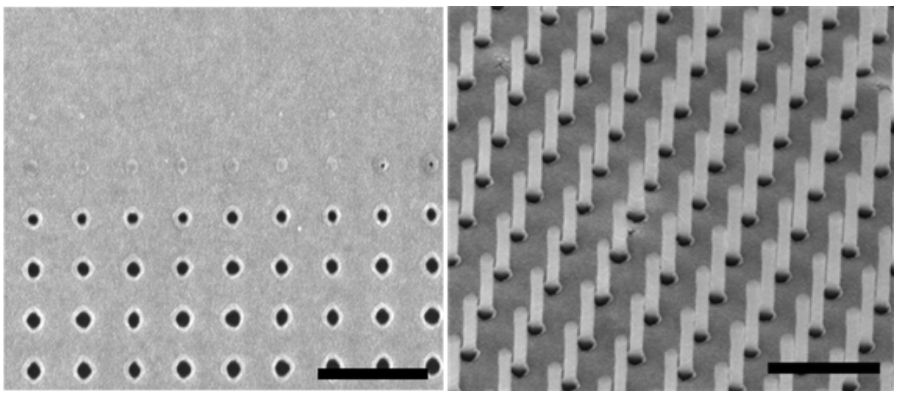

(a) (b)

Figure 6.11: (a) SEM image of Au perforated film connected to an Au pad. (b) Tilted-view SEM image of Si nanowires etched using BiMACE with U = 1.5 V and [HF] = 4.6 M for 35 minutes. Scale bar for the SEM image is 2 μm.

Recently, there has been much interest in fabricating nanowires using MACE on technologically important semiconductor materials other than Si, such as silicon germanium (SiGe),[34] gallium arsenide (GaAs),[35,36] and gallium nitride (GaN).[37] However, the etching morphology is generally dependent on the oxidant concentration.[36,37] The possibility of etching without oxidant using BiMACE might pave the way for a better control in etching of semiconductor materials other than silicon.

Chapter 7. Conclusion

7.1 Summary

The main objectives of this thesis were to investigate the mechanism and catalyst stability of MACE of Si in HF and H_2O_2 with isolated and interconnected catalyst as well as to develop ways to control the flow of electronic holes in the etching process.

First, the role of electronic holes on etching underneath Au was presented. The role of excess holes was characterized through observations of pit formation as a function of catalyst proximity and the ratio of the H_2O_2 and HF concentrations in the etch solution. We showed that suppression of excess hole generation, and therefore pitting, can be achieved by either adding NaCl to the etch solution or by increasing the HF concentration relative to the H_2O_2 concentration. We also demonstrated that an external electric field can be used to direct most of the excess holes to the back of the Si wafer, and thus reduce pit formation at the surface of the Si between the Au catalysts. We also explored the role of Au back contact on the etching characteristics for three different cases: (i) back contact is exposed to the etchant, (ii) back contact is not exposed to the etchant, and (iii) etching with an additional current injection from an applied bias. Next, we proposed that there are two possible causes for catalyst instability during MACE, namely the overlap of excess holes between neighboring catalysts and the generation of hydrogen (H_2) bubbles. From these two modes of instability, we defined a regime of etch chemistry and catalyst spacing for which catalyst stability and vertical etching can be achieved.

Next, we investigated the etching characteristics with interconnected

catalyst configuration patterned by interference lithography (IL). We proposed that the role of excess holes is more significant in IL-patterned catalyst configuration such that the etched nanostructures possess a relatively high degree of porosity. We demonstrated that the porosity of the nanostructures can be exploited to obtain an ordered array of Si nanocones,[21] which may find applications in biomedical research, scanning probe nanolithography, or field-emitting-tip devices. The influence of doping type and concentration on the porosity of nanowires was examined. We further demonstrated that the porosity of the nanostructures can be tuned from the etchant composition.

Finally, we used an electric field to develop a new etching method called bias- and metal-assisted chemical etching (BiMACE) of Si. Essential features of BiMACE were presented and comparisons were made between MACE and BiMACE. Quantitative analysis of the hole contribution to BiMACE without and with H_2O_2 was presented. The etching mechanism of BiMACE was discussed. Application of BiMACE to fabricate Si nanowires was also demonstrated and its possible extension to other semiconductor materials was suggested.

To conclude, this work has provided a better understanding on the mechanism and catalyst stability of MACE of Si. The essential role of electronic holes was elucidated from the series of experiments and this may provide ways to achieve 3D sculpturing of Si or even other semiconductor materials.

7.2 Recommendations

Based on the results obtained in this research work, several avenues are available as potential future research topics:

- Since catalyst instability depends on the mechanical properties (such as moment of inertia) of the catalyst,[33] it will be interesting to investigate the etching stability of isolated catalyst with different sizes (length and width) and geometries, e.g. ring structure.
- Since other noble metals also catalyze etching of Si in HF and H_2O_2,[18,29] it will be useful to carry out similar mechanistic studies using Pt or Ag catalysts.
- Since we have demonstrated the applicability of electric field to control the flow of electronic holes in MACE, it will be interesting to extend this method to fabricate non-porous nanowires on heavily doped Si wafers for nanocapacitor application.[82] It will also be very useful to optimize this method to manipulate the etching direction.
- Since we have demonstrated BiMACE capability to etch Si without oxidant, it might pave the way for a better control in etching of semiconductor materials other than Si, which is difficult to achieve at present with MACE because the etching morphology is dependent on the oxidant concentration.[36,37]

Appendix A. Etching in an Electric Field for $[H_2O_2]$ = 0.46 M

Figures A1a, **b** and **c** show SEM images of three samples etched with [HF] = 1.73 M and $[H_2O_2]$ = 0.46 M with U = 0, 10 and 100 V. For the sample with U = 0 V, excess holes diffused into Regions A and B (**Figure A1a**) to form pits as described in **Section 4.4**. With U = 10 V, the excess holes are drawn toward the bulk of Si resulting in less pitting in Regions A and B (**Figure A1b**). The effect of the electric field in drawing the holes to the bulk of Si is even more significant for U = 100 V (**Figure A1c**). It was also found that the etch rate decreased with increasing electric field. For samples etched with U = 0, 10 and 100 V, the etch rates were 0.062, 0.019, and 0.009 μm/min, respectively.

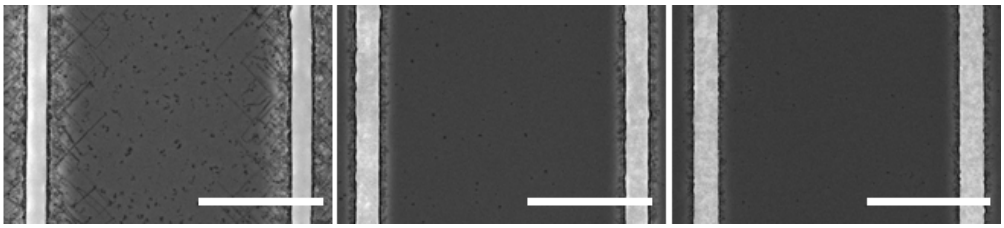

(a) (b) (c)

Figure A1: (a)-(c) Top-view SEM images of samples with an Au strip spacing of 20 μm etched for 15 minutes in [HF] = 1.73 M and $[H_2O_2]$ = 0.46 M with U = 0, 10, and 100 V, respectively. The scale bar for the SEM images is 10 μm.

Appendix B. Determination of *D* Value

From **Figures B1b** and **c**, the value of the hole diffusion distance can be estimated as

$$L_p = \sqrt{1.7^2+0.8^2} \times 10^{-6}m = 1.88 \times 10^{-6}m$$

So, the hole diffusivity can be obtained using

$$\sqrt{Dt} = L_p \ ,$$

to determine that D=2.94 x 10^{-15} m^2/s.

(a)

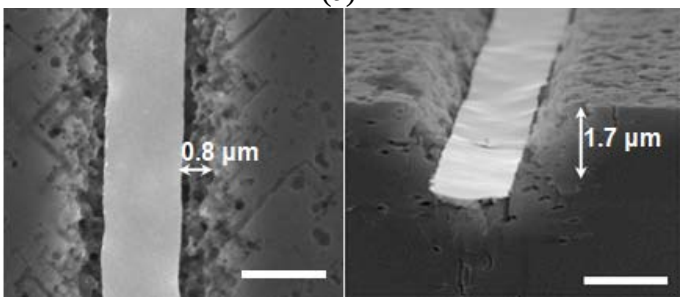

(b) (c)

Figure B1: (a) Schematic of 2-D isotropic hole diffusion inside Si during etching. (b)–(c) Top-view and cross-sectional SEM images of an etched sample with strip spacing of 20 µm, etched with [H_2O_2] = 1.21 M. The [HF] was fixed at 1.73 M and the etch duration was 20 minutes. The scale bar is 2 µm.

Appendix C. Summary of SEM Images Used for Construction of the Etch Stability Diagram

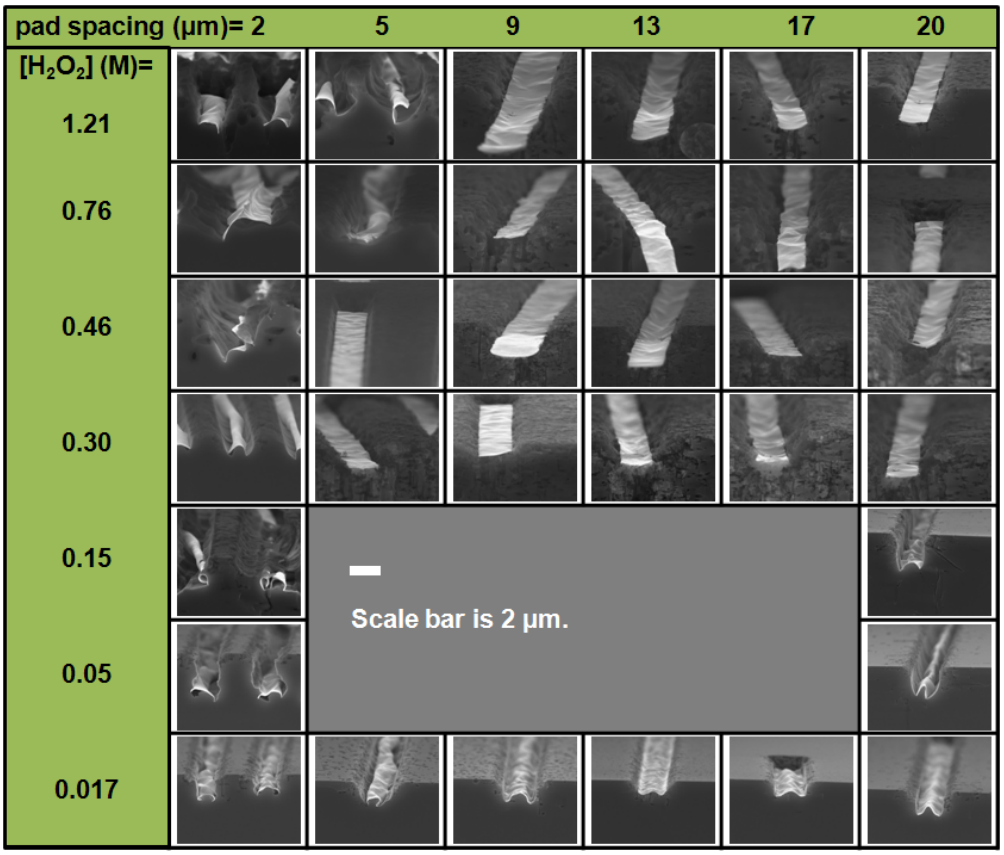

Figure C1: Cross-sectional SEM images of the etched samples used to construct the stability diagram in **Figure 4.17**. [HF] was fixed at 1.73 M.

Appendix D. Si Nanofins Etched with Different [H_2O_2]

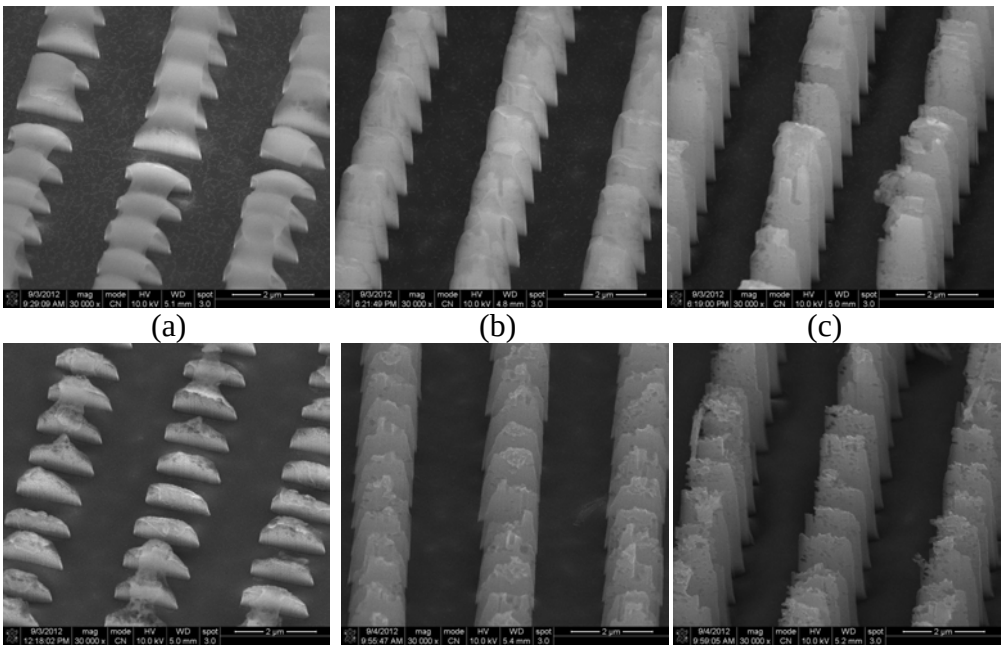

(a) (b) (c)

(d) (e) (f)

Figure D1: Si nanofins etched with: (a) [H_2O_2] = 0.46 M for 10 minutes, (b) [H_2O_2] = 0.2 M for 30 minutes, and (c) [H_2O_2] = 0.09 M for 90 minutes. [HF] was fixed at 1.73 M. (d)-(f) are SEM images of the nanofins shown in (a)-(c), after aged for ~ 1 day in atmospheric condition and etched in 10% HF for 1 minute. The etch rates for (a), (b), and (c) are 300, 120, and 60 nm/min, respectively.

Appendix E. Si Nanofins Etched with Different [HF]

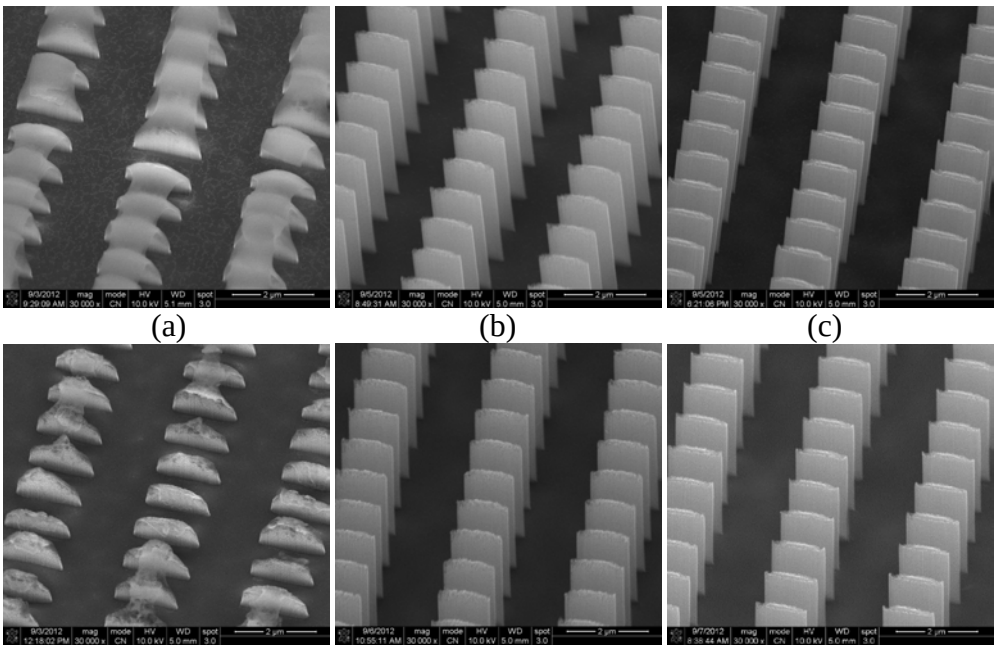

(a) (b) (c)

(d) (e) (f)

Figure E1: Si nanofins etched with: (a) [HF] = 1.73 M for 10 minutes, (b) [HF] = 4.6 M for 8 minutes, and (c) [HF] = 8.63 M for 10 minutes. [H_2O_2] was fixed at 0.46 M. (d)-(f) are SEM images of the nanofins shown in (a)-(c), after aged for ~ 1 day in atmospheric condition and etched in 10% HF for 1 minute. The etch rates for (a), (b), and (c) are 300, 500, and 400 nm/min, respectively.

Appendix F. Role of Extraneous Au Nanoparticles

We notice that the etched nanostructures using our IL-MACE method always contain surface damage at the top portion, as can be seen in **Figure F1**. In this section, we explore the role of extraneous Au NPs in creating this surface damage. We demonstrate that by employing an ARC layer beneath the PR in the lithographic step, the contribution of these extraneous Au NPs is eliminated and it is possible to obtain Si nanostructures without surface damage.

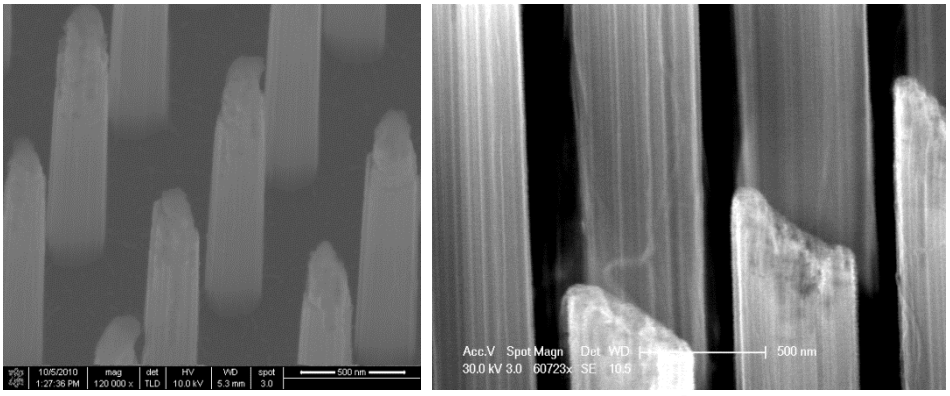

(a) (b)

Figure F1: (a) Si nanowires etched for 6 minutes. (b) Si nanofins etched for 5 minutes. [HF] and [H_2O_2] were 4.6 and 0.46 M, respectively. Surface damage is obvious at the top portion of both nanostructures.

F.1 Role of Extraneous Au Nanoparticles

The standing wave pattern generated due to reflection of the laser from the Si substrate in the PR during IL exposure generates PR pattern with scalloped sidewall. This allows Au NPs to decorate the rim of the base of the PR during Au deposition step, as schematically illustrated in **Figure F2a**. **Figure F2b** shows the Si sample with PR posts after Au deposition and the scalloped sidewall of the PR is clearly revealed. After removing the PR posts

via lift-off process, the presence of Au NPs can be observed at the rim of the void (**Figure F2c**), as suggested earlier. To investigate the role of these extraneous Au NPs, the sample was etched for 1 minute and the result is shown in **Figure F2d**. It can be seen that these Au NPs have etched numerous pores around the edges of the Si surface. Besides, there are also horizontal pores oriented along <100> directions in the middle region of the Si surface. This anisotropic etching along <100> directions is typical of isolated catalyst (e.g. NPs) and in agreement with the finding reported by Tsujino and Matsumura.[24] This nanopore formation by the Au NPs is therefore expected to result in a considerable surface damage when the nanostructures are etched deeper, as shown in **Figure F1**.

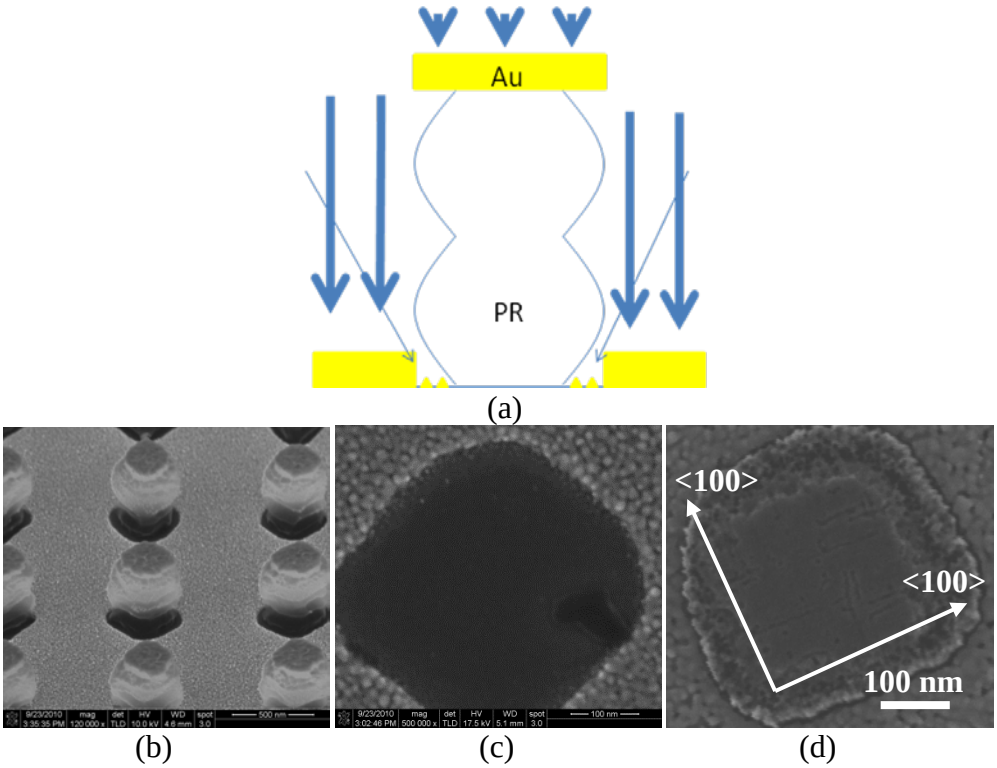

(a) (b) (c) (d)

Figure F2: (a) Schematic diagram illustrating the deposition of extraneous Au NPs on the Si surface beneath the scalloped PR sidewall. (b)-(d) Si sample with PR posts after: (b) Au deposition, (c) lift-off of PR posts, and (d) etching for 1 minute.

F.2 Elimination of Extraneous Au Nanoparticles using Anti-Reflection-Coating Layer

To prevent the Au NPs from being deposited on the Si surface, we have modified the experimental procedures by employing an ARC layer, as schematically illustrated in **Figure F3**. The Si wafer was first coated with an XHRiC-16 ARC layer (~ 100-nm thicknes) and baked at 175°C for 3 minutes. An Ultra-i 123 PR layer was then coated on the sample and baked at 90°C for 90 seconds. The sample was exposed using a Lloyd's-mirror type IL setup with a HeCd laser source (λ = 325 nm), baked at 110°C for 90 seconds, and developed in Microposit MF CD-26 to obtain periodic PR patterns on Si. The pattern was transferred to the ARC layer using O_2 plasma at a pressure of 0.2 Torr and power of 200 W for an etching time of 80 seconds. Afterwards, the sample was coated with 15-nm Au using thermal evaporation at a base pressure of ~ 10^{-6} Torr. The sample was then etched in a mixture of H_2O, HF, and H_2O_2 at room temperature with the [HF] and [H_2O_2] fixed at 4.6 and 0.46 M, respectively. Afterwards, the Au was removed using a standard iodine-based Au etchant and the PR was dissolved in acetone.

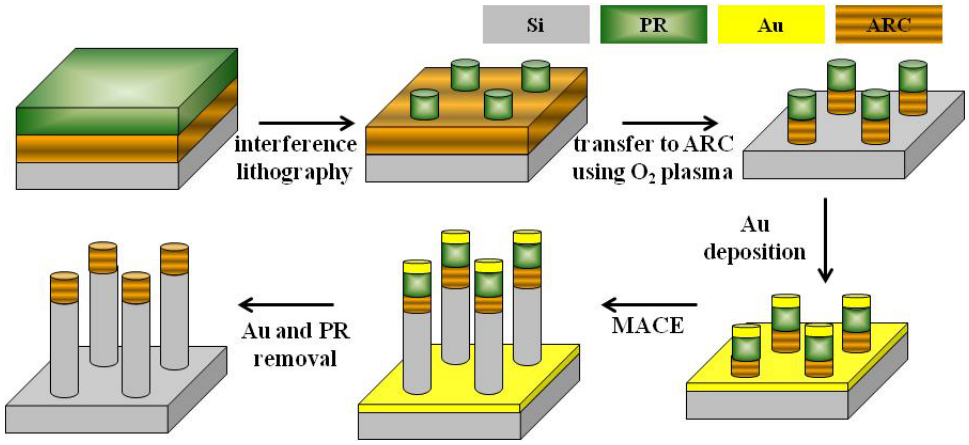

Figure F3: Schematic diagrams illustrating fabrication of Si nanowires or nanofins using a combination of interference lithography and MACE with additional ARC layer.

As shown in **Figure F4a**, even if there is still some standing wave in the PR, the Au NPs can only occupy the space beneath the PR and not on the Si surface. In practice, as shown in **Figure F4b**, the ARC posts have sloping sidewall because the PR is also trimmed sideway during the O_2 plasma step to transfer the pattern to the ARC layer. It can be seen that the extraneous Au NPs are deposited on the ARC and therefore will not contribute to etching when immersed in HF and H_2O_2. Etching results using this bilayer resist stack are shown in **Figures F4c** and **d**. As can be seen, we are now able to fabricate Si nanowires and nanofins without surface damage at the top portion (*c.f.* **Figures F4c**, **d** and **Figures F1a**, **b**).

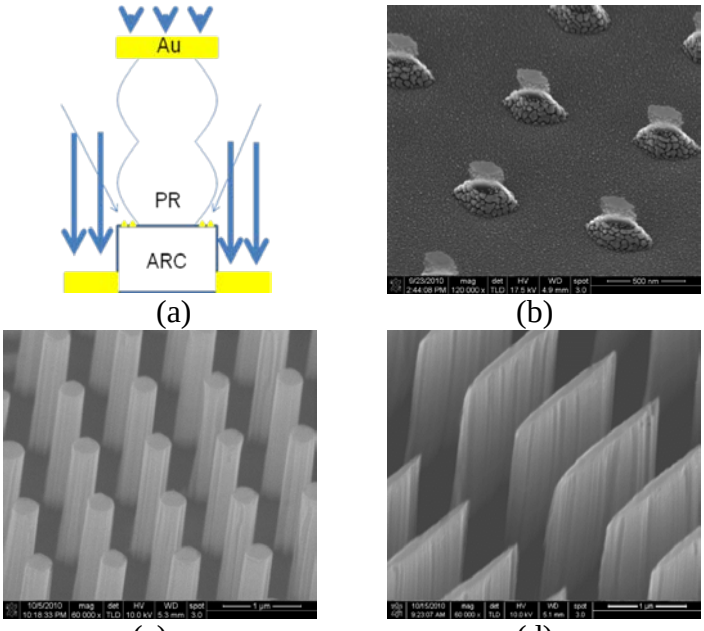

Figure F4: (a) Schematic diagram illustrating the elimination of extraneous Au nanoparticle deposition on the Si surface by using an ARC layer beneath the PR. (b) Si sample with PR+ARC posts after Au deposition. (c) Si nanowires after etching sample (b) for 7.5 minutes. (d) Si nanofins etched for 5 minutes using the same procedure.

Appendix G. References

1. Feynman, R. P. There's plenty of room at the bottom. *Engineering and Science* **23**, 22–36 (1960).

2. Cui, Y., Zhong, Z., Wang, D., Wang, W. U. & Lieber, C. M. High Performance Silicon Nanowire Field Effect Transistors. *Nano Lett.* **3**, 149–152 (2003).

3. Goldberger, J., Hochbaum, A. I., Fan, R. & Yang, P. Silicon Vertically Integrated Nanowire Field Effect Transistors. *Nano Lett.* **6**, 973–977 (2006).

4. Cui, L.-F., Ruffo, R., Chan, C. K., Peng, H. & Cui, Y. Crystalline-Amorphous Core−Shell Silicon Nanowires for High Capacity and High Current Battery Electrodes. *Nano Lett.* **9**, 491–495 (2008).

5. Teki, R., Datta, M. K., Krishnan, R., Parker, T. C., Lu, T.-M., Kumta, P. N. & Koratkar, N. Nanostructured Silicon Anodes for Lithium Ion Rechargeable Batteries. *Small* **5**, 2236–2242 (2009).

6. Hochbaum, A. I., Chen, R., Delgado, R. D., Liang, W., Garnett, E. C., Najarian, M., Majumdar, A. & Yang, P. Enhanced thermoelectric performance of rough silicon nanowires. *Nature* **451**, 163–167 (2008).

7. Cui, Y., Wei, Q., Park, H. & Lieber, C. M. Nanowire Nanosensors for Highly Sensitive and Selective Detection of Biological and Chemical Species. *Science* **293**, 1289–1292 (2001).

8. Murthy, B. R., Ng, J. K. K., Selamat, E. S., Balasubramanian, N. & Liu, W. T. Silicon nanopillar substrates for enhancing signal intensity in DNA microarrays. *Biosensors and Bioelectronics* **24**, 723–728 (2008).

9. Kelzenberg, M. D., Boettcher, S. W., Petykiewicz, J. A., Turner-Evans, D. B., Putnam, M. C., Warren, E. L., Spurgeon, J. M., Briggs, R. M., Lewis, N. S. & Atwater, H. A. Enhanced absorption and carrier collection in Si wire arrays for photovoltaic applications. *Nature Materials* **9**, 239–244 (2010).

10. Peng, K.-Q., Wang, X., Li, L., Wu, X.-L. & Lee, S.-T. High-Performance Silicon Nanohole Solar Cells. *J. Am. Chem. Soc.* **132**, 6872–6873 (2010).

11. Wang, H.-P., Lai, K.-Y., Lin, Y.-R., Lin, C.-A. & He, J.-H. Periodic Si Nanopillar Arrays Fabricated by Colloidal Lithography and Catalytic Etching for Broadband and Omnidirectional Elimination of Fresnel Reflection. *Langmuir* **26**, 12855–12858 (2010).

12. Oh, Y.-J., Ross, C. A., Jung, Y. S., Wang, Y. & Thompson, C. V. Cobalt Nanoparticle Arrays made by Templated Solid-State Dewetting. *Small* **5**, 860–865 (2009).

13. Wagner, R. S. & Ellis, W. C. Vapor-Liquid-Solid Mechanism of Single Crystal Growth. *Appl. Phys. Lett.* **4**, 89 (1964).

14. Hisamoto, D., Lee, W.-C., Kedzierski, J., Takeuchi, H., Asano, K., Kuo, C., Anderson, E., King, T.-J., Bokor, J. & Hu, C. FinFET-a self-aligned double-gate MOSFET scalable to 20 nm. *Electron Devices, IEEE Transactions on* **47**, 2320 – 2325 (2000).

15. Kedzierski, J., Ieong, M., Nowak, E., Kanarsky, T. S., Zhang, Y., Roy, R., Boyd, D., Fried, D. & Wong, H.-S. P. Extension and source/drain design for high-performance FinFET devices. *Electron Devices, IEEE Transactions on* **50**, 952 – 958 (2003).

16. Wu, Y., Cui, Y., Huynh, L., Barrelet, C. J., Bell, D. C. & Lieber, C. M. Controlled Growth and Structures of Molecular-Scale Silicon Nanowires. *Nano Lett.* **4**, 433–436 (2004).

17. Schmidt, V., Senz, S. & Gösele, U. The shape of epitaxially grown silicon nanowires and the influence of line tension. *Applied Physics A: Materials Science & Processing* **80**, 445–450 (2005).

18. Li, X. & Bohn, P. W. Metal-assisted chemical etching in HF/H2O2 produces porous silicon. *Appl. Phys. Lett.* **77**, 2572–2574 (2000).

19. Choi, W. K., Liew, T. H., Dawood, M. K., Smith, H. I., Thompson, C. V. & Hong, M. H. Synthesis of Silicon Nanowires and Nanofin Arrays Using Interference Lithography and Catalytic Etching. *Nano Letters* **8**, 3799–3802 (2008).

20. Chang, S., Chuang, V. P., Boles, S. T. & Thompson, C. V. Metal-Catalyzed Etching of Vertically Aligned Polysilicon and Amorphous Silicon Nanowire Arrays by Etching Direction Confinement. *Advanced Functional Materials* **20**, 4364–4370 (2010).

21. Dawood, M. K., Liew, T. H., Lianto, P., Hong, M. H., Tripathy, S., Thong, J. T. L. & Choi, W. K. Interference lithographically defined and catalytically etched, large-area silicon nanocones from nanowires. *Nanotechnology* **21**, 205305 (2010).

22. Lee, C.-L., Tsujino, K., Kanda, Y., Ikeda, S. & Matsumura, M. Pore formation in silicon by wet etching using micrometre-sized metal particles as catalysts. *J. Mater. Chem.* **18**, 1015 (2008).

23. Huang, Z., Geyer, N., Werner, P., de Boor, J. & Gösele, U. Metal-Assisted Chemical Etching of Silicon: A Review. *Adv. Mater.* **23**, 285–308 (2011).

24. Tsujino, K. & Matsumura, M. Morphology of nanoholes formed in silicon by wet etching in solutions containing HF and H2O2 at different concentrations using silver nanoparticles as catalysts. *Electrochimica Acta* **53**, 28–34 (2007).

25. Hildreth, O. J., Lin, W. & Wong, C. P. Effect of Catalyst Shape and Etchant Composition on Etching Direction in Metal-Assisted Chemical Etching of Silicon to Fabricate 3D Nanostructures. *ACS Nano* **3**, 4033–4042 (2011).

26. Choi, W. K., Liew, T. H., Chew, H. G., Zheng, F., Thompson, C. V., Wang, Y., Hong, M. H., Wang, X. D., Li, L. & Yun, J. A Combined Top-Down and Bottom-Up Approach for Precise Placement of Metal Nanoparticles on Silicon. *Small* **4**, 330–333 (2008).

27. Ahn, M., Heilmann, R. K. & Schattenburg, M. L. Fabrication of ultrahigh aspect ratio freestanding gratings on silicon-on-insulator wafers. *Journal of Vacuum Science & Technology B: Microelectronics and Nanometer Structures* **25**, 2593 (2007).

28. Nassiopoulos, A. G., Grigoropoulos, S., Gogolides, E. & Papadimitriou, D. Visible luminescence from one- and two-dimensional silicon structures produced by conventional lithographic and reactive ion etching techniques. *Applied Physics Letters* **66**, 1114–1116 (1995).

29. Chartier, C., Bastide, S. & Lévy-Clément, C. Metal-assisted chemical etching of silicon in HF-H2O2. *Electrochimica Acta* **53**, 5509–5516 (2008).

30. Peng, K. Q., Hu, J. J., Yan, Y. J., Wu, Y., Fang, H., Xu, Y., Lee, S. T. & Zhu, J. Fabrication of Single-Crystalline Silicon Nanowires by Scratching a Silicon Surface with Catalytic Metal Particles. *Adv. Funct. Mater.* **16**, 387–394 (2006).

31. Hadjersi, T. Oxidizing agent concentration effect on metal-assisted electroless etching mechanism in HF-oxidizing agent-H2O solutions. *Applied Surface Science* **253**, 4156–4160 (2007).

32. Tsujino, K. & Matsumura, M. Helical Nanoholes Bored in Silicon by Wet Chemical Etching Using Platinum Nanoparticles as Catalyst. *Electrochem. Solid-State Lett.* **8**, C193 (2005).

33. Hildreth, O. J., Brown, D. & Wong, C. P. 3D Out-of-Plane Rotational Etching with Pinned Catalysts in Metal-Assisted Chemical Etching of Silicon. *Advanced Functional Materials* **21**, 3119–3128 (2011).

34. Wang, X., Pey, K. L., Choi, W. K., Ho, C. K. F., Fitzgerald, E. & Antoniadis, D. Arrayed Si/SiGe Nanowire and Heterostructure Formations via Au-Assisted Wet Chemical Etching Method. *Electrochem. Solid-State Lett.* **12**, K37 (2009).

35. Yasukawa, Y., Asoh, H. & Ono, S. Periodic GaAs Convex and Hole Arrays Produced by Metal-Assisted Chemical Etching. *Japanese Journal of Applied Physics* **49**, 116502 (2010).

36. DeJarld, M., Shin, J. C., Chern, W., Chanda, D., Balasundaram, K., Rogers, J. A. & Li, X. Formation of High Aspect Ratio GaAs

Nanostructures with Metal-Assisted Chemical Etching. *Nano Lett.* **11**, 5259–5263 (2011).

37. Geng, X., Duan, B. K., Grismer, D. A., Zhao, L. & Bohn, P. W. Monodisperse GaN nanowires prepared by metal-assisted chemical etching with in situ catalyst deposition. *Electrochemistry Communications* **19**, 39–42 (2012).

38. Chen, C.-Y., Wu, C.-S., Chou, C.-J. & Yen, T.-J. Morphological Control of Single-Crystalline Silicon Nanowire Arrays near Room Temperature. *Adv. Mater.* **20**, 3811–3815 (2008).

39. Ramette, R. W. Outmoded terminology: The normal hydrogen electrode. *J. Chem. Educ.* **64**, 885 (1987).

40. Canham, L. T. Silicon quantum wire array fabrication by electrochemical and chemical dissolution of wafers. *Appl. Phys. Lett.* **57**, 1046–1048 (1990).

41. Chattopadhyay, S., Li, X. & Bohn, P. W. In-plane control of morphology and tunable photoluminescence in porous silicon produced by metal-assisted electroless chemical etching. *Journal of Applied Physics* **91**, 6134–6140 (2002).

42. Hochbaum, A. I., Gargas, D., Hwang, Y. J. & Yang, P. Single Crystalline Mesoporous Silicon Nanowires. *Nano Lett.* **9**, 3550–3554 (2009).

43. Physical Chemistry Division Commission on Colloid and Surface Chemistry Including Catalysis, McCusker, L. B., Liebau, F. & Engelhardt, G. Nomenclature of structural and compositional characteristics of ordered microporous and mesoporous materials with inorganic hosts: (IUPAC recommendations 2001). *Microporous and Mesoporous Materials* **58**, 3–13 (2003).

44. De Boor, J., Geyer, N., Wittemann, J. V., Gösele, U. & Schmidt, V. Sub-100 nm silicon nanowires by laser interference lithography and metal-assisted etching. *Nanotechnology* **21**, 095302 (2010).

45. Chang, S.-W., Chuang, V. P., Boles, S. T., Ross, C. A. & Thompson, C. V. Densely Packed Arrays of Ultra-High-Aspect-Ratio Silicon Nanowires Fabricated using Block-Copolymer Lithography and Metal-Assisted Etching. *Advanced Functional Materials* **19**, 2495–2500 (2009).

46. Peng, K., Zhang, M., Lu, A., Wong, N.-B, Zhang, R. & Lee, S.-T. Ordered silicon nanowire arrays via nanosphere lithography and metal-induced etching. *Applied Physics Letters* **90**, 163123–163123–3 (2007).

47. Huang, Z., Shimizu, T., Senz, S., Zhang, Z., Zhang, X., Lee, W., Geyer, N. & Gösele, U. Ordered Arrays of Vertically Aligned [110] Silicon Nanowires by Suppressing the Crystallographically Preferred <100> Etching Directions. *Nano Lett.* **9**, 2519–2525 (2009).

48. Smith, R. L. & Collins, S. D. Porous silicon formation mechanisms. *Journal of Applied Physics* **71**, R1–R22 (1992).

49. Tsujino, K. & Matsumura, M. Boring Deep Cylindrical Nanoholes in Silicon Using Silver Nanoparticles as a Catalyst. *Advanced Materials* **17**, 1045–1047 (2005).

50. Bauer, S., Brunner, J. G., Jha, H., Yasukawa, Y., Asoh, H., Ono, S., Böhm, H., Spatz, J. P. & Schmuki, P. Ordered nanopore boring in silicon: Metal-assisted etching using a self-aligned block copolymer Au nanoparticle template and gravity accelerated etching. *Electrochemistry Communications* **12**, 565–569 (2010).

51. Huang, Z., Shimizu, T., Senz, S., Zhang, Z., Geyer, N. & Gösele, U. Oxidation rate effect on the direction of metal-assisted chemical and electrochemical etching of silicon. *The Journal of Physical Chemistry C* **114**, 10683–10690 (2010).

52. Chun, I. S., Chow, E. K. & Li, X. Nanoscale three dimensional pattern formation in light emitting porous silicon. *Applied Physics Letters* **92**, 191113–1–191113–3 (2008).

53. Paxton, W. F., Baker, P. T., Kline, T. R., Wang, Y., Mallouk, T. E. & Sen, A.. Catalytically Induced Electrokinetics for Motors and Micropumps. *J. Am. Chem. Soc.* **128**, 14881–14888 (2006).

54. Peng, K., Lu, A., Zhang, R. & Lee, S.-T. Motility of Metal Nanoparticles in Silicon and Induced Anisotropic Silicon Etching. *Adv. Funct. Mater.* **18**, 3026–3035 (2008).

55. Uhlir, Jr., A. Electrolytic Shaping of Germanium and Silicon. *Bell System Technical Journal* **35**, 333–347 (1956).

56. Gösele, U. & Lehmann, V. Light-emitting porous silicon. *Materials chemistry and physics* **40**, 253–259 (1995).

57. Barillaro, G., Nannini, A. & Piotto, M. Electrochemical etching in HF solution for silicon micromachining. *Sensors and Actuators A: Physical* **102**, 195–201 (2002).

58. Kern, W. & Puotinen, D. A. Cleaning solutions based on hydrogen peroxide for use in silicon semiconductor technology. *RCA Review* **31**, 187–206 (1970).

59. Kern, W. The Evolution of Silicon Wafer Cleaning Technology. *J. Electrochem. Soc.* **137**, 1887–1892 (1990).

60. Ghandhi, S. K. *VLSI Fabrication Principles: Silicon and Gallium Arsenide, 2nd Edition*. (Wiley-Interscience: 1994).

61. Plummer, J. D., Deal, M. D. & Griffin, P. B. *Silicon VLSI Technology: Fundamentals, Practice, and Modeling*. (Prentice Hall: 2000).

62. Smith, H. I. A review of submicron lithography. *Superlattices and Microstructures* **2**, 129–142 (1986).

63. Smith, H. I. Low cost nanolithography with nanoaccuracy. *Physica E: Low-dimensional Systems and Nanostructures* **11**, 104–109 (2001).

64. Senturia, S. D. *Microsystem Design*. (Springer: 2004).

65. Knotter, D. M. Etching Mechanism of Vitreous Silicon Dioxide in HF-Based Solutions. *Journal of the American Chemical Society* **122**, 4345–4351 (2000).

66. Egerton, R. F. *Physical Principles of Electron Microscopy: An Introduction to TEM, SEM, and AEM*. (Springer: 2005).

67. Chen, H., Wang, H., Zhang, X.-H., Lee, C.-S. & Lee, S.-T. Wafer-Scale Synthesis of Single-Crystal Zigzag Silicon Nanowire Arrays with Controlled Turning Angles. *Nano Lett.* **10**, 864–868 (2010).

68. Rykaczewski, K., Hildreth, O. J., Wong, C. P., Fedorov, A. G. & Scott, J. H. J. Directed 2D-to-3D Pattern Transfer Method for Controlled Fabrication of Topologically Complex 3D Features in Silicon. *Advanced Materials* **23**, 659–663 (2011).

69. Rykaczewski, K., Hildreth, O. J., Kulkarni, D., Henry, M. R., Kim, S.-K., Wong, C. P., Tsukruk, V. V. & Fedorov, A. G. Maskless and Resist-Free Rapid Prototyping of Three-Dimensional Structures Through Electron Beam Induced Deposition (EBID) of Carbon in Combination with Metal-Assisted Chemical Etching (MaCE) of Silicon. *ACS Appl. Mater. Interfaces* **2**, 969–973 (2010).

70. Kim, H. J., Bang, I. C. & Onoe, J. Characteristic stability of bare Au-water nanofluids fabricated by pulsed laser ablation in liquids. *Optics and Lasers in Engineering* **47**, 532–538 (2009).

71. Hydrofluoric Acid Properties. (2012).at <http://www51.honeywell.com/sm/hfacid/common/documents/HF_properties_and_graphs.pdf>

72. Lee, D. H., Kim, Y., Doerk, G. S., Laboriante, I. & Maboudian, R. Strategies for controlling Si nanowire formation during Au-assisted electroless etching. *Journal of Materials Chemistry* **21**, 10359–10363 (2011).

73. MathWorks - MATLAB and Simulink for Technical Computing. (2012).at <http://www.mathworks.com/>

74. Wolkin, M. V., Jorne, J., Fauchet, P. M., Allan, G. & Delerue, C. Electronic States and Luminescence in Porous Silicon Quantum Dots: The Role of Oxygen. *Phys. Rev. Lett.* **82**, 197–200 (1999).

75. Bae, J., Kulkarni, N. N., Zhou, J. P., Ekerdt, J. G. & Shih, C.-K. VLS growth of Si nanocones using Ga and Al catalysts. *J. Cryst. Growth* **310,** 4407–4411 (2008).

76. Hsu, C.-M., Connor, S. T., Tang, M. X. & Cui, Y. Wafer-scale silicon nanopillars and nanocones by Langmuir–Blodgett assembly and etching. *Appl. Phys. Lett.* **93,** 133109 (2008).

77. Pokroy, B., Kang, S. H., Mahadevan, L. & Aizenberg, J. Self-Organization of a Mesoscale Bristle into Ordered, Hierarchical Helical Assemblies. *Science* **323**, 237–240 (2009).

78. Duan, H. & Berggren, K. K. Directed Self-Assembly at the 10 nm Scale by Using Capillary Force-Induced Nanocohesion. (2010).

79. Weast, R. C. (editor-in-chief). *Handbook of Chemistry and Physics, 65th Edition*. (CRC Press, 1984).

80. Yae, S., Kawamoto, Y., Tanaka, H., Fukumuro, N. & Matsuda, H. Formation of porous silicon by metal particle enhanced chemical etching in HF solution and its application for efficient solar cells. *Electrochemistry Communications* **5,** 632–636 (2003).

81. Ragone, D. V. *Thermodynamics of Materials Volume I*. (Wiley, 1995).

82. Chang, S., Oh, J., Boles, S. T. & Thompson, C. V. Fabrication of silicon nanopillar-based nanocapacitor arrays. *Appl. Phys. Lett.* **96**, 153108 (2010).